Service Life Assessment of Internal Replacement Pipe: External Load Testing of AQUA-PIPE™

Final Report

Prepared for:

DOE/ARPA-E REPAIR
COREAQUA

Prepared by:

REPAIR Testing & Analysis Team

B. P. Wham, S.G. Senji, P. Dixon, M. Sickler, C. Ihnotic, D. Holt
Center for Infrastructure, Energy, and Space Testing
University of Colorado Boulder

T. D. O'Rourke, J. Strait
Geotechnical Lifelines Large-Scale Testing Facility
Cornell University

November 2024

Table of Contents

List of Figures

List of Tables

Executive Summary

This document reports on a testing program performed on 12-in.- (300-mm) diameter specimens repaired with AQUA-PIPE™ internal replacement pipe (IRP). Five specimens were tested, including those with steel (4) and CI (1) host pipes. The specimens were prepared with a nominal 0.5-in. (12.7 mm) or 6-in. (150 mm) gap of exposed AQUA-PIPE™ lining, with approximately 5 ft (1.52 m) of host pipe on either side of the gap. They were subjected to cyclic flexural and axial loading using specialized testing equipment at the Center for Infrastructure, Energy, and Space Testing (CIEST) at the University of Colorado Boulder and the Bovay Laboratory Complex at Cornell University.

The general methodology consisted of applying bending deformation to a pipe specimen, followed by axial loading. Bending involved 500,000 short duration (1 to 2 Hz) cycles representing cyclic deformation caused by surface traffic. This fatigue testing was followed by larger bending deformations reflective of the system responses to adjacent excavation activity, which in turn were followed by roughly 100,000 additional "traffic" cycles. Then, 50 or more axial cycles were applied, representing the thermal deformation over 50 years associated with annual temperature changes, ΔT, of 40°F or 50°F (22.2°C or 27.8°C). Final axial tension tests were performed to assess the ultimate pullout capacity of the host pipe with AQUA-PIPE™ IRP. As prescribed by the test program, the ultimate capacity in axial tension of all specimens was achieved by IRP detachment from the host pipe. This occurred at loads around 50 kips (220 kN) with gap opening displacements at failure from roughly 5 in. to 12 in. (127 mm to 304.8 mm). Most testing was performed at about 65 psi (450 kPa) of internal water pressure.

The AQUA-PIPE™ repair system performed well under all applied external loads representative of 50 years of service. No cracks or significant structural damage to the IRP were observed during service life testing, and no leakage occurred until the final stages of cyclic testing for thermally induced axial displacements. The product was able to debond locally from the host pipe to accommodate strain concentrations while achieving containment and continuity. While this testing program and the applied cycles were limited to a 50-year service life due to project time constraints, the performance observed suggests that longer durations of testing could demonstrate the ability of the system to accommodate additional years of mechanical aging. This research demonstrates that the proposed service life testing procedures can be accommodated by an existing trenchless technology and supports further applications of the proposed methods.

Acknowledgements

The authors thank DOE/ARPA-E for financially supporting this research and for guiding our progress throughout its execution, In particular, we thank Dr. Jack Lewnard, Dr. Sade Ruffin, and Matthew Hackworth for their leadership of the Rapid Encapsulation of Pipelines Avoiding Intensive Replacement (REPAIR) program. The team extends its gratitude to the Technical & Testing Specifications Pannel (TTSP), who provided valuable practical feedback and industry guidance throughout the project. We thank the staff and students at the University of Colorado at Boulder, University of Southern Queensland, and Cornell University for their many contributions to the REPAIR project as well as the work presented herein. We appreciate greatly COREAQUA (formerly Sanexen Environmental Services' Infrastructure Group) for the donation of test specimens and support through technical discussion with Dr. Martin Buearu, Gilles Gagnon, Jean-Luc Moquin, and Michael Davison.

The information, data, or work presented herein was funded in part by the Advanced Research Projects Agency-Energy (ARPA-E), US Department of Energy under Award No. DE-AR0001327. The views and opinions of authors expressed herein do not necessarily state or reflect those of the United States Government or any agency thereof.

1 Introduction & Background

Compared to the open trench method, trenchless technologies (TT) for water, wastewater, oil, and gas pipelines are used increasingly to replace incident-prone legacy pipes. TT results in less environmental impact and the minimization of excavation activities (Allouche et al., 2014; Lu et al., 2020; Najafi, 2005; Vladeanu & Matthews, 2018). A TT approach has a cost advantage compared to open cut. For a pipe diameter less than or equal to 12 in. (300 mm,) it costs half as much to place an internal lining inside a host pipe than to replace the pipeline inside an open cut (Zhao & Rajani, 2002). There has been much effort to develop internal replacement pipe (IRP) technologies as well as the formal standards and related documents concerning these technologies (Pipeline Infrastructure Committee 2021; ASME PCC-2 Article 403 2018; ASTM F1216 2016a; ASTM F3182 2016b; ASTM F1743 2017; ASTM D5813 2018; ASTM F2207 2019a; AWWA Committee 2019). Nevertheless, there are some outstanding questions about IRP technologies, including long-term suitability and performance, practical considerations for external loads, and the role of adhesion in structural capacity and response. Legacy host pipes undergo various failure modes depending on the type of loading. Moreover, studies are lacking for the long-term response of deteriorated host pipes to internal and external loads (Dixon et al., 2023b; Fu et al., 2020).

This report addresses external loads affecting IRP technologies. It presents lab-based methods for evaluating IRP over a 50-year service life with repaired pipe specimens. The specimens studied featured the IRP material AQUA-PIPE™ (formerly called Altra10x), provided by COREAQUA (formerly Sanexen Environmental Services' Infrastructure Group), which is considered a "known" material that has a successful track record in both laboratory testing and field applications. The external loads are traffic loading, ground movement due to adjacent excavations, and thermally-induced axial deformation of the repaired system. This report is a logical extension of earlier work performed at Cornell University (e.g., Jeon et al., 2004; Stewart et al., 2015), which developed an evaluation framework for cured-in-place liners (CIPLs) under external loads. The framework developed at Cornell University assumed negligible mechanical contribution (stiffness) of the liner to the pipeline response. This assumption was conservative and appropriate, considering the type of materials that were evaluated by Cornell researchers at the time. The current team has altered this aspect in their framework, now accounting for the stiffness of a repair pipe in the estimation of field deformation. The numerical and analytical methods to estimate the field deformation of an AQUA-PIPE ™ IRP are outlined briefly in this report. Detailed test methods and major results are presented. Important observations and various aspects of the testing are discussed.

2 Methodology of Mechanical Aging Tests

The following section describes the test methodology to simulate major aspects of the external loading of an internal REPAIR pipe over a 50-year service life in the field. The approach applies laboratory loading to mimic deformations applied by traffic loading, adjacent excavations, and seasonal temperature fluctuation.

2.1 Lateral Loading

2.1.1 Model Description

A "beam-on-springs" finite element (FE) model was developed in OpenSees for a buried cast iron pipeline subjected to traffic loading and soil displacements representative of adjacent excavation activity. The pipeline elements were represented by 3-in. (75-mm) long, 1D Euler-Bernoulli beam elements. A circumferential gap (also referred to as crack) was modeled by removing host pipe elements. For the cases in which an IRP repair was combined with the host pipe, the missing element or gap was replaced with a beam element with properties of the IRP material and length equal to the width of the gap opening. CI joints were modeled using rotational, shear, and axial springs. Soil was represented using soil springs with a hyperbolic force-displacement.

2.1.2 Traffic Loading

As described in detail by Klingaman et al., (2022), traffic loading was derived from an HS-20 design truck and was conservatively increased to 30 kips (130 kN). The resulting traffic load was assumed to be applied at the ground surface according to the Boussinesq stress distribution for a point load on a semi-infinite elastic medium. The stress calculated at a depth of 30 in. (762 mm) was multiplied by the vertically projected area of the pipe (diameter times element size) and discretely applied to each pipeline node in the FE model (Figure 1). Resulting pipe deformations (e.g., relative rotations) were recorded so that they could be applied in the lab.

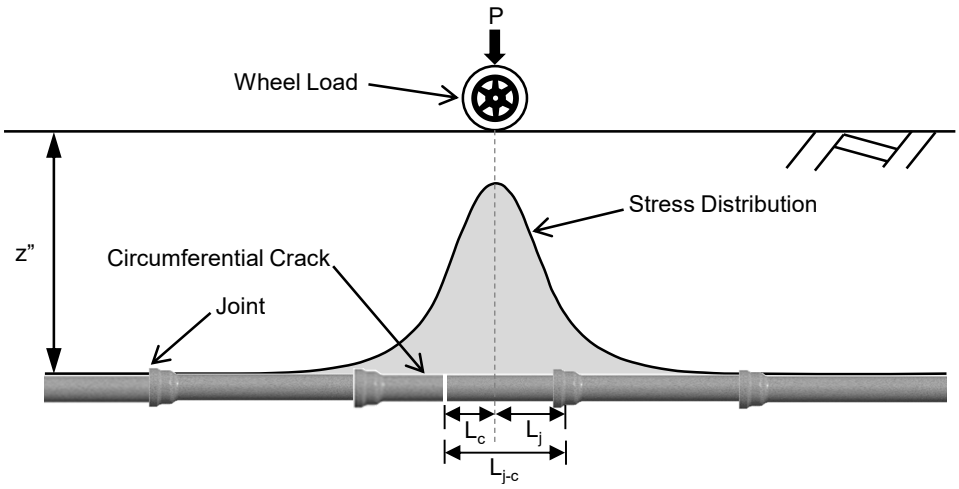

Figure 1. Schematic of traffic loading scenario

2.1.3 Adjacent Excavation

As described by Klingaman et al. (2024), soil displacement profiles were developed using a functional form proposed by Roboski & Finno (2006), which requires 3 inputs: excavation depth, H_e, maximum soil displacement, d_{max}, and the length over which d_{max} is developed, L. The adjacent excavation (AE) depth was assumed to be 20 ft. (6 m), various values of d_{max} were considered, ranging from 2.5-10 in. (63.5-254 mm), and L was assumed to be 50 ft. (15.2 m) (Figure 2). The soil displacements were applied to each soil node in the FE model and resulting rotations were recorded so that they could be applied in the lab. During this study, the smaller and larger parallel (adjacent) excavation events, typically referred to as PE1 and PE2 for each specimen, were associated with d_{max} of 2.5 in. (63.5 mm) and 5 in. (127 mm), respectively.

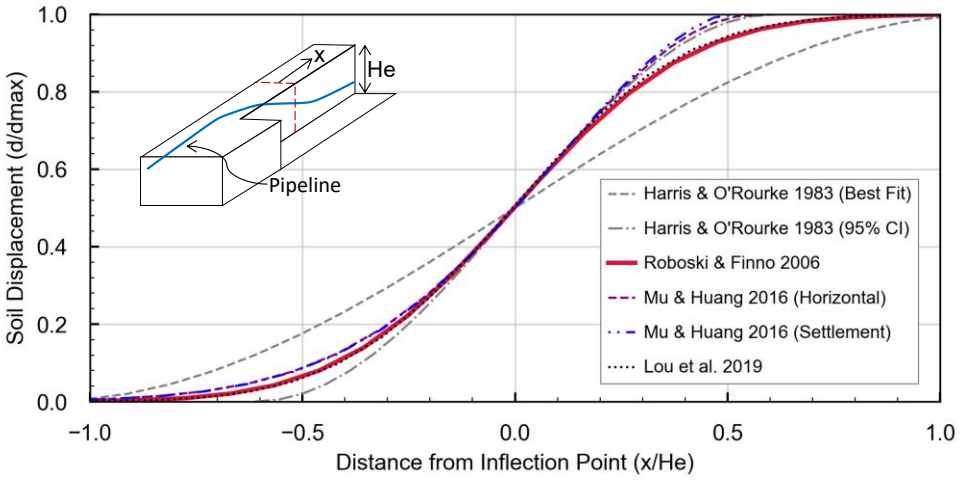

Figure 2. Soil displacement profiles parallel (adjacent) to an excavation from previous studies

2.2 Thermal Loading

Temperature fluctuations in soil will give rise to axial deformation and/or induced axial load in repaired systems from thermal expansion. Previous work used 40°F (22.2°C) as the annual soil temperature variation in New York State (Stewart et al., 2015). This work includes temperature variations of 40°F (22.2°C) and 50°F (27.8°C) and considers granular soil as the backfill material in contact with the host pipe. Additionally, this work considers the stress-free state of the system to be the highest temperature (T_{max}), such that all temperature variation is negative. To understand the problem, a mechanics-based analytical approach has been developed as shown in Figure 3 (Dixon et al., 2023a).

Figure 3. Fully bonded approach schematic with friction from pipe-soil interaction

The specimen is divided into three regions/segments: Segment A refers to the combined host and REPAIR section, and Segment B refers to the exposed REPAIR pipe region (Segment C would refer to the other combined host and REPAIR section but symmetry allows the use of only Segment A and B). The host and repair pipe are treated as fully bonded in Segment A. Simple analytical expressions for the fully unbonded case are straightforward, and it is noted as the gap width (length of Segment B) approaches the system length, induced loads calculated with a fully-bonded assumption approach those for the unbonded case. Furthermore, even in "unbonded" systems, some level of intimate mechanical contact is necessary for a successful installation. So the initial assumption will be fully bonded (if results from initial assessments with small levels of axial displacement demonstrate a fully unbonded system, then the unbonded approach will be used). In this approach Segment A acts as a single unit, i.e., combined section properties and thermo-mechanical response with no differential displacement between the repair and host within the segment. Soil friction, f_u, is accounted for in the approach. Compatibility between the segments is used to solve the induced load, which then can be used to determine the elongation of Segment B, i.e., the crack/gap opening displacement (COD). The aforementioned assumptions are intended to produce the largest expected deformation at the gap opening and, therefore, establish a conservative estimate of thermally induced displacement.

The simple analysis assumes linear elastic materials and properties that do not vary with temperature. Additionally, details of load transfer across the interface and the soil-structure interaction are simplified. However, this approach is leveraged with previous work, finite element models, and knowledge about

AQUA-PIPE™ to obtain target displacements for axial loading (e.g., Ahmadi et al., 2024) that are conservative in magnitude (i.e., displacements greater than those that more detailed methods produce). As discussed later in this report, because this method produces conservative levels of displacement, larger than what would be expected in the field, a safety factor on target displacements should be no greater than 1.5, and FS=1.0 is appropriate for future test programs.

3 Test Specimens and Preparation

Specimens consisted of a host pipe of either steel or cast iron of 12 in. (305 mm) nominal diameter, repaired with COREAQUA's (formerly Sanexen Environmental Services) (Logistec) AQUA-PIPE™ (formerly referred to as Altra10x[1]). Each specimen consisted of two segments of the host pipe, arranged such that, when repaired, full circumferential (ring) gaps of exposed AQUA-PIPE™ are present at the center of the specimen. This condition is intended to represent a worst-case scenario that the fully structural IRP would need to accommodate during its service life (i.e., a circumferential crack or gap in the host pipe). The nominal gap widths were either 0.5 in. (12.7 mm) or 6 in. (152.4 mm). The former dimension reflects a partially displaced (pulled-out) joint in a legacy cast-iron distribution system, which is still functional (determined from utility input), and the latter dimension corresponds to a region of extreme deterioration of the host pipe post-repair. The Testing & Analysis (T&A) Team notes these circumferential gaps are fairly severe, requiring the load to be carried entirely by the repair pipe over a section while simultaneously capturing interactions between host and repair pipe that potentially could give rise to stress concentrations and failures, which would not be observed in the host pipe alone.

AQUA-PIPE™ is cured-in-place pipe system. The structural components are woven polyester (PET) and glass fibers in an epoxy matrix (Figure 4). AQUA-PIPE™ also consists of an inner jacket, which is in contact with the fluid inside the pipe, as well as an outer jacket. A similar product, AQUA-PIPE™, has been investigated by others (e.g., Fu et al., 2020; O'Rourke et al., 2021). O'Rourke et al. (2021) also tested AQUA-PIPE™ and performed experiments with host pipe reinforced by this IRP.

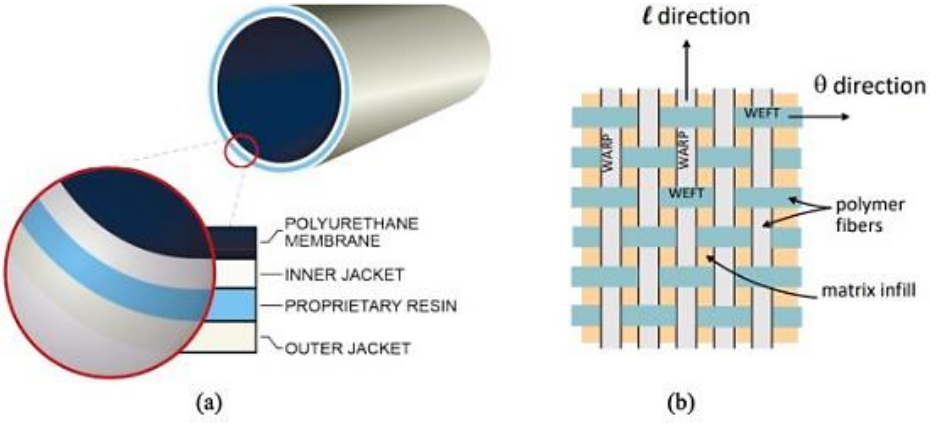

Figure 4. Illustration of AQUA-PIPE™ liner and its components[2]

[1] At the start of this study the IRP material was called Altra10x. A rebranding occurred toward the end of the project (late 2024) that reverted the IRP name back to AQUA-PIPE, which the product has been previously been called cr. 2019. The authors are not aware of any physical differences between Altra10x and the current AQUA-PIPE™.
[2] Figure provided by manufacturer

Tensile coupons and full-scale test specimens were prepared by COREAQUA (formerly Sanexen Environmental Services) at their facilities (Figure 5). Host pipes were shipped in specially designed crates to the manufacturer, and the specimens were prepared following typical installation procedures and then shipped back to the respective testing laboratories.

Figure 5. Preparation of AQUA-PIPE™ specimens, including full-scale specimens (rear) and plates for material testing (center, covered by plywood)

The internal surfaces of the steel host pipe segments were unprotected. No treatment was applied to them prior to lining. A rotary chain tool was applied to the cast-iron host pipe segments' internal surfaces to remove tuberculation, and then some light pressure-washing with water was performed on these surfaces prior to lining. As mentioned, AQUA-PIPE™ is a CIPP system that is widely used in water contexts, and its installation in test specimens is consistent with standard field applications.

The stress-strain behavior of AQUA-PIPE™ in both the weft (circumferential/hoop) and warp (longitudinal) directions are shown in Figure 6. The data in Figure 6(a) was reported by the *Centre de Developement des Composites du Quebec* [CDQC] (Bussières, 2021) and Figure 6(b) shows the representative average response based on the coupon specimens. The initial elastic modulus in the axial direction, 554 ksi (3820 MPa), is used in the following sections.

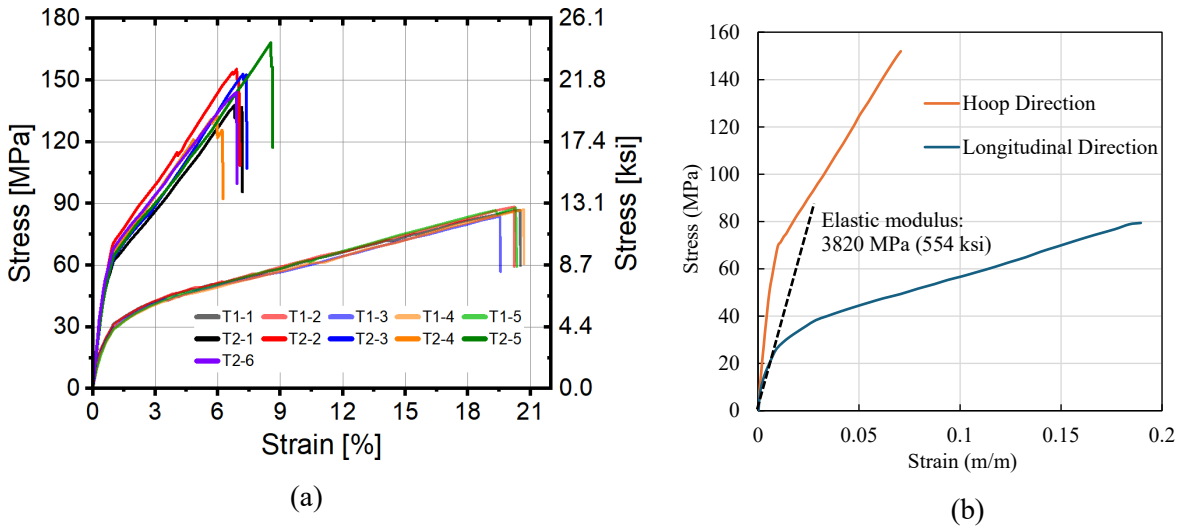

Figure 6. Stress-strain behavior of AQUA-PIPE™ in the longitudinal and hoop directions: (a) tensile coupon test data and (b) representative curve fit to test data

4 Test Methods & Experimental Description

This section describes the procedures performed on the test specimens. The section is divided into bending and axial sections, and these sections are further broken down by the specific specimen. All CU Boulder specimens were tested using the Structural Testing System (STS) at CIEST. General methods were similar among the specimens, but differences in exact instrumentation and methods warrant such a breakdown. Five specimens were investigated. Their general constructions are as described above. The five specimens were as follows: S01) steel host pipe with a nominal 0.5 in (12.7 mm) gap width; C01) cast-iron host pipe with a nominal 0.5 in (12.7 mm) gap width; S02) steel host pipe with a nominal 6 in. (152.4 mm) gap width; S03) steel host pipe with a nominal 0.5 in (12.7 mm) gap width; and S04) steel host pipe with a nominal 0.5 in (12.7mm) gap width. Specimen details are given in Table 1.

Table 1. Basic AQUA-PIPE™ specimen details

Specimen Label	Host Pipe Material	Nominal gap Width (in.) [mm]	Host Pipe OD (in.) [mm]	Approx. Specimen Length (in.) [m]
S01	Steel	0.5 [12.7]	12.75 [324]	127 [3.2]
C01	Cast-iron (legacy)	0.5 [12.7]	13.2 [335]	117 [3.0]
S02	Steel	6 [152.4]	12.75 [324]	133 [3.4]
S03	Steel	0.5 [12.7]	12.75 [324]	127 [3.2]
S04 (Cornell)	Steel	0.5 [12.7]	12.75 [324]	127 [3.2]

Each steel specimen consisted of two 60 in. (1524 mm) long steel host pipe segments, one of which was intact and the other which featured several holes with diameters ranging from 0.25 in. (6.35 mm) to 1.5 in. (38.1 mm). Figure 7 shows drawings of these specimen dimensions.

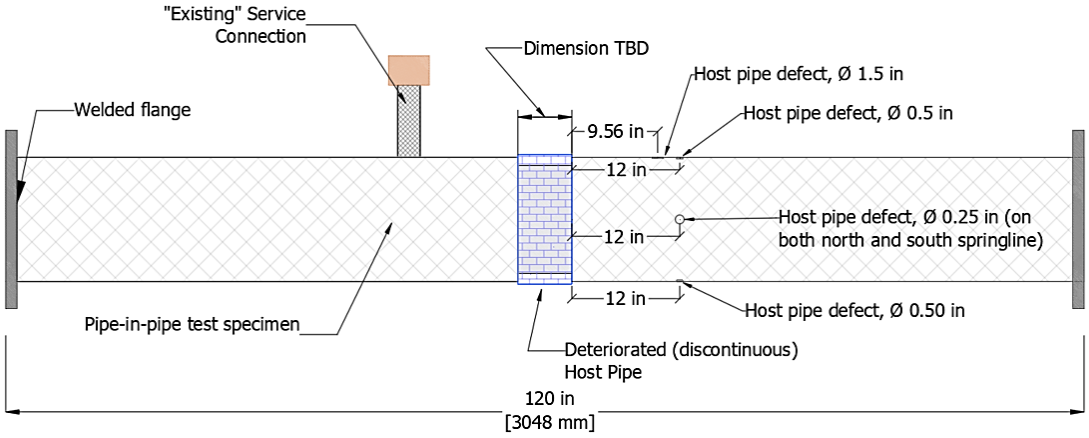

Figure 7. Drawings of specimens including locations of defects and service connection

4.1 Lateral Loading

All CU Boulder specimens were tested in four-point bending, in order to apply a constant moment across the component under investigation (CUI), with a 110-kip (500 kN) or 22-kip (100 kN) [S03] actuator. The Cornell specimen (S04) was tested with a 55-kip (250 kN) actuator. Testing made use of saddles at load and support points to avoid localized loading effects. Strain gauges (SGs), string pots (SPs), and linear variable differential transducers (LVDTs) were applied to all specimens to record displacement. The LVDTs positioned at the outer load points (denoted as EE and WW) were utilized, with measurements taken relative to their respective closest support points, to calculate global rotations. A schematic showing this deformation measure is given below in Figure 8.

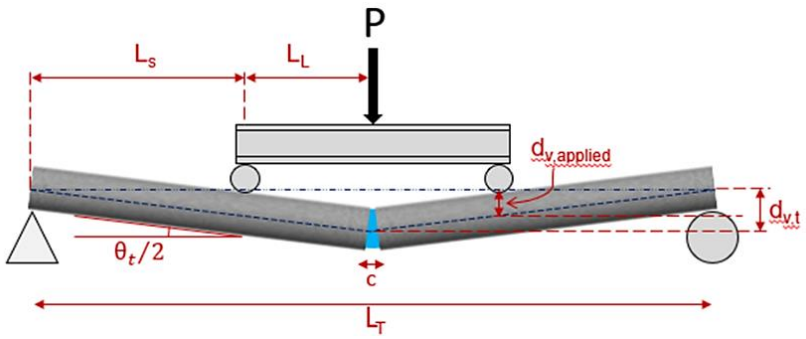

Figure 8. Schematic of rotation angle, θ_t calculated by the arctan($d_{v,applied}/L_s$) multiplied by two (adapted from Klingaman et al. 2022).

Note that, unlike the idealized scenario, the displacements are measured at the two location points, and the two distances are used to calculate the two "half" angles, which are then added to the rotation angle in testing.

All setups featured saddles fitted to the pipe and cages about saddle rollers at both the loading and support points of the specimens. The saddle and cage system allowed the pipeline to return to its initial position without being lifted off its support points, thus simulating deflection in the field wherein the pipeline in soil returns to its original position after rolling traffic loads move across the pipe. To duplicate this condition, some tensile force is mobilized through the saddles to counterbalance the dead weight of the pipeline. For some operations, these cages were loosened, but for most testing, the cages were secured (exceptions clearly noted). Between tests, specimens were supported by jacks to avoid specimen sag under self-weight. The crossbeam used to distribute load was also lifted away from the specimen and supported by restraining chains between each test.

Traffic loading cycles were performed in block sets to allow for setup, sensor retightening, and ease of general lab use. To begin a new traffic cycle set, the specimens with water inside but without pressure were brought to a zero-load position on the jacks. This actuator position essentially served as a reference point for the traffic cycle set. This method was conservative in terms of total deformation applied to the specimen, as this zero-load position commonly reflected a progressively bent shape of the specimens. Most testing was performed at a nominal pressure of 65 psi (450 kPa) with water.

A schematic of test arrangement featuring the measurement devices is shown in Figure 9. The spacing of the sensors and clamps in Figure 9 are listed in detail in Table 3, for S01, and similar tables in the following sections.

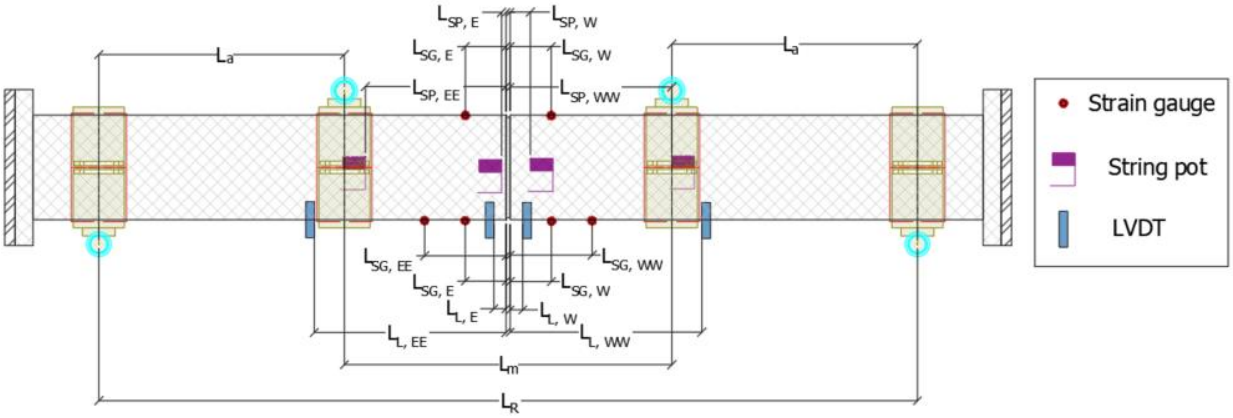

Figure 9. Dimensioned test instrumentation schematic

4.1.1 S01 (CUB)

The gap (also referred to as a crack) width of S01 was initially measured at 0.6 in. (15.24 mm). For analysis purposes, the nominal value was used. The instrumentation of S01 for bending is given by Table 2. It is noted that LVDTs on the outside of the load points (EE & WW) were added after a small initial bending test. Table 2 reflects the test measurements. As shown in Figure 9 the bending test setup was 30 in. – 40 in. – 30 in. (762 mm – 1016 mm - 762 mm) (leaving about a 12 in. (304.8 mm) of overhang, inclusive of flanges on both support points) initially. It is noted that the gap opening was centered for testing. Photographs of the specimen and test setup are shown in Figure 10. The spacing of the sensors and clamps in Figure 9 are listed in detail in Table 3.

Table 2. S01 bending instrumentation table

Instrument Description	Local Instrument Name	Location	Channel No.
East, Crown, 5 in. from gap edge, Circumferential	SG5E_CC	On steel host pipe, crown, east side 5 in. from gap edge	Ch 10
East, Crown, 5 in. from gap edge, Axial	SG5E_CA	On steel host pipe, crown, east side 5 in. from gap edge	Ch 11
East, Invert 5 in. from gap edge, Circumferential	SG5E_IC	On steel host pipe, invert, east side 5 in. from gap edge	Ch. 12
East, Invert, 5 in. from gap edge, Axial	SG5E_IA	On steel host pipe, invert, east side 5 in. from gap edge	Ch. 13
East, Invert 10 in. from gap edge, Circumferential	SG10E_IC	On steel host pipe, invert, east side 10 in. from gap edge	Ch. 8
East, Invert, 10 in. from gap edge, Axial	SG10E_IA	On steel host pipe, invert, east side 10 in. from gap edge	Ch. 9
West, Invert 10 in. from gap edge, Circumferential	SG10W_IC	On steel host pipe, invert, east side 10 in. from gap edge	Ch. 14
West, Invert, 10 in. from gap edge, Axial	SG10W_IA	On steel host pipe, invert, east side 10 in. from gap edge	Ch. 15
West, Crown, 5 in. from gap edge, Circumferential	SG5W_CC	On steel host pipe, crown, west side 5 in. from gap edge	Ch. 16
West, Crown, 5 in. from gap edge, Axial	SG5W_CA	On steel host pipe, crown, west side 5 in. from gap edge	Ch. 17
West, Invert, 5 in. from gap edge, Circumferential	SG5W_IC	On steel host pipe, invert, west side 5 in. from gap edge	Ch. 18
West, Invert 5 in. from gap edge, Axial	SG5W_IA	On steel host pipe, invert, west side 5 in. from gap edge	Ch. 19
Vertical String pot, West, South Springline on Saddle (19.75 in. from gap edge)	SP18-10_WW	On west saddle (centered), south springline, 19.75 in. from gap edge	Ch 1.
Vertical String pot, West, South Springline on Steel Pipe (2.5 in. from gap edge)	SP17-20_W	On steel host pipe, west side, south springline, 2.5 in. from gap edge	Ch. 2
Vertical String pot, East South Springline on Steel Pipe (0.5 in. from gap edge)	SP15-10_E	On steel host pipe, east side, south springline, 0.5 in. from gap edge	Ch. 3
Vertical String pot, East, South Springline on Saddle (19.75 in. from gap edge)	SP19-20_EE	On east saddle (centered), south springline, 19.75 in. from gap edge	Ch. 5
LVDT 1020, West, Invert, 1.5 in from gap edge	LVDT06_1020W	On bracket on steel, west, invert, 1.5 in. from gap edge	LVDT Ch. 6
LVDT 1021, East Invert, 1.5 in from gap edge	LVDT07_1021E	On bracket on steel, east, invert, 1.5 in. from gap edge	LVDT Ch. 7
LVDT 1017, West, Invert, 23 in from gap edge	LVDT2_1017WW	On bracket on steel, west, invert, outside east load saddle, 23 in from gap edge	LVDT Ch. 2

LVDT 1008, East, Invert, 23 in from gap edge	LVDT10_1008EE	On bracket on steel, east, invert, outside east load saddle, 23 in from gap edge	LVDT Ch. 10
110-kip Load Cell	Applied Force	MTS Crosshead (Above Specimen)	
MTS Actuator Piston Position		MTS Crosshead (Above Specimen)	
150 psi Pressure Transducer	N/A	N/A	Ch. 21

* VSP: vertical string pot, LVDT: linearly varying differential transducer, SG: foil stain gage

Table 3. Test instrumentation schematic dimensions

Sensor / Measurement	Symbol	Distance
Strain Gauge (EE)	$L_{SG, EE}$	10 in
Strain Gauge (E)	$L_{SG, E}$	5 in
Strain Gauge (W)	$L_{SG, W}$	5 in
Strain Gauge (WW)	$L_{SG, WW}$	10 in
String Pot (EE)	$L_{SP, EE}$	19.75 in
String Pot (E)	$L_{SP, E}$	0.5 in
String Pot (W)	$L_{SP, W}$	2.5 in
String Pot (WW)	$L_{SP, WW}$	19.75 in
LVDT (EE)	$L_{L, EE}$	23 in
LVDT (E)	$L_{L, E}$	1.5 in
LVDT (W)	$L_{L, W}$	1.5 in
LVDT (WW)	$L_{L, WW}$	23 in
Distance between reaction and applied force	L_a	30 in
Distance between reactions	L_R	100 in
Distance between applied forces	L_m	40 in

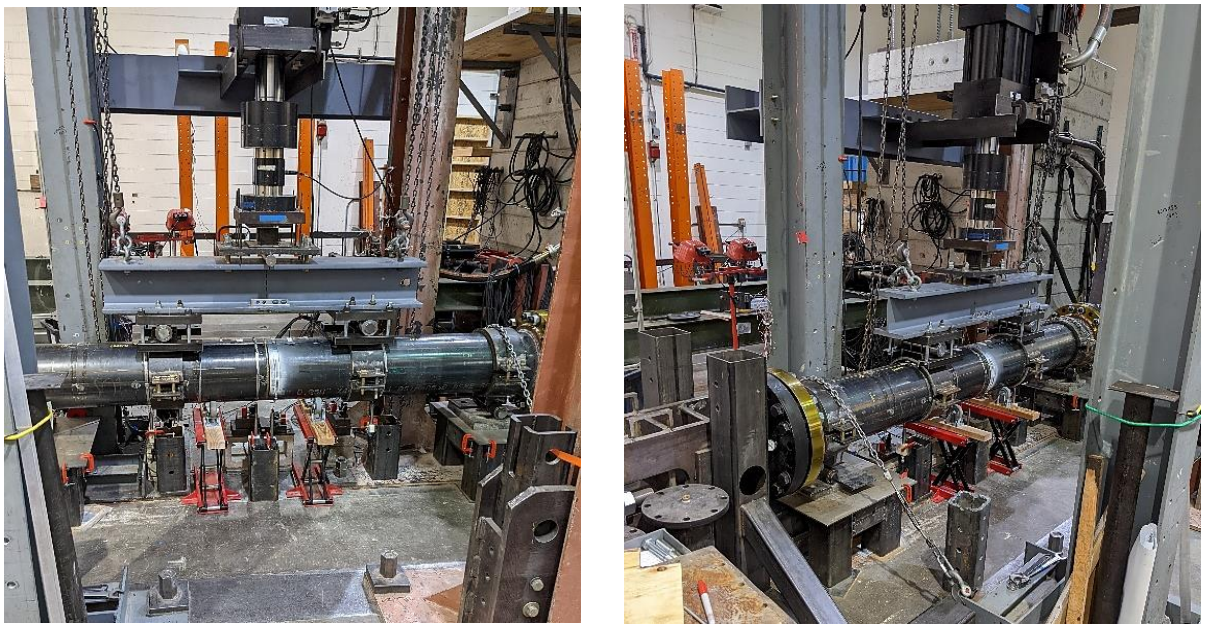

Figure 10. Images of S01 bending setup

Several preliminary bend tests were performed on S01 to check that instrumentation was functioning and assess the stiffness. Traffic loading cycles were then performed. These were predominantly performed at cyclic frequencies of 1 Hz and 2 Hz, associated with sample rates of 16 Hz and 64 Hz, respectively. For S01, the targeted rotation was 0.09°, which was determined from the analysis as described in Section 2.1.2, and increased with a safety factor of 1.5. Applied global rotations ranged from 0.09° to 0.12°; the actuator displacement associated with achieving these rotations was about 0.04 in. (1 mm) and displacement from the LVDTs outside the load points was about 0.022 in. (0.56 mm). After approximately 475,000 traffic cycles, the bending configuration was adjusted to a 25 in. – 40 in. – 25 in. (635 mm – 1016 mm – 635 mm) setup to be consistent with the configuration that would be used on the slightly shorter CI specimen (C01). About 25,000 cycles were performed in this updated configuration.

Most traffic cycles were performed with constant water pressure. However, some cycles near the 350,000-cycle mark were performed without pressure. In this configuration, similar rotations were achieved with similar actuator displacements.

Then deformations were applied to simulate adjacent (i.e., parallel) excavations. These were performed with constant internal water pressure, which led to pressure fluctuations under large deformation. Cages were loosened and restraining chains were loosened for this procedure. This consisted of an initial bend to a rotation of 0.18°, associated with an actuator displacement of 0.08 in. (2 mm). The actuator was then returned to the initial test position, and the specimen was loaded to a rotation of 0.6°, associated with

an actuator displacement of 0.22 in. (5.6 mm). Displacement measured by the LVDTs outside the load points was about 0.12 in. (3 mm). These rotations correspond to values from the adjacent excavation model considering soil displacements of 0.5 in. and 1.5 in. (12.7 mm and 38.1 mm), adjusted with a safety factor of 1.5. Crosshead speed was 0.2 in./min (5 mm/min).

After the adjacent excavation testing, the cages and restraining chains were retightened. Roughly 125,000 subsequent traffic cycles were then performed with similar rotation about the gap and actuator displacement as the previous cycles. Lastly, an additional bend simulating the smaller deformation adjacent excavation (0.08 in. (2 mm) actuator displacement) was performed with cages and chains set as they are for the traffic cycles, with dead pressure at a crosshead speed of 0.2 in./min (5 mm/min). This concluded the bending procedure for S01. It is noted in the testing of S01 that pressurizations and depressurizations were not recorded. When not under test, save a few instances, the specimen was kept in a depressurized state.

4.1.2 C01 (CUB)

The average gap width of C01 was initially measured at 0.6 in. (15.24 mm). For analysis purposes, this nominal value was used. The instrumentation of C01 for bending is given by Table 4. It is very similar to that for S01. The bending test configuration for C01 was 25 in. – 40 in. – 25 in. (635 mm – 1016 mm – 635 mm). It is noted that gap is centered in the test setup. Photographs of specimen and test setup are shown in Figure 11.

Figure 11. Images of C01 bending setup

Table 4. C01 bending instrumentation table

Instrument Description	Local Instrument Name	Location	Channel No.
East, Crown, 5 in. from gap edge, Circumferential	SG5E_CC	On CI host pipe, crown, east side 5 in. from gap edge	Ch 10
East, Crown, 5 in. from gap edge, Axial	SG5E_CA	On CI host pipe, crown, east side 5 in. from gap edge	Ch 11
East, Invert 5 in. from gap edge, Circumferential	SG5E_IC	On CI host pipe, invert, east side 5 in. from gap edge	Ch. 12
East, Invert, 5 in. from gap edge, Axial	SG5E_IA	On CI host pipe, invert, east side 5 in. from gap edge	Ch. 13
East, Invert 10 in. from gap edge, Circumferential	SG10E_IC	On CI host pipe, invert, east side 10 in. from gap edge	Ch. 8
East, Invert, 10 in. from gap edge, Axial	SG10E_IA	On CI host pipe, invert, east side 10 in. from gap edge	Ch. 9
West, Invert 10 in. from gap edge, Circumferential	SG10W_IC	On CI host pipe, invert, east side 10 in. from gap edge	Ch. 14
West, Invert, 10 in. from gap edge, Axial	SG10W_IA	On CI host pipe, invert, east side 10 in. from gap edge	Ch. 15
West, Crown, 5 in. from gap edge, Circumferential	SG5W_CC	On CI host pipe, crown, west side 5 in. from gap edge	Ch. 16
West, Crown, 5 in. from gap edge, Axial	SG5W_CA	On CI host pipe, crown, west side 5 in. from gap edge	Ch. 17
West, Invert, 5 in. from gap edge, Circumferential	SG5W_IC	On CI host pipe, invert, west side 5 in. from gap edge	Ch. 18
West, Invert 5 in. from gap edge, Axial	SG5W_IA	On CI host pipe, invert, west side 5 in. from gap edge	Ch. 19
Vertical String pot, West, South Springline on Saddle (19.75 in. from gap edge)	SP18-10_WW	On west saddle (centered), south springline, 19.75 in. from gap edge	Ch 1.
Vertical String pot, West, South Springline on CI Pipe (2.5 in. from gap edge)	SP17-20_W	On CI host pipe, west side, south springline, 2.19 in. from gap edge	Ch. 2
Vertical String pot, East South Springline on CI Pipe (0.5 in. from gap edge)	SP15-10_E	On CI host pipe, east side, south springline, 2.69 in. from gap edge	Ch. 3
Vertical String pot, East, South Springline on Saddle (19.75 in. from gap edge)	SP19-20_EE	On east saddle (centered), south springline, 19.88 in. from gap edge	Ch. 5
LVDT 1020, West, Invert, 1.5 in from gap edge	LVDT06_1020W	On backet on CI, west, invert, 1.5 in. from gap edge	LVDT Ch. 6
LVDT 1021, East Invert, 1.5 in from gap edge	LVDT07_1021E	On backet on CI, east, invert, 1.25 in. from gap edge	LVDT Ch. 7
LVDT 1017, West, Invert, 23 in from gap edge	LVDT2_1017WW	On bracket on CI, west, invert, outside east load	LVDT Ch. 2

		saddle, 23.94 in from gap edge	
LVDT 1008, East, Invert, 23 in from gap edge	LVDT10_1008EE	On bracket on CI, east, invert, outside east load saddle, 23.81 in from gap edge	LVDT Ch. 10
110-kip Load Cell	Applied Force	MTS Crosshead (Above Specimen)	
MTS Actuator Position		MTS Crosshead (Above Specimen)	
500 psi Pressure Transducer	N/A	N/A	Ch. 21

Preliminary bend tests were performed on C01 to check that instrumentation was functioning and assess the stiffness. Traffic loading cycles were then performed, predominantly at cyclic frequencies of 1 Hz and 2 Hz, with a sample rate of 64 Hz. For C01, the targeted rotation was 0.12°, which was determined from the analysis as described in Section 2.1.2, and increased with a safety factor of 2. Applied global rotations ranged from 0.11° to 0.15°; the actuator displacement associated with achieving these rotations was about 0.035 in. (0.9 mm) generally, and the displacement from the LVDTs outside the load points was about 0.026 in. (0.66 mm). Roughly 485,000 cycles were performed in the vast majority under constant (dead) pressure. Some cycles around the 420,000-cycle mark were performed without pressure.

After the ~485,000 cycles of traffic loading, deformations were applied to simulate parallel excavations. These were performed at a crosshead speed of 0.2 in/min (5 mm/min) with dead pressure, which led to fluctuations in internal pressure under this large deformation. Cages were loosened, and restraining chains were removed for this procedure. This consisted of an initial bend to a rotation of 0.26°, associated with an actuator displacement of 0.08 in. (2 mm). The actuator was then returned to the initial test position, and then the specimen was loaded to a rotation of 0.77°, associated with an actuator displacement of 0.20 in. (5 mm), and displacement from the LVDTs outside the load points was about 0.14 in. (3.6 mm). These rotations roughly correspond to values from the parallel excavation model considering soil displacements of 0.5 in. and 1.5 in. (12.7 mm and 38.1 mm). A safety factor of 1.5 was used to adjust the rotation.

After the parallel excavation testing, the cages and restraining chains were retightened. Roughly 110,000 subsequent traffic cycles were then performed with actuator displacement similar to the previous cycles. Lastly, an additional bend simulating the smaller deformation parallel excavation (0.08 in. (2 mm) actuator displacement) was performed with cages and chains tight and with dead pressure at a crosshead speed of 0.2 in/min (5 mm/min). This concluded the bending procedure for C01. It is noted that in the C01 testing, pressurizations and depressurizations were not recorded. When not under test, the specimen was kept in a depressurized state.

4.1.3 S02 (CUB)

The average gap opening width of S02 was initially measured at 6.11 in. (155.2 mm). For analysis purposes, this nominal value was used. The instrumentation of S02 for bending is given by Table 5. It is very similar to that for S01 and C01 but features some instrumentation on the exposed AQUA-PIPE™ repair pipe. The bending test configuration for S02 was 26.5 in. – 40 in. – 26.5 in. (673 mm – 1016 mm – 673 mm). It is noted that gap is centered. Photographs of the specimen and test setup are shown in Figure 12.

Table 5. S02 bending instrumentation table

Instrument Description	Local Instrument Name	Location	Channel No.
East, Crown, 5 in. from gap edge, Circumferential	SG5E_CC	On steel host pipe, crown, east side 5 in. from gap edge	Ch 10
East, Crown, 5 in. from gap edge, Axial	SG5E_CA	On steel host pipe, crown, east side 5 in. from gap edge	Ch 11
East, Invert 5 in. from gap edge, Circumferential	SG5E_IC	On steel host pipe, invert, east side 5 in. from gap edge	Ch. 12
East, Invert, 5 in. from gap edge, Axial	SG5E_IA	On steel host pipe, invert, east side 5 in. from gap edge	Ch. 13
Center Invert, Center Gap, Circumferential	SGCenC_IC	On liner, invert, ~1 in. west of gap center	Ch. 8
East, Invert, 10 in. from gap edge, Axial	SG10E_IA	On steel host pipe, invert, east side 10 in. from gap edge	Ch. 9
Center Crown Center Gap, Circumferential	SGCenC_CC	On liner, crown ~1 in. west of gap center	Ch. 14
West, Invert, 10 in. from gap edge, Axial	SG10W_IA	On steel host pipe, invert, east side 10 in. from gap edge	Ch. 15
West, Crown, 5 in. from gap edge, Circumferential	SG5W_CC	On steel host pipe, crown, west side 5 in. from gap edge	Ch. 16
West, Crown, 5 in. from gap edge, Axial	SG5W_CA	On steel host pipe, crown, west side 5 in. from gap edge	Ch. 17
West, Invert, 5 in. from gap edge, Circumferential	SG5W_IC	On steel host pipe, invert, west side 5 in. from gap edge	Ch. 18
West, Invert 5 in. from gap edge, Axial	SG5W_IA	On steel host pipe, invert, west side 5 in. from gap edge	Ch. 19
Center Invert, Center Gap, Axial	SGCenC_IA	On liner, invert, ~1 in. west of gap center	Ch. 6
Center North Springline Center Gap, Axial	SGCenC_SlA	On liner, north springline ~1 in. west of gap center	Ch. 7
Center Crown, Center Gap, Axial	SGCenC_CA	On liner, crown ~1 in. west of gap center	Ch. 20
Vertical String pot, West, South Springline on Saddle (19.75 in. from gap edge)	SP18-10_WW	On west saddle (centered), south springline, 19.75 in. from gap edge	Ch 1.

Vertical String pot, West, South Springline on Steel Pipe (2.5 in. from gap edge)	SP17-20_W	On steel host pipe, west side, south springline, 2.5 in. from gap edge	Ch. 2
Vertical String pot, East South Springline on Steel Pipe (0.5 in. from gap edge)	SP15-10_E	On steel host pipe, east side, south springline, 0.5 in. from gap edge	Ch. 3
Vertical String pot, East, South Springline on Saddle (19.75 in. from gap edge)	SP19-20_EE	On east saddle (centered), south springline, 19.75 in. from gap edge	Ch. 5
LVDT 1020, West, Invert, 1.5 in from gap edge	LVDT06_1020W	On backet on steel, west, invert, 1.5 in. from gap edge	LVDT Ch. 6
LVDT 1021, East Invert, 1.5 in from gap edge	LVDT07_1021E	On backet on steel, east, invert, 1.5 in. from gap edge	LVDT Ch. 7
LVDT 1017, West, Invert, 23 in from gap edge	LVDT2_1017WW	On bracket on steel, west, invert, outside east load saddle, 23 in from gap edge	LVDT Ch. 2
LVDT 1008, East, Invert, 23 in from gap edge	LVDT10_1008EE	On bracket on steel, east, invert, outside east load saddle, 23 in from gap edge	LVDT Ch. 10
LVDT 1005, Center, Invert, Gap Center	LVDT4_1005_Center	On magnet on inch worm (hose clamp) around the liner, center of the gap	LVDT Ch. 4
110-kip Load Cell	Applied Force	MTS Crosshead (Above Specimen)	
MTS Actuator Piston Position		MTS Crosshead (Above Specimen)	
500 psi Pressure Transducer	N/A	N/A	Ch. 21

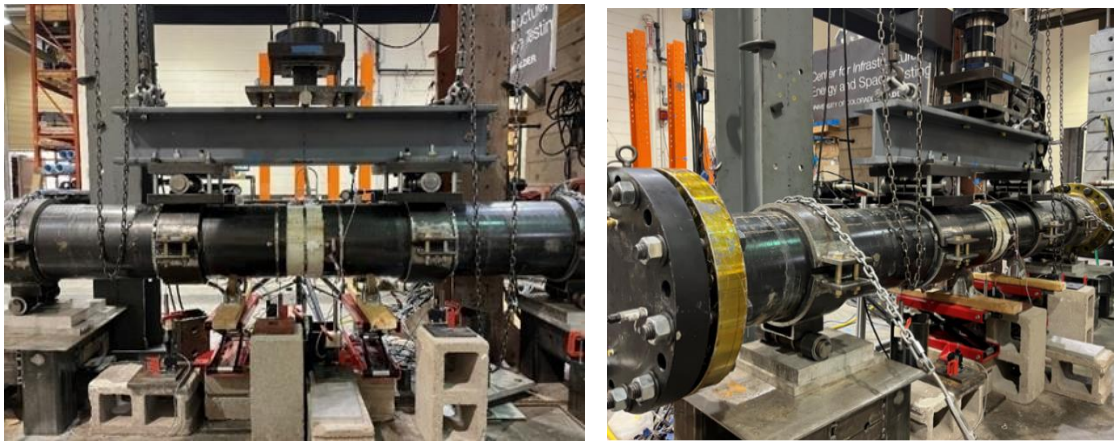

Figure 12. S02 bending setup

Preliminary bend tests were performed on S02 to check that instrumentation was functioning and assess the stiffness. Traffic loading cycles were then performed. These were predominantly performed at cyclic frequencies of 1 Hz and 2 Hz, with a sample rate of 64 Hz. For S02, the targeted rotation was 0.20°, which was determined from the analysis as described in Section 2.1.2 and increased with a safety factor of 2. Applied global rotations ranged from 0.21° to 0.25°; the actuator displacement associated with achieving these rotations was about 0.062 in. (1.6 mm) generally, displacement from the LVDTs outside the load points was about 0.042 in. (1 mm). Roughly 500,000 cycles were performed, the vast majority under (dead) pressure. Some cycles around the 495,000 cycle mark were performed without pressure.

After the ~500,000 cycles of traffic loading, deformations were applied to simulate parallel excavations. These were performed at a crosshead speed of 0.2 in/min (5 mm/min) with live pressure. Cages were loosened and restraining chains were removed for this procedure. This consisted of a first bend to a rotation of 1.5°, associated with an actuator displacement of 0.39 in. (9.9 mm). The second parallel excavation bend was to a rotation of 3.3°, associated with an actuator displacement of 0.84 in. (21.3 mm) and displacement from the LVDTs outside the load points was about 0.68 in. (17.2 mm). Pressure was dropped at maximum deflection and then returned for unloading. These rotations roughly correspond to values from the parallel excavation model considering soil displacements of 2.5 and 5 in. (63.5 mm and 127 mm), adjusted with a safety factor of two.

After the parallel excavation testing, the cages and restraining chains were retightened. Roughly 100,000 subsequent traffic cycles were then performed with similar actuator displacement as the previous cycles. Lastly an additional bend simulating the smaller deformation parallel excavation (0.36 in. (9.1 mm) actuator displacement) was performed with cages and chains set as they are for the traffic cycles with live pressure at a crosshead speed of 0.2 in/min (5 mm/min). This concluded the bending procedure for S02. It is noted in the testing of S02, pressurizations and depressurizations were recorded in testing. When not under test, the specimen was kept in a depressurized state generally.

4.1.4 S03 (CUB)

The average measured gap width of S03 was initially 0.41 in. (10.4 mm). For analysis purposes, this nominal value was used. The instrumentation consisted of strain gauges on the crown and invert over the middle 40 in. (1000 mm) (maximum moment) span in the vicinity of the gap opening. Linear variable differential transducers (LVDTs) and string potentiometers (SPs) were vertically arranged to measure pipe deflection at various locations on the beam. LVDTs were mounted on stands on the ground and the rods were connected to the pipes with brackets or screw sockets. SPs were mounted on the pipe, stands on the grounds, and beams extending from the strong wall (frame support). Additionally, the north-facing side of

the pipe over and in the vicinity of the gap was painted white and speckled black for digital image correlation (see Figure 13).

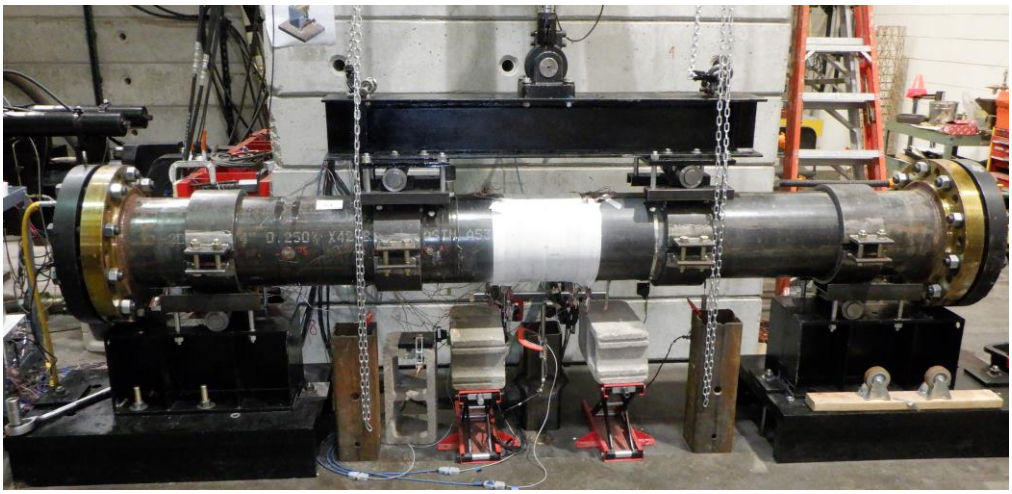

Figure 13. S03 bending setup

The instrumentation details are given in Table 6. The bending test configuration for S03 was 25in. – 40 in. – 25 in. (635 mm – 1016 mm – 635 mm) on a 22-kip load cell, which was a different test instrument than used for C01, S01, and S02 (110-kip load cell).

Table 6. Instrumentation overview for S03

Instrument Description	Local Instrument Name	Location	Channel No.
East, Crown, 5 in. from gap edge, Axial	SG0CAE5_0	On steel host pipe, crown, east side 5 in. from gap edge	Ch. 0
East, Crown, 1 in. from gap edge, Axial	SG1CAE1_1	On steel host pipe, crown, east side 1 in. from gap edge	Ch. 1
East, Invert, 5 in. from gap edge, Axial	SG15AE5_4	On steel host pipe, crown, east side 5 in. from gap edge	Ch. 4 (initial 15)
East, Invert, 3 in. from gap edge, Axial	SG5IAE3_5	On steel host pipe, invert, east side 3 in. from gap edge	Ch. 5
East, Invert, 1 in. from gap edge, Axial	SG6IAE1_6	On steel host pipe, invert, east side 1 in. from gap edge	Ch. 6
West, Crown, 1 in. from gap edge, Axial	SG2CAW1_2	On steel host pipe, invert, east side 1 in. from gap edge	Ch. 2
West, Crown, 5 in. from gap edge, Axial	SG3CAW5_3	On steel host pipe, invert, east side 5 in. from gap edge	Ch. 3
West, Invert, 1 in. from gap edge, Axial	SG7IAW1_7	On steel host pipe, invert, east side 1 in. from gap edge	Ch. 7
West, Invert, 3 in. from gap edge, Axial	SG8IAW3_8	On steel host pipe, invert, east side 3 in. from gap edge	Ch. 8
West, Invert, 5 in. from gap edge, Axial	SG9IAW5_9	On steel host pipe, crown, west side 5. from gap edge	Ch. 9
West, Invert, 5 in. from gap edge, Circumferential	SG13ICW5_13	On steel host pipe, invert, west side 5 in. from gap edge	Ch. 13
West, Crown, 5 in. from gap edge, Circumferential	SG11CCW5_11	On steel host pipe, crown, west side 5 in. from gap edge	Ch .11
East, Invert, 5 in. from gap edge, Circumferential	SG12ICE5_12	On steel host pipe, invert, east side 5 in. from gap edge	Ch. 12
East, Crown, 5 in. from gap edge, Circumferential	SG10CCE5_10	On steel host pipe, crown, east side 5 in. from gap edge	Ch. 10

Vertical String pot, West, South Springline on Saddle (15.75 in. from gap edge)	SPWW23-3	On floor (mounted on steel host pipe at invert), west side, 15.75 in. from gap edge	SP (module) Ch. 3
Vertical String pot, West, South Springline on Steel Pipe (1.875 in. from gap edge)	SP2W18-10	On steel host pipe (mounted on bars from support block), west side, south springline, 1.875 in. from gap edge	SP (module) Ch. 2
Vertical String pot, East South Springline on Steel Pipe (1.975 in. from gap edge)	SP1E15-10	On steel host pipe (mounted on bars from support block), east side, south springline, 1.975 in. from gap edge	SP (module) Ch. 1
Vertical String pot, East, South Springline on Saddle (14.25 in. from gap edge)	SP0EE21-3	On steel host pipe (clamped on blocks on floor), east side, invert, 14.25 in. from gap edge	SP (module) Ch. 0
LVDT 1020, West, Invert, 0.2 in from gap edge	LVDT2_1020W	On backet on steel, west, invert, 0.2 in. from gap edge	LVDT Ch. 2
LVDT 1021, East, South Springline, 4.315 in from gap edge	LVDT1_1021E	On backet on steel, east, south springline, 4.315 in. from gap edge	LVDT Ch. 1
LVDT 1017, West, Invert, 24.375 in from gap edge	LVDT3_1017WW	On screw socket on steel, west, invert, outside west load saddle, 24.375 in from gap edge	LVDT Ch. 3
LVDT 1005, East, Invert, 25.25 in from gap edge	LVDT0_1005EE	On screw socket on steel, east, invert, outside east load saddle, 25.25 in from gap edge	LVDT Ch. 0
22-kip Load Cell	Applied Force	MTS Crosshead (Above Specimen)	
MTS Actuator Piston Position		MTS Crosshead (Above Specimen)	
150 psi Pressure Transducer	N/A	N/A	SP module Ch. 7

Several preliminary bend tests were performed on S03 to check that instrumentation was functioning and assess the stiffness. Traffic loading cycles were then performed. These were predominantly performed at cyclic frequencies of 1 Hz and 2 Hz, and with a sample rate of 64 Hz For S03, the targeted rotation was 0.12°, which was determined from the analysis as described in Section 2.1.2, and increased with a safety factor of 1.5. Applied global rotations ranged from about 0.11° to 0.12°; the actuator displacement associated with achieving these rotations was about 0.08 in. (2 mm) and displacement from the LVDTs

outside the load points was about 0.021 in. (0.5 mm). The majority of these were performed with dead water pressure [nominal value of 65 psi (450 kPa)].

After approximately 500,000 cycles the deformations were applied to simulate parallel excavations. These were performed with live water pressure. Cages were loosened for this testing. The parallel excavation bend procedure consisted of an initial bend to a rotation of 1.09°, associated with outer LVDT displacements around 0.2 in. (5 mm). The actuator was then returned to the initial test position, and the specimen was loaded to a rotation of 1.8°, associated with outer LVDT displacements around 0.45 in. (11.5 mm) [0.35 in. (9 mm). These rotations correspond to values from a parallel excavation model considering maximum soil displacements of 2.5 in. and 5 in. (63.5 mm and 127 mm) and a safety factor of two. The crosshead speed was 0.2 in./min (5 mm/min). The associated maximum actuator displacement applied was 0.71 in. (18 mm).

After the parallel excavation testing, the cages were retightened. Roughly 100,000 subsequent traffic cycles were then performed. The first ca. 15,000 cycles were performed with very similar test set-up parameters (actuator displacement command) as the previous traffic cycles. The stiffness had been reduced by the parallel excavation bends, and the rotation was roughly 0.25°. Based on the reduction in stiffness, the parameters of the following cycles were changed, and a rotation of roughly 0.40° was applied to the specimen for the remaining 85,000 traffic cycles.

4.1.5 S04 (Cornell)

Table 7 lists the location, instrument type, and local instrument name. The instruments and their locations both north and south of the gap at the center of the specimen are depicted in Figure 14. Vertical displacements along the length of the specimen were measured using LVDTs and SPs. The LVDTs were mounted on stands on the base frame with their rods positioned against brackets connected to the pipeline. SPs were mounted next to the LVDTs utilizing the same brackets.

Table 7. SNES04 four-point bending instrumentation table

Location	Instrument Description	Local Instrument Name
25 in. North of Centerline	LVDT	LVDT_N25
	String Potentiometer	VSP_N25
10 in. North of Centerline	Invert, Axial Strain	IA_N10
	Invert, Circumferential Strain	IC_N10
5 in. North of Centerline	Crown, Axial Strain	CA_N5
	Crown, Circumferential Strain	CC_N5
	Invert, Axial Strain	IA_N5
	Invert, Circumferential Strain	IC_N5
1 in. North of Centerline	LVDT	LVDT_N1

	String Potentiometer	VSP_N1
1 in. South of Centerline	LVDT	LVDT_S1
	String Potentiometer	VSP_S1
5 in. South of Centerline	Crown, Axial Strain	CA_S5
	Crown, Circumferential Strain	CC_S5
	Invert, Axial Strain	IA_S5
	Invert, Circumferential Strain	IC_S5
10 in. South of Centerline	Invert, Axial Strain	IA_S10
	Invert, Circumferential Strain	IC_S10
25 in. South of Centerline	LVDT	LVDT_S25
	String Potentiometer	VSP_S25
Actuator	MTS Load Xducer (55 kip)	Actuator_Load
	MTS Actuator LVDT (±3")	Actuator_Disp_In
	String Potentiometer	Actuator_Disp_Ex
Pipe South End	Pressure Xducer Pipe	Pressure_Pipe
	Flow Meter	Flow_Meter
Wall Valve	Pressure Xducer Wall	Pressure_Deck

A characteristic of four-point bending, for which a schematic is shown in Figure 14, is constant moment ($M_{central}$), across the central 40 in. (1016 mm) that separates the two load points. The moment increases from zero to $M_{central}$ across the 25-in. (625-mm) separation between the load and support points. The moment applied to the central portion of the specimen, $M_{central}$, was calculated as

$$M_{central} = \frac{P\,(25in.)}{2} \tag{1}$$

in which P is the load applied by the actuator to the load beam plus the vertical force of the load beam of 0.23 kips (1.02 kN).

A global rotation was measured, which is the relative rotation at the pipeline center between straight-line projections of the pipes on either side of the gap. Global rotation in response to traffic loads is shown and discussed by Stewart et al. (2015). In this section of the report, global rotation is often referred to as rotation. It was calculated as

$$\theta\ (\text{degrees}) = \sin^{-1}\left[\frac{0.80(d_{v1}+d_{v2})}{20in.}\right] \tag{2}$$

for which d_{v1} and d_{v2} are the relative vertical displacements (in.) between the support points and the nearest linear voltage differential transformer (LVDT)/string potentiometer (SP) locations on either side of the gap. The distance 20 in. (508 mm) refers to the separation between the support point and the nearest LVDT/SP location.

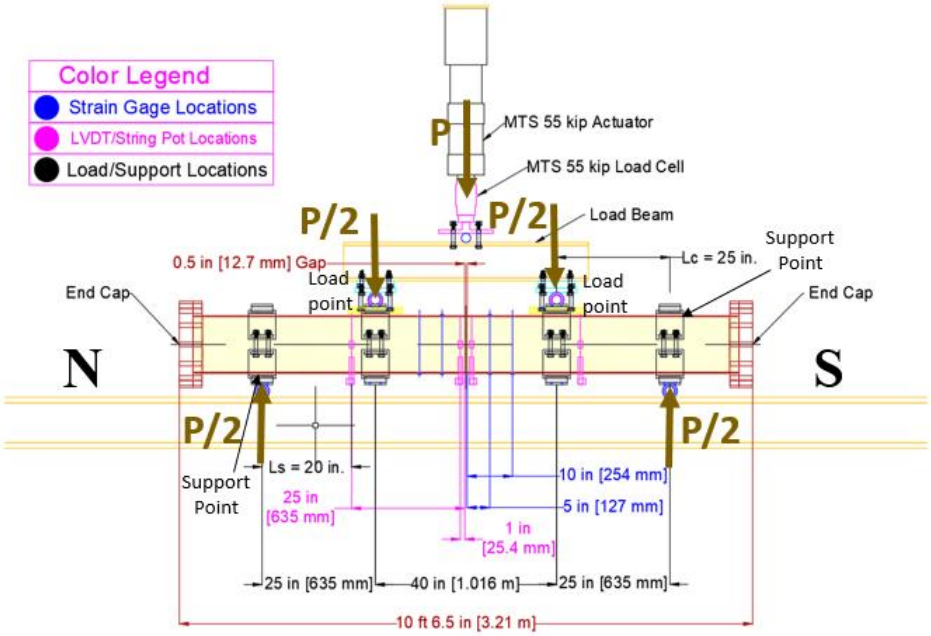

Figure 14. Schematic of four-point bending test for specimen SNES04

As shown in Figure 14 load was applied to load and support points through saddles fitted to the pipe. The saddles allowed the pipeline to return to its initial position, thus simulating deflection in the field wherein the pipeline in soil returns to its original position after rolling traffic loads move across the pipe. To duplicate this condition some tensile force is mobilized through the saddles to counterbalance the dead weight of the pipeline. North and South are shown by N and S, respectively, in Figure 14 as well as in other test schematics and photographs.

The vertical load, P, was applied to the pipeline by a 55-kip (245 kN), 6-in. (152 mm) actuator through a 55-kip (245 kN) load cell. Vertical displacements were measured through LVDTs and SPs jointly horizontally along the pipeline. Strain gages were also placed at various locations to evaluate the longitudinal and circumferential stress/strain behavior. Four practice loadings were performed on Specimen SNES04 to check that the instrumentation was functioning and to evaluate the specimen stiffness. The average water pressure sustained during testing was 65 psi (448 kPa). A pressure relief valve was connected to the specimen to maintain constant pressure. All tests were performed with live pressure. The data sampling rate was 64 Hz.

Figure 15 presents a photograph of the test set-up depicted in Figure 14. The test pipeline, MTS actuator, load cell, load beam, load contacts, and supports can be seen in the figure. The gap was centered in the load frame. Four-point bending was applied, for which the reaction locations were positioned 25 in.

(635 mm) north and south of the loading locations, which were in turn separated by 40 in. (1016 mm). This arrangement is referred to as a 25 in. – 40 in. – 25 in. configuration.

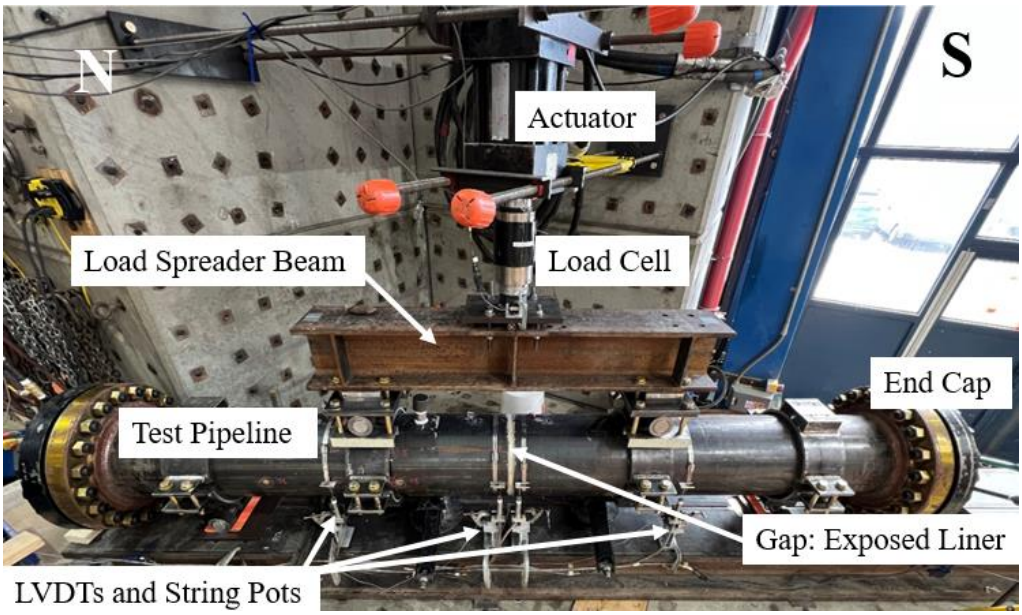

Figure 15. Photograph of four-point bending test

4.2 Axial Testing

Axial testing followed the completion of all bending tests. All specimens were axially tested in a horizontal position. 110-kip (500 kN) and 220-kip (1000 kN) actuators were used to test CU Boulder specimens, while a 55-kip (250 kN) actuator was used to test the Cornell specimen. In loading, specimens were supported by one or two supports with low friction pads to avoid potential side-loading of hardware with the specimen weight. Specimens were tested with live pressure generally. Tensile loading was predominantly performed; often the cycles were performed to avoid compression. Pressurizations and depressurizations were generally recorded. Load was transferred to the steel specimens (S01 and S02) through the flanges with rods. For the cast iron specimen, rods with three Megalug clamps were used on each end of specimen to transfer the load; this was done to avoid pulling the end cap assemblies off or open. Axial loading cycles were performed in sets.

Target displacements were determined as described above (Section 2.2), with the caveat that the responses of the pipe specimens in initial small displacement tensile tests were used to determine an effective gap width to be used in the calculations. Initial displacements less than the target displacements were first applied to assess system stiffness, test equipment performance, and ensure the specimen was not

overloaded during the first cycle. Pressurization caused COD, which generally was not subsequently zeroed (i.e., this displacement was considered to contribute to reaching the target COD). COD were measured with a variety of displacement sensors (details provided for each specimen below). Target displacements were compared to the maximum measure in testing to determine the cycle maximum had been reached. However, in Discussion of Results (Section 6), average COD are used unless otherwise noted.

4.2.1 S01 (CUB)

S01 was tested using a 110-kip (500 kN) actuator and self-reacting frame. Strain gauge location remained the same as in the bending operations (see Table 2, note channels did change), though most circumferential measures of strain were not taken. SPs and LVDTs were placed over the gap opening, fixed to the host pipe. Instrumentation details are given in Table 8. Figure 16 shows the axial test setup of S01.

Table 8. S01 axial instrumentation over the gap opening

Instrument Description	Local Instrument Name	Location	Channel No.
Horizontal String pot, Crown, over the Gap, fixed to Steel Pipe	SP18-10_C	Crown, over gap fixed to steel host pipe segments	Ch. 24
Horizontal String pot, Invert, over the Gap, fixed to Steel Pipe	SP15-10_I	Invert, over gap fixed to steel host pipe segments	Ch. 25
Horizontal String pot, North Shoulder, over the Gap, fixed to Steel Pipe	SP17-20_NS*	North shoulder, over gap fixed to steel host pipe segments	Ch. 23
Horizontal String pot, South Shoulder, over the Gap, fixed to Steel Pipe	SP19-20_SS*	South shoulder, over gap fixed to steel host pipe segments	Ch. 26
LVDT 1005, South Springline, over gap, fixed to Steel Pipe	LVDT04_1005_S	South springline, over the gap, fixed to steel host pipe segments	LVDT Ch. 4
LVDT 1001, North Springline, over gap, fixed to Steel Pipe	LVDT08_1001_N	North springline, over the gap, fixed to steel host pipe segments	LVDT Ch. 8

* Added for larger displacement cycles only

Figure 16. S01 axial test setup

Six cycles of low COD were performed, with an average COD from 0.014 in. to 0.05 in. (0.35 mm to 1.27 mm). Forty-nine subsequent cycles approached or reached the target displacement of 0.1 in. (2.54 mm), associated with an actuator displacement of 0.3 in. (7.62 mm). For the last of these cycles, some were run without pressure. Three following cycles for larger gap openings were performed with CODs around 0.4 in. (10.16 mm) associated with an actuator displacement of 0.65 in. (16.5 mm). Also, these cycles purposely included some compressive loading. The time of all cycles ranged from 1 h to 15 min. Most cycles were roughly 25 min.

After these cycles, pulling the specimen in tension to failure was attempted. In the first attempt, the maximum actuator travel was reached. The specimen was loosened from the fixtures, and the actuator's position was reset. The specimen was then pulled to failure. These operations were performed with live pressure at crosshead speeds from 0.07 in./min to 0.4 in./min (1.7 mm/min to 10 mm/min). A post-failure axial test was then performed.

4.2.2 C01 (CUB)

C01 was tested using a 220-kip (1000 kN) actuator. Strain gauge location remained the same as in the bending operations (see Table 4, note channels may have changed). SPs and LVDTs were placed over the gap opening, fixed to the host pipe. Their details are given in Table 9. Figure 17 shows the axial test setup of C01.

Table 9. C01 axial instrumentation over the gap opening

Instrument Description	Local Instrument Name	Location	Channel No.
Horizontal String pot, Crown, over the Gap, fixed to CI Pipe	SP18-10_C	Crown, over gap fixed to CI host pipe segments	Ch. 1
Horizontal String pot, Invert, over the Gap, fixed to CI Pipe	SP15-10_I	Invert, over gap fixed to CI host pipe segments	Ch. 5
Horizontal String pot, North Haunch, over the Gap, fixed to CI Pipe	SP17-20_NH	North haunch, over gap fixed to CI host pipe segments	Ch. 2
Horizontal String pot, South Shoulder, over the Gap, fixed to CI Pipe	SP19-20_SS	South shoulder, over gap fixed to CI host pipe segments	Ch. 5
LVDT 1005, South Springline, over gap, fixed to CI Pipe	LVDT06_1005_S	South springline, over the gap, fixed to CI host pipe segments	LVDT Ch. 6
LVDT 1001, North Springline, over gap, fixed to CI Pipe	LVDT07_1001_N	North springline, over the gap, fixed to CI host pipe segments	LVDT Ch. 7

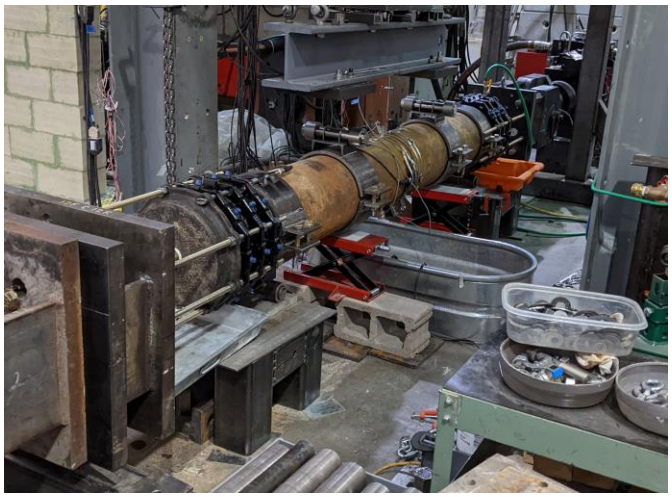

Figure 17. C01 axial test setup

Three cycles of low COD were performed, with an average COD from roughly 0.015 in. to 0.05 in. (0.38 mm to 1.27 mm). Forty-seven subsequent cycles approached or reached the target displacement of 0.1 in. (2.54 mm), associated with an actuator displacement of 0.26 in. (6.6 mm). For the last of these cycles, some were run without pressure. A single cycle was performed with CODs around 0.4 in. (10.16 mm) associated

with actuator displacement ~0.6 in. (16.5 mm) (immediately prior to pulling to failure). Typical cycle time was around 15 min.

After these cycles, the specimen was pulled to failure. This was performed with live pressure for most of the test at actuator displacement rates ranging from 0.2 in./min to 0.4 in./min (5 mm/min to 10 mm/min). The pressure was adjusted near the time of failure. Several post-failure axial test sequences were performed.

4.2.3 S02 (CUB)

S02 was tested using a 220-kip (1000 kN) actuator. Strain gauge location remained the same as in the bending operations (see Table 5, note channels may have changed). SPs were placed over the gap opening, fixed to the host pipe. Their details are given in Table 10. Figure 18 shows the axial test setup of S02.

Table 10. S02 axial instrumentation over the gap opening

Instrument Description	Local Instrument Name	Location	Channel No.
Horizontal String pot, Crown, over the Gap, fixed to Steel Pipe	SP19-20_C	Crown, over gap fixed to steel host pipe segments	Ch. 5
Horizontal String pot, Invert, over the Gap, fixed to Steel Pipe	SP17-20_I	Invert, over gap fixed to steel host pipe segments	Ch. 2
Horizontal String pot, North Shoulder, over the Gap, fixed to Steel Pipe	SP08-50_NS	North haunch, over gap fixed to steel host pipe segments	Ch. 12
Horizontal String pot, South Shoulder, over the Gap, fixed to Steel Pipe	SP11-30_SS	South shoulder, over gap fixed to steel host pipe segments	Ch. 18
Horizontal String pot, South Springline, over the Gap, fixed to Steel Pipe	SP15-10_S	South springline, over the gap, fixed to steel host pipe segments	Ch. 3
Horizontal String pot, North Springline, over the Gap, fixed to Steel Pipe	SP18-10_N	North springline, over the gap, fixed to steel host pipe segments	Ch. 1

Figure 18. S02 axial test setup

Thirteen cycles of somewhat reduced COD (relative to the target) were performed, with an average COD of 0.15 in. to 0.2 in (3.81 mm to 5 mm). Forty-five subsequent cycles approached or reached the target displacement of 0.3 in. (7.62 mm), associated with an actuator displacement of 0.43 in. (10.9 mm). Towards the last of these cycles, some were run without pressure.

A 1 in. (25.4 mm) COD axial cycle was performed at 0.3 in./min (7.6 mm/min). Immediately following this, the pull to failure was performed at the same rate. During this pull, the test was paused, the specimen was unloaded so that the springline SPs, which would have reached their limit, could be detached. The specimen was then reloaded to failure. After failure, the specimen was depressurized and repressurized. The specimen was closed off (dead pressure), and the pressure drop was recorded.

4.2.4 S03 (CUB)

S03 was axially tested in a horizontal position with a 110-kip (500 kN) actuator. In loading, the specimen was supported by two supports with low friction pads to avoid potential side-loading of hardware with the specimen weight. The specimen was tested with live pressure generally. Pressurizations and depressurizations were generally recorded. Load was transferred to the specimen through the flanges with rods. Axial loading cycles were performed in sets. Figure 19 shows S03 in the axial frame.

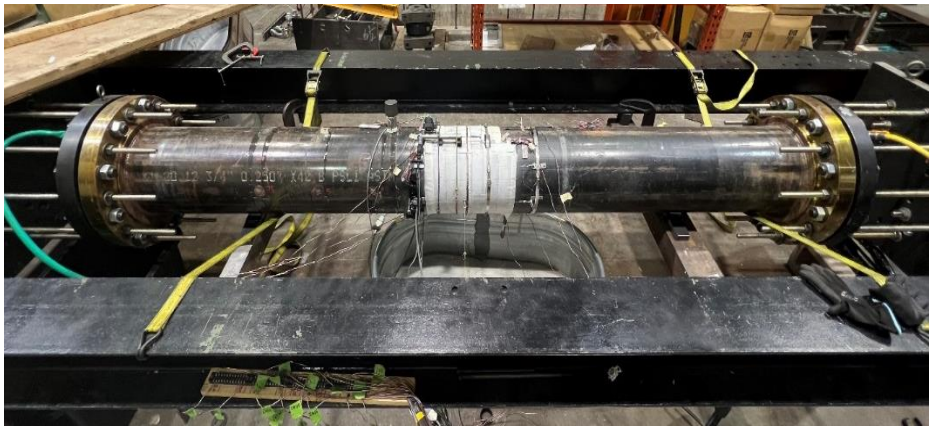

Figure 19. Axial test setup for S03

Strain gauge location remained the same as in the bending operations, though most circumferential measures of strain were not taken. String potentiometers (SPs) and linear variable differential transducers (LVDTs) were placed over the gap opening, fixed to the host pipe. Their details are given in Table 11.

Table 11. S03 instrumentation for axial test over the gap opening

Instrument Description	Local Instrument Name	Location	Channel No.
Horizontal String pot, Crown, over the gap, fixed to steel pipe	SP3-30_C	Crown, centered over gap, fixed to steel host pipe segments	Ch 19
Horizontal String pot, South, over the gap, fixed to steel pipe	SP29-10_SS	South Shoulder, centered over gap, fixed to steel host pipe segments	Ch 20
Horizontal String pot, South Shoulder, over the gap, fixed to steel pipe	SP26-30_S	South Springline, centered over gap, fixed to steel host pipe segments	Ch 12
Horizontal String pot, South Springline, over the gap, fixed to steel pipe	SP18-10_I	Invert, centered over gap, fixed to steel host pipe segments	Ch 15
Horizontal String pot, Invert, over the gap, fixed to steel pipe	SP28-20_N	North Springline, centered over the gap, fixed to steel host pipe segments	Ch 17
Horizontal String pot, North Springline, over the gap, fixed to steel pipe	SP17-20 NS (S/N: 51061210)	North Shoulder, centered over gap, fixed to steel host pipe segments	Ch 18
LVDT, West, Crown, 1.5 in. from gap edge	LVDT__10271017_C (SN 1017)	On bracket on steel, Crown, West, 1.5 in. from gap edge	LVDT Ch. 6
LVDT, West, Invert, 1.5 in from gap edge	LVDT__1005_I (SN 1005)	On bracket on steel, Invert, west 1.5 in. from gap edge	LVDT Ch. 1

Axial cycles started with three small displacement cycles with a maximum average COD of 0.082 in. (2 mm). These cycles were continued, and over the course of 18 cycles, the maximum average COD of 0.25 in. (6.35 mm) was observed. The next ca. 20 cycles had a maximum average COD progressively increasing from ~0.3 in. (7.6 mm) to ~0.5 in. (12.7 mm) over 10 sets of testing. At the end of the 38th cycle, a minor leak was observed in the pipe, and the test was paused for nearly 4 months. The remaining 12 cycles were continued at a lower level of applied deformation to complete the planned 50 cycles of thermal loading. The remaining set of cycles had an average COD of ~0.3 in. (7.6 mm) to ~0.25 in. (6.35 mm). Also, these cycles purposedly included some compressive loading. Cycles ranged from 15 min to 1 h, with the average cycle duration at roughly 25 min.

After these cycles, pulling the specimen in tension to failure was attempted. In the first attempt, the maximum actuator travel was reached. The specimen was loosened from the fixtures, and the actuator's position was reset. The specimen was then pulled to failure. These operations were performed with live pressure. A post-failure axial test was then performed.

4.2.5 S04 (Cornell)

Axial testing of Specimen SNES04 was performed to simulate thermal expansion/contraction of a pipeline with a lined round crack or lined weak joint. The specimen was tested in a horizontal position with a 55-kip (245 kN), 6 in. (152 mm) actuator, as shown in Figure 20. Low-friction Teflon pads provided support against sagging of the test pipeline under its own weight and the weight of water inside the pipeline. The loading rate was 0.026 in./min. (0.66 mm/min.). The average water pressure sustained during testing was 65 psi (448 kPa). The load was transferred to the specimen through the flanges with threaded steel rods. Those rods were attached to a steel plate that was, in turn, connected to the load cell and actuator to apply tension in the test pipeline.

Figure 21 presents a photograph of the test setup depicted in Figure 20. The test pipeline, MTS actuator, load cell, center gap, flange/end cap, and threaded rods can be seen in the figure. The center gap has been expanded due to axial pull in this figure so that the orange/brown lining is visible on the south (left) side and central part of the opening. The initial gap with white epoxy can be seen on the north (right) side of the opening.

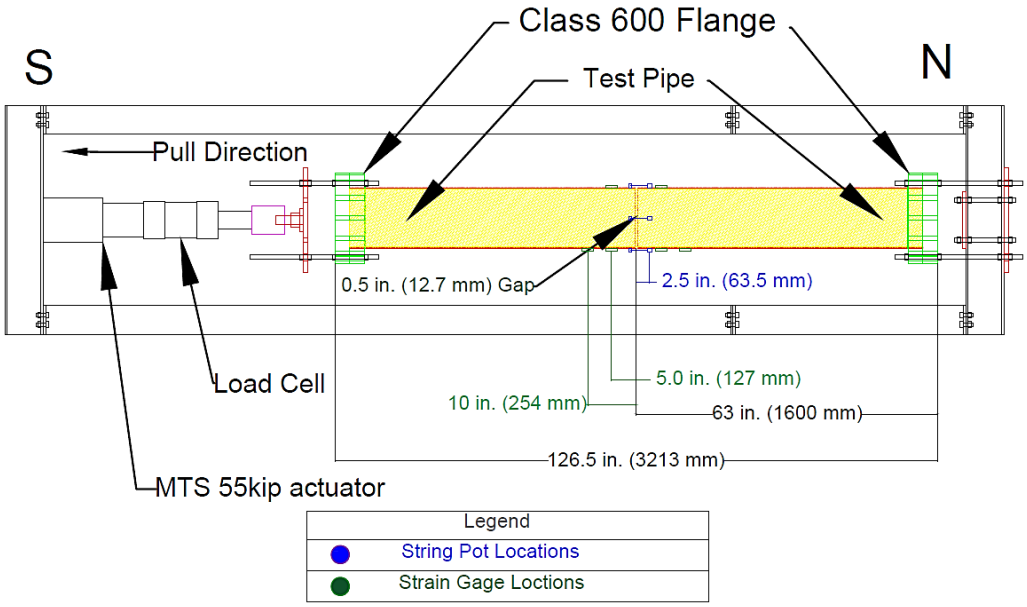

Figure 20. Schematic of axial test setup for specimen SNES04

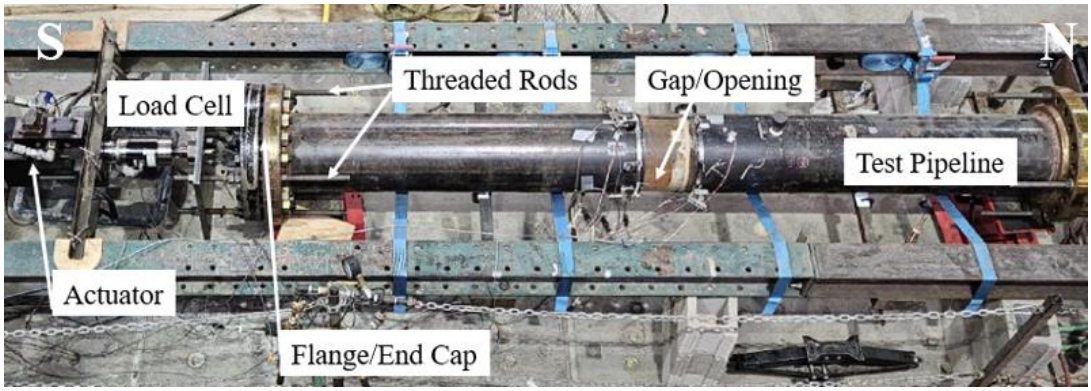

Figure 21. Axial load test setup

Table 12 lists the location, instrument type, and local instrument name. Gap opening was measured during the test as the average displacement of the six horizontal SPs. Strain gages were located north and south of the gap for axial stress/strain measurements.

Table 12. SNES04 axial load instrumentation table

Location	Instrument Description	Local Instrument Name
Crown, Fixed, Spanning Specimen Gap	Horizontal String Pot	HSP_C
Invert, Fixed, Spanning Specimen Gap		HSP_I
West Spring Line, Fixed, Spanning Specimen Gap		HSP_W
East Spring Line, Fixed, Spanning Specimen Gap		HSP_E
Crown West, Fixed, Spanning Specimen Gap		HSP_CW
Crown East, Fixed, Spanning Specimen Gap		HSP_CE
10 in. North Centerline	Invert, Axial Strain	IA_N10
	Invert, Circumferential Strain	IC_N10
5 in. North Centerline	Crown, Axial Strain	CA_N5
	Crown, Circumferential Strain	CC_N5
	Invert, Axial Strain	IA_N5
	Invert, Circumferential Strain	IC_N5
5 in. South of Centerline	Crown, Axial Strain	CA_S5
	Crown, Circumferential Strain	CC_S5
	Invert, Axial Strain	IA_S5
	Invert, Circumferential Strain	IC_S5
10 in. South of Centerline	Invert, Axial Strain	IA_S10
	Invert, Circumferential Strain	IC_S10
Actuator	MTS Load Cell (55 kip)	Actuator_Load
	MTS Actuator LVDT (±3")	Actuator_Disp_In
Pipe South End	Pressure Xducer Pipe	Pressure_Pipe
Wall Valve	Pressure Xducer Wall	Pressure_Deck

5 Test Results

5.1 S01 Results

A coarse overview of the operations performed on S01 is provided in Table 13.

Table 13. Principal loading procedures for specimen S01

General Operation	Num. of Tests or Cycles	Deformations	Test Configuration
Initial Preliminary Bends	6	~0.1° Rotation and Less	30 in. - 40 in. - 30 in.
Traffic Loading Bending Cycles	475000	0.1° Rotation	30 in. - 40 in. - 30 in.
Bends in New Configuration	2	~0.1° Rotation and Less	25 in. - 40 in. - 25 in.
Traffic Loading Bending Cycles	25000	0.1° Rotation	25 in. - 40 in. - 25 in.
Parallel Excavation	1	0.2° Rotation, 0.6° Rotation	25 in. - 40 in. - 25 in.
Traffic Loading Bending Cycles	100000	0.1° Rotation	25 in. - 40 in. - 25 in.
Parallel Excavation	1	0.2° Rotation	25 in. - 40 in. - 25 in.
Axial Cycles	56	0.04 in. to 0.4 in. of COD	Weight-supported axial testing
Pull to Failure	2	~12 in. of total COD	Weight-supported axial testing
Axial Deformation to Assess Friction	1		Weight-supported axial testing

5.1.1 S01 Bending Results

Figure 22 shows load-time data and LVDT displacement-time data from the first set of traffic cycles of S01. These cycles are a representative sample of traffic loading cycles performed on S01. Traffic loading of S01 entailed a mechanical load up to roughly 3.3 kips (14.7 kN). A small lifting load was required to support the pipe and return the frame's actuator to its initial position (typically about 300 lbs (1.3 kN)).

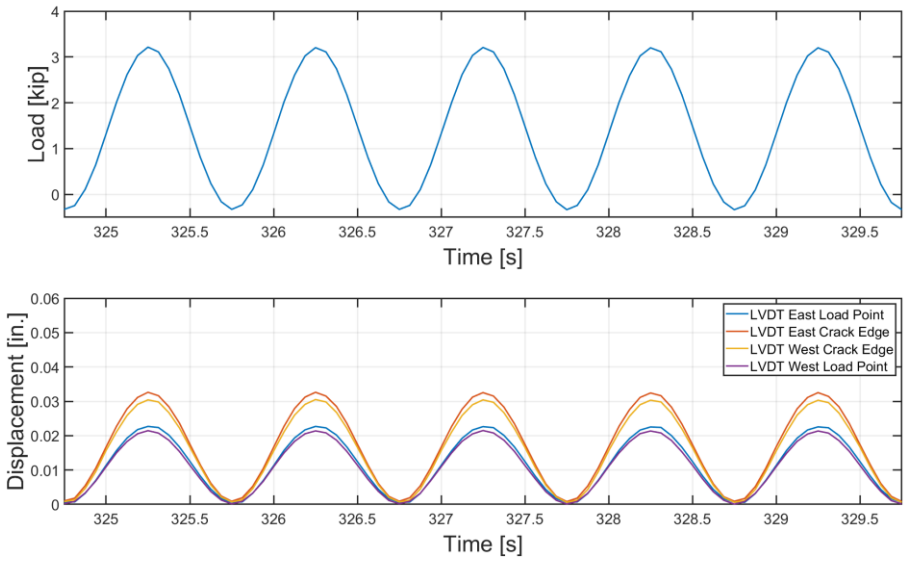

Figure 22. Load and LVDT displacements vs. time from the first set of traffic cycles for S01

Figure 23 shows applied moment vs. global rotation curves at different cycle counts from a single set of traffic cycles conducted at a rate of 2 Hz. The cycle count shown in the legend represents the overall number of cycles applied and corresponds to cycles 5, 1000, and 15000 within the set. The figure shows consistent applied moment while a marginal shift in the maximum and minimum rotation values occurred over cycling.

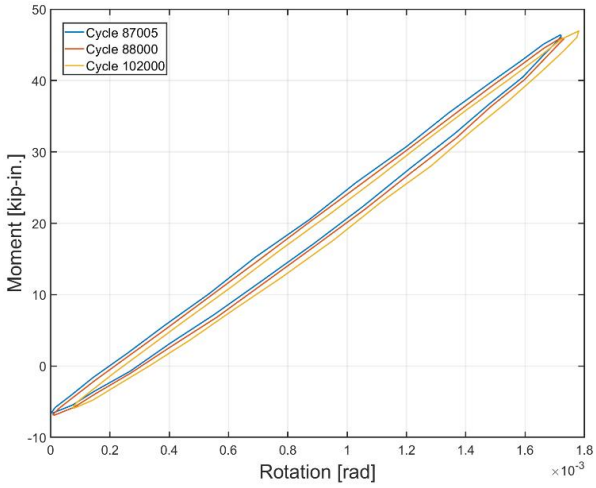

Figure 23. Measured moment vs. global rotation curves from a single block of traffic loading for S01

Figure 24 presents load vs. time and pressure vs. time data for a block of traffic cycles in which the pressure was released. Without pressure, a positive shift in the load is observed; the actuator applies more compressive load to reach the same displacement level and less tensile load to return to the initial position.

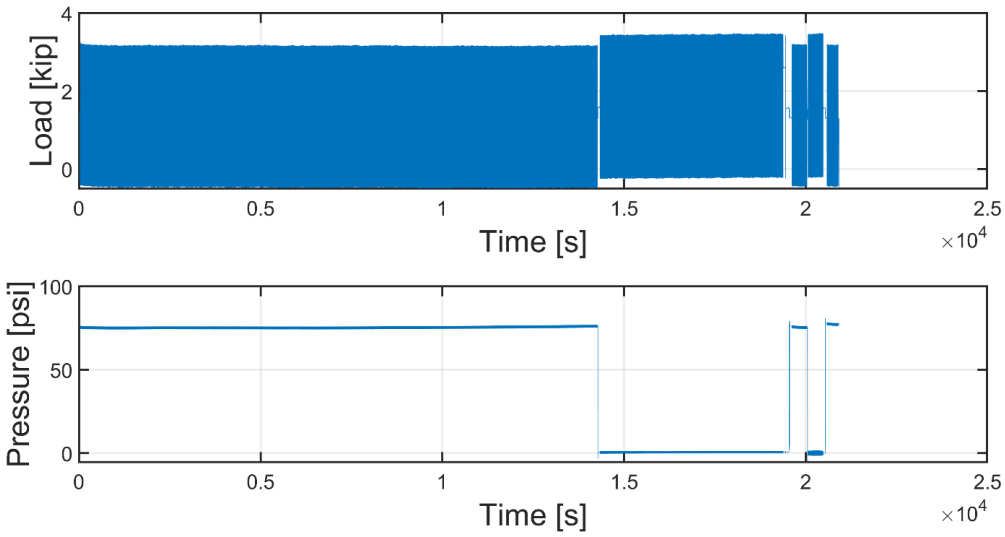

Figure 24. Load and pressure vs. time for S01 traffic loading cycles with variable internal pressure

Figure 25 shows the effect of pressure on moment vs. global rotation curves for pressurized (dead pressure) and zero pressure conditions from traffic loading. Their behavior is similar but shifted due to the increase in applied load corresponding to the decrease in pressure. The effect of loading frequency is shown in Figure 26. The hysteresis loop expands slightly at a greater frequency.

Figure 27 shows the stiffness over the traffic cycles before the parallel excavation bends and the change in bending configuration. This stiffness was calculated by fitting the slope on the moment-global rotation curves (over the middle) of the loading portion of cycles. It varies only slightly throughout testing. Figure 28 shows the stiffness from traffic cycles after changing the bending configuration from 30 in. –40 in. – 30 in. to 25 in. – 40 in. – 25 in. (762 mm – 1016 mm - 762 mm to 635 mm – 1016 mm – 635 mm). A comparison between these two figures shows some reduction in system stiffness due to the change in configuration.

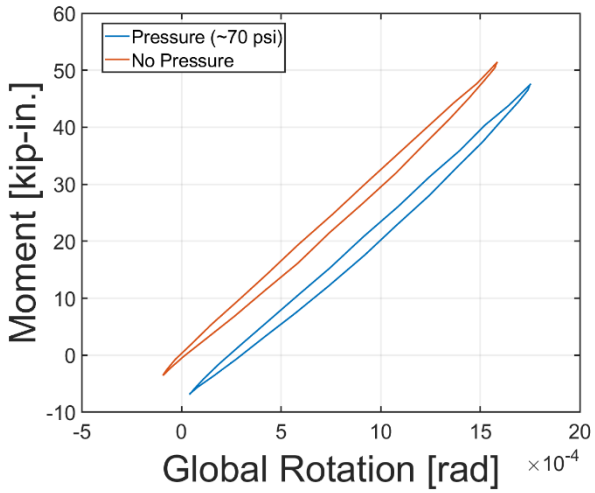

Figure 25. Moment vs. rotation with and without pressure for S01

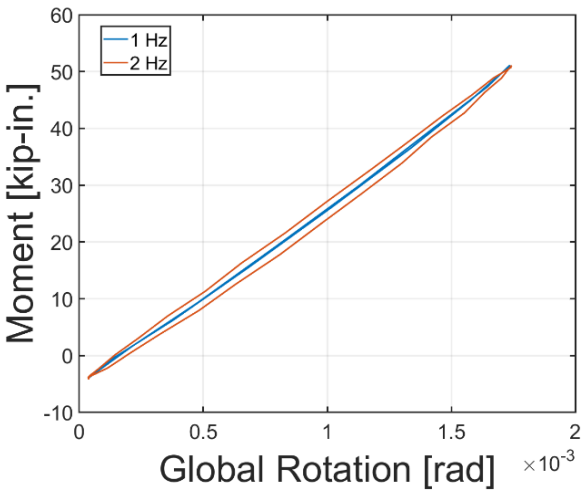

Figure 26. Moment vs. rotation at 1 Hz and 2 Hz for S01, 1 Hz rotation uniformly shifted for visualization of hysteresis

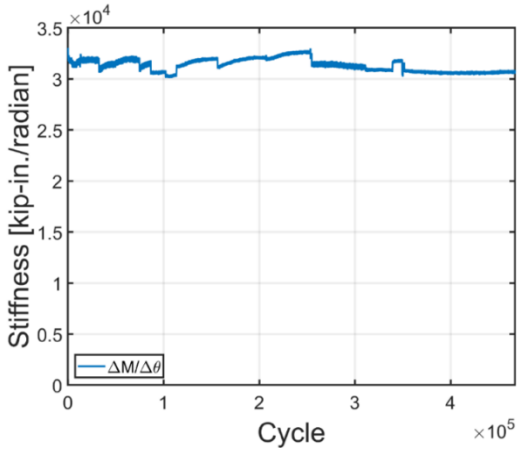

Figure 27. Stiffness vs. cycle count for S01, stiffness calculated with the slope of the moment against the rotation angle

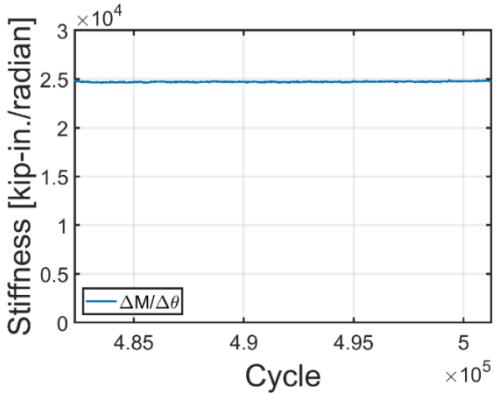

Figure 28. Stiffness vs. cycle count for S01, prior to parallel excavation deformation in the 25 in. – 40 in. – 25 in. configuration

Figure 29 presents half cycles at various cycle counts, further demonstrating consistent system stiffness from cycles 1 to 470,000. Because displacement devices were zeroed at the start of each testing block, global rotation was also assumed to be zero at the start of cycling. While the initial location of the actuator (zero-load point) between cycle sets did generally increase due to slight progressive specimen bending, the

marginal differences in absolute values of rotation in this figure are not intended to indicate the magnitude of progressive deformation relative to the specimen's initial state.

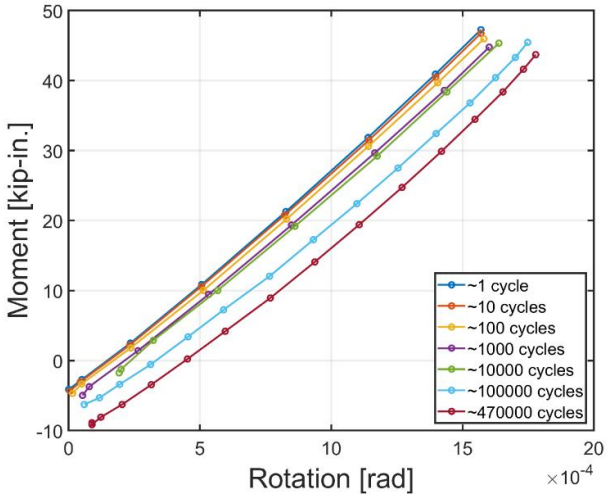

Figure 29. Moment-rotation half cycles at specific counts for S01

Figure 30 shows the moment vs. global rotation relationship for the parallel excavation deformations. A maximum moment of 194 kip-in. (22 kN-m) was reached.

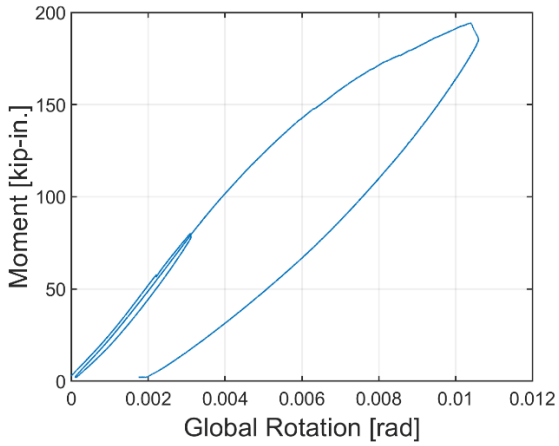

Figure 30. Moment vs. rotation relation in parallel excavation loading for S01

In Figure 31, the stiffness measured in the traffic cycles after the adjacent excavation deformations (AED) are given. The stiffness is consistent over these cycles and about 10% less than the stiffness measured prior to the AE loading with the same configuration (Figure 28).

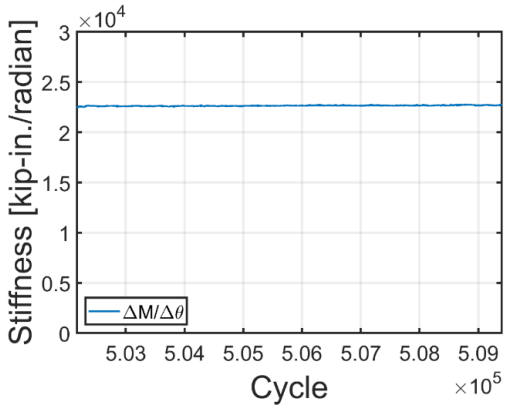

Figure 31. Stiffness vs. cycle count for S01, after parallel excavation deformation in the 25 in. – 40 in. – 25 in. configuration

5.1.2 S01 Axial Testing Results

Figure 32 shows the axial load and displacement measures about the gap opening plotted against a pseudo-time index for most axial cycles of S01. The difference in displacements measured at various positions around the gap opening is attributed to the deformed shape of the specimen imposed by the previous lateral deformation cycles. Note here that the displacement measures are all zeroed from the initial test zero for the purpose of effective visualization only. For purposes of analysis, the displacement data is zeroed at the beginning of each set of cycles.

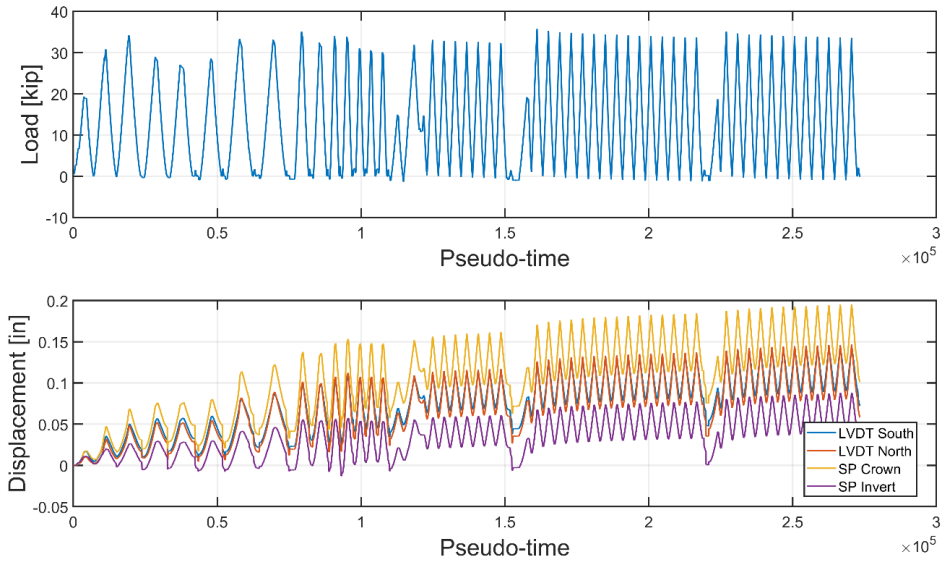

Figure 32. Load and CODs in axial cycling for S01

The load vs. the average COD from an early axial cycle (2nd) is given in Figure 33. A small load drop occurs near the peak displacement, which is likely associated with minor debonding between the host pipe and IRP. The COD is a calculated average of the crown, invert, and springline measures for this and all other specimens unless specifically noted otherwise.

Figure 34 is a plot of the displacements from the various sensors about the gap opening in a typical axial cycle of S01. The increase in COD because of pressurization is not shown, but the values of displacement reflect this, as well as the previous loading history within the set. Figure 35 shows load vs. the average displacement of the gap opening for several typical cycles of S01. Axial cycles with and without pressure are shown in Figure 36.

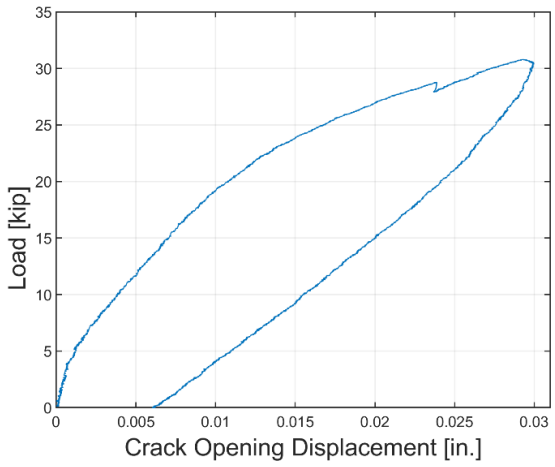

Figure 33. Early axial cycle, load vs. COD for S01

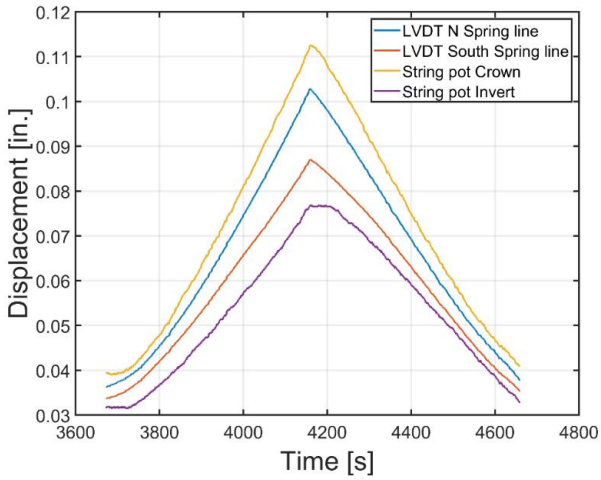

Figure 34. Displacements from LVDTs and SPs for S01 in a typical axial cycle

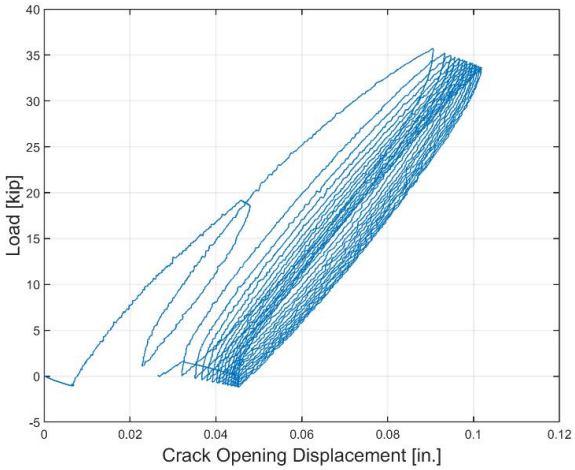

Figure 35. Axial cycles, load vs. COD for S01

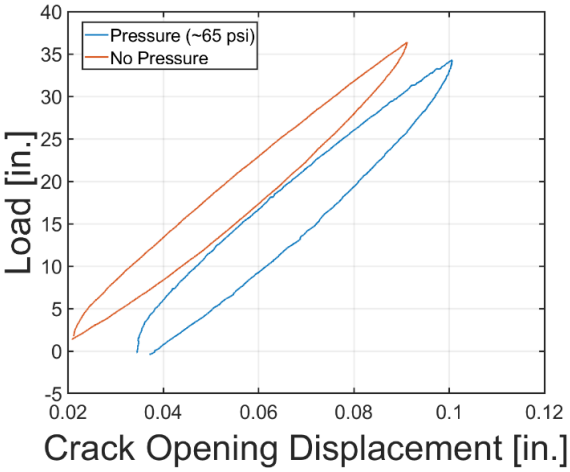

Figure 36. Axial cycles with and without pressure for S01

The loading portions of select axial cycles are shown in Figure 37. These cycles are the first full cycles of loading blocks. Initial portions, in which the load rises sharply without a substantial increase in COD for cycles 16 and 51, have been removed, as this behavior deviates from the load and COD relationship of each cycle. This behavior seems to result from the initial half cycle applied prior to these cycles (cycles 16 and 51 followed the previous half cycles). Load and displacement for all cycles have been zeroed for ease in visualization of the change in response.

The larger displacement cycles are shown in Figure 38. Here, the average COD is taken from the string pots only, and thus is weighted more towards the opening near the crown.

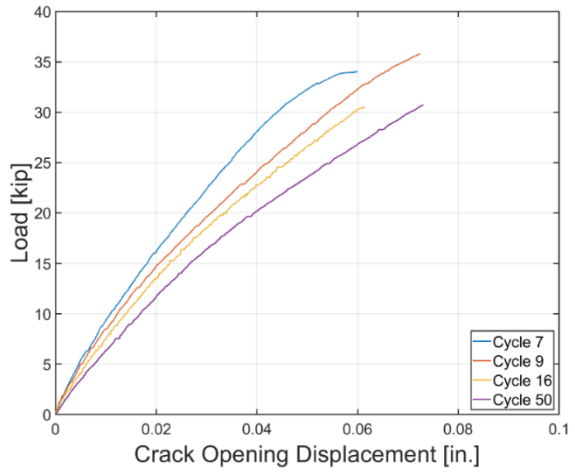

Figure 37. Select axial cycles of S01 showing loading portions

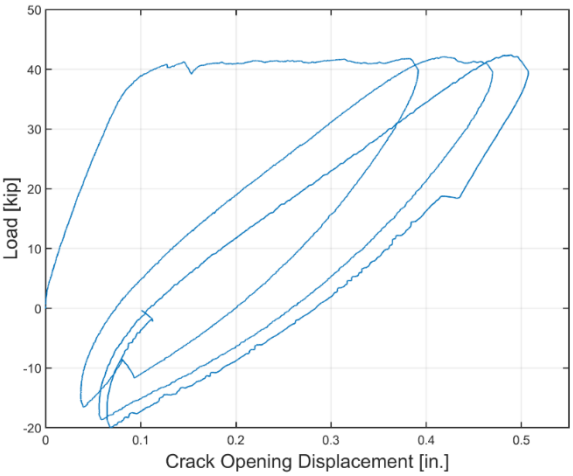

Figure 38. Axial displacement cycles to 0.4 in. featuring compressive loading for S01

5.1.3 S01 Pull to Failure Results

Figure 39 shows the load vs. average COD for the large pulls of S01. Displacement values are zeroed at the start of each test. As above, the average COD is taken from the string pots only. Failure occurred by detachment at approximately 56 kips (250 kN). After the first pull, the specimen recovered about 4 in. (101.6 mm) of COD, as measured from the string pots. Thus, the total COD to failure from its cycled state was about 12 in. (304.8 mm).

Leakage occurred at the west side of the gap, between the steel and liner. This failure indicates water is backtracking between the detached region from inside the pipe. The gap opening from an overhead view is shown in Figure 40 while Figure 41 provides images of the specimen before, after the first pull, and at the end of the test.

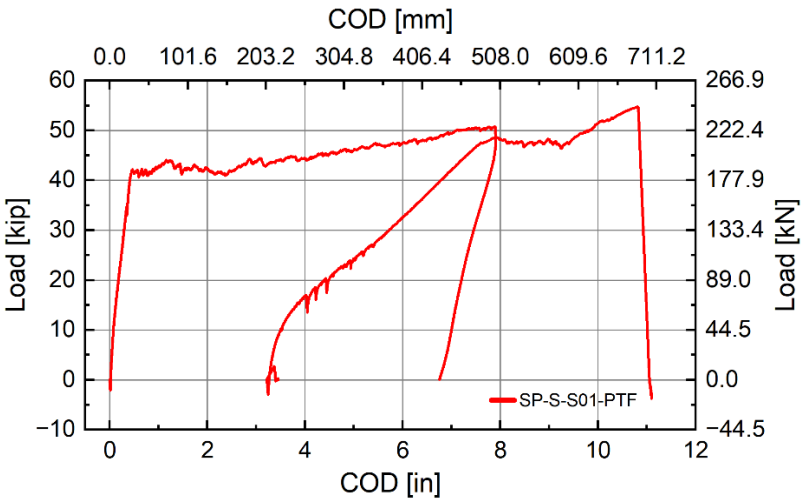

Figure 39. Large axial pulls of S01, load vs. COD

Figure 40. Gap opening in the failed specimen S01

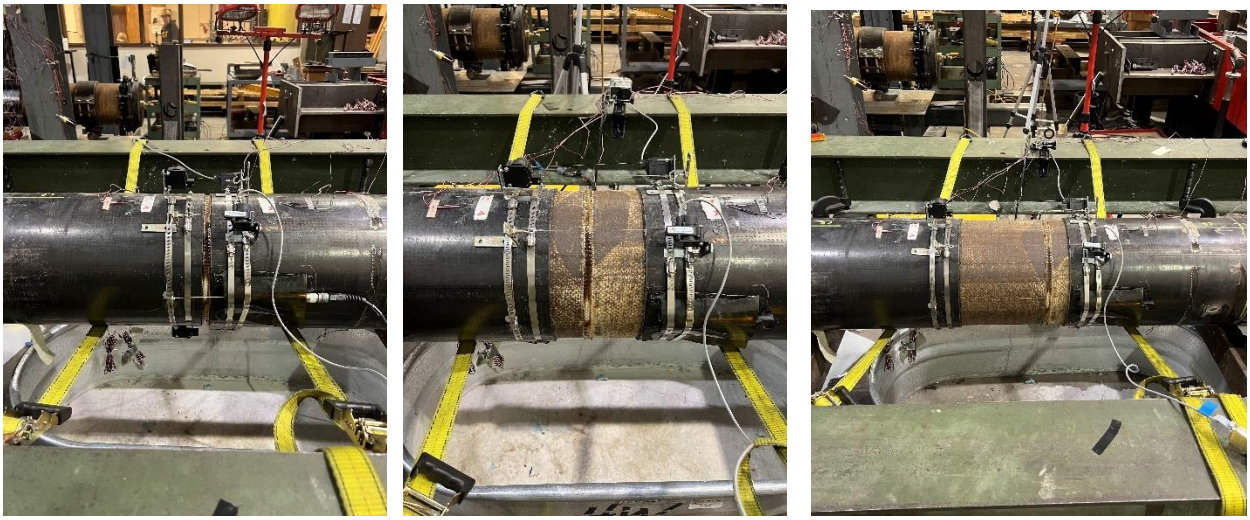

Figure 41. S01 (a) before pull to failure, (b) after first pull applied, and (c) after final detachment

5.2 C01 Results

An overview of the operations performed on C01 is provided in Table 14.

Table 14. Principal loading procedures for specimen C01

General Operation	Number of Tests or Cycles	Deformations	Test Configuration
Initial Preliminary Bends	4	~0.1° Rotation	25 in. - 40 in. - 25 in.
Traffic Loading Bending Cycles	485000	0.12° Rotation	25 in. - 40 in. - 25 in.
Parallel Excavation	1	0.3° Rotation, 0.8° Rotation	25 in. - 40 in. - 25 in.
Traffic Loading Bending Cycles	100000	0.15° Rotation	25 in. - 40 in. - 25 in.
Parallel Excavation	1	0.2° Rotation	25 in. - 40 in. - 25 in.
Axial Cycles	50	0.015 in. to 0.4 in. of COD	Weight-supported axial testing
Pull to Failure	1	~5 in. of total COD	Weight-supported axial testing
Axial Deformation to Assess the Interface	4		Weight-supported axial testing

5.2.1 C01 Bending Results

Load-time and LVDT displacement-time data are shown for early traffic cycles in Figure 42. The load levels are similar to traffic loading in C01. Nearly 600,000 traffic cycles were applied to C01 in the course of its evaluation.

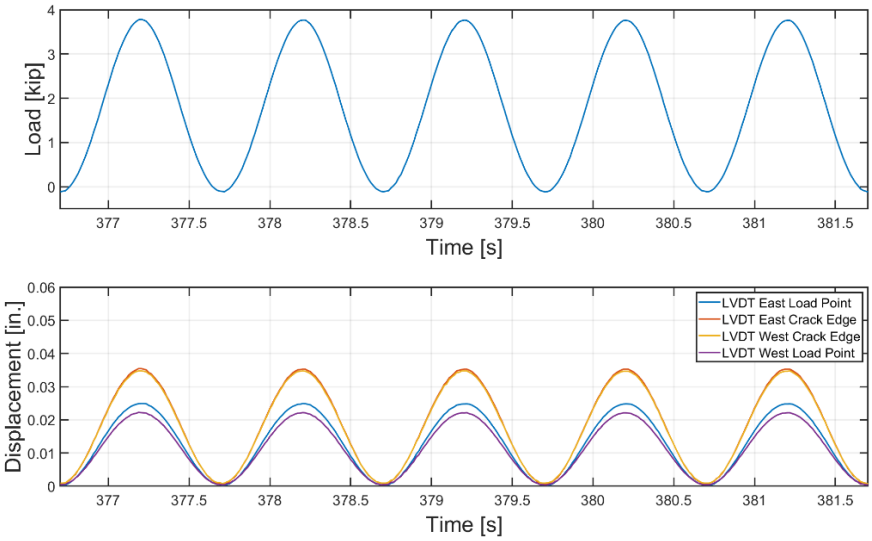

Figure 42. C01 traffic cycles, showing load vs. time and LVDT displacements vs. time from the third set of traffic cycles of C01

Figure 43 shows applied moment global rotation curves at different cycle counts from a single set of traffic cycles performed at a rate of 2 Hz. The rotation values increase throughout the testing. Load changes slightly throughout the testing.

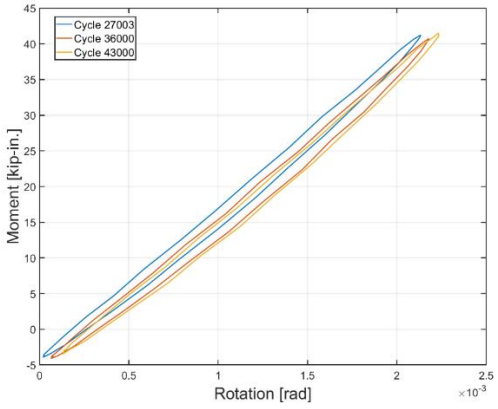

Figure 43. Measured moment global rotation curves from a single block of traffic loading for C01 (within block cycle counts are 3, 9000, 16000)

Figure 44 shows load and pressure against time for a block of traffic loading on C01, in which the pressure was released for some cycles. A positive shift in the load is observed, corresponding to the release of pressure.

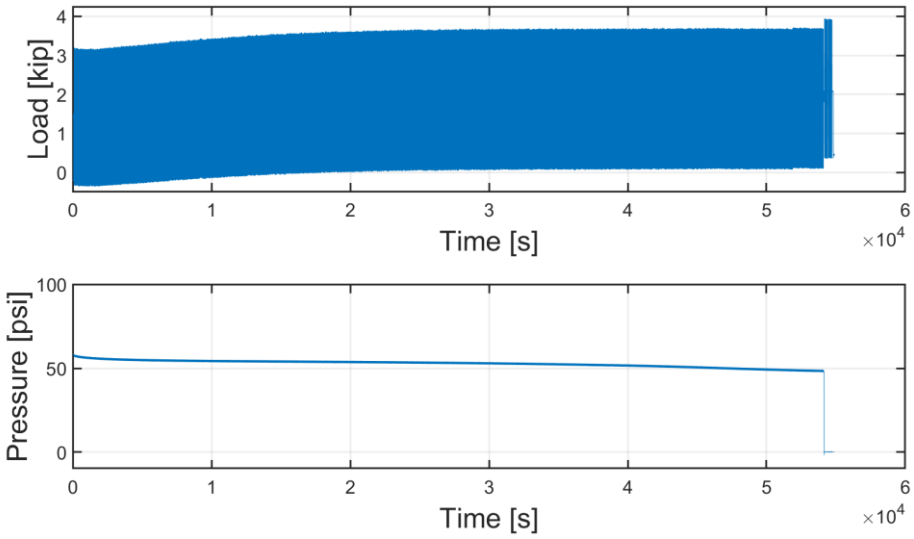

Figure 44. Load and pressure vs. time for C01

Figure 45 shows the moment vs. rotation relationship at various frequencies. The hysteresis loop expands slightly at a greater frequency. The stiffness (slope fit) varied slightly over the course of about 480,000 cycles, as shown in Figure 46. For practical purposes, the stiffness is constant.

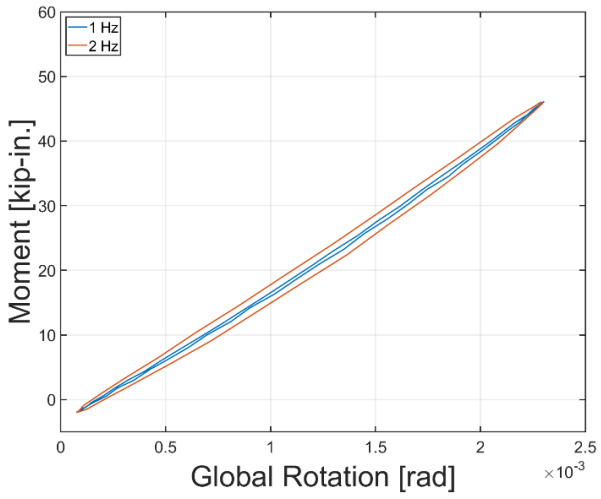

Figure 45. Moment - rotation at 1 Hz and 2 Hz for C01

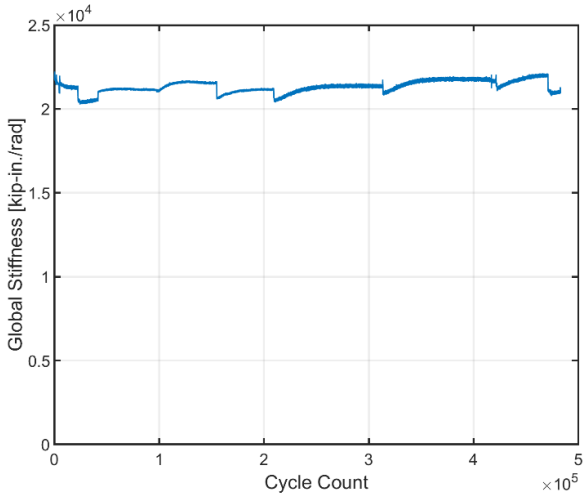

Figure 46. Stiffness vs. cycle count prior to parallel excavation deformations for C01

Figure 47 shows moment vs. global rotation curves for various cycles prior to parallel excavation loading. Again, the stiffness remains relatively constant across the first 500,000 cycles. Because displacement devices were zeroed at the start of each testing block, global rotation was also assumed to be zero at the start of cycling. While the initial location of the actuator (zero-load point) between cycle sets did generally increase due to slight progressive specimen bending, the marginal differences in absolute values of rotation in this figure are not intended to indicate the magnitude of progressive deformation relative to the specimen's initial state.

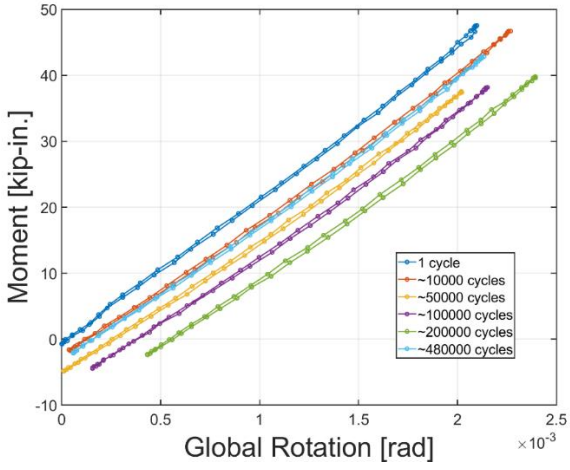

Figure 47. Moment vs. rotation cycles at specific counts for C01

The moment rotation curve for the deformations simulating parallel excavation is shown in Figure 48. A maximum moment of 128 kip-in. (14.5 kN-m) was reached. The figure also compares this relationship calculated with only the west LVDT and the string pots attached to the loading saddles. They show reasonable agreement until beyond $11x10^{-3}$ radians of deformation, perhaps suggesting that the increased deflection on the west side of the pipe is associated with more debonding on the west side of the pipe.

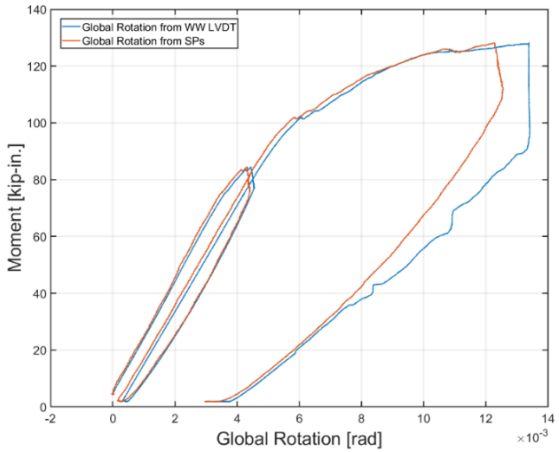

Figure 48**. Moment vs. rotation relation in parallel excavation loading SPs vs LVDT for C01**

Figure 49 shows stiffness of the specimen before and after the adjacent excavation deformation. After adjacent excavation, stiffness was reduced by 30%. Unfortunately, the traffic cycles (post parallel excavation deformation) were not run with an appropriate sample rate due to a lack of storage. As a result, the stiffness calculation per cycle had to be performed with a simple maximum–minimum approach. The storage error has been fixed for future tests.

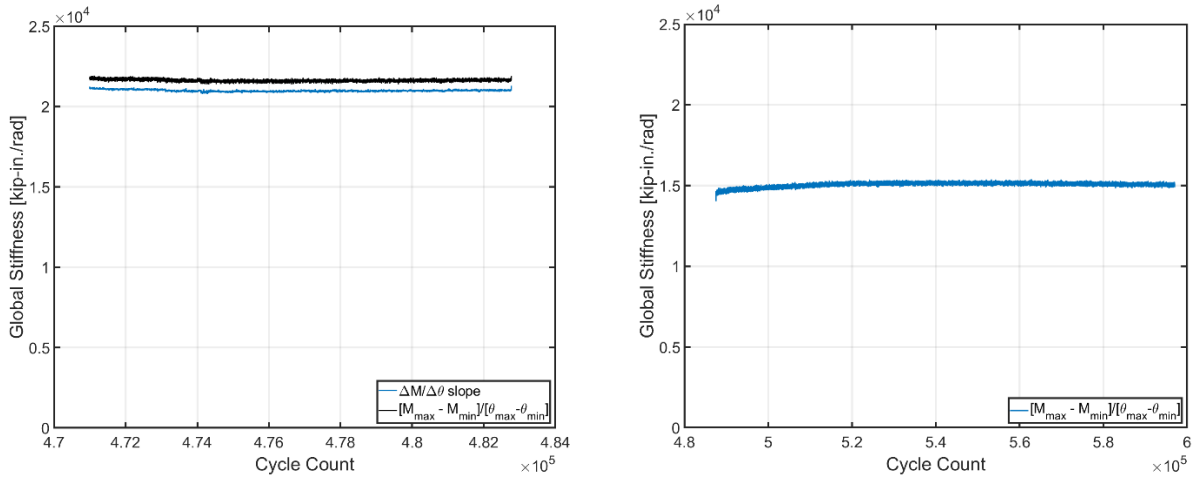

(a) (b)

Figure 49. Stiffness vs. cycle count for C01, (a) before the parallel excavation event, (b) after the parallel excavation event

5.2.2 C01 Axial Testing Results

Figure 50 shows the axial load and displacement measures about the gap opening plotted against a pseudo-time index for most axial cycles of C01. The difference in displacements measured at different positions over the gap is attributed to deformed shape of the structure imposed by the previous lateral deformation. Note here that the displacement measures are zeroed from the first point recorded in the first axial cycle for ease of visualization. In analysis, each separate test run is treated as an individual set of cycles, and displacements are zeroed from the first point of the individual set.

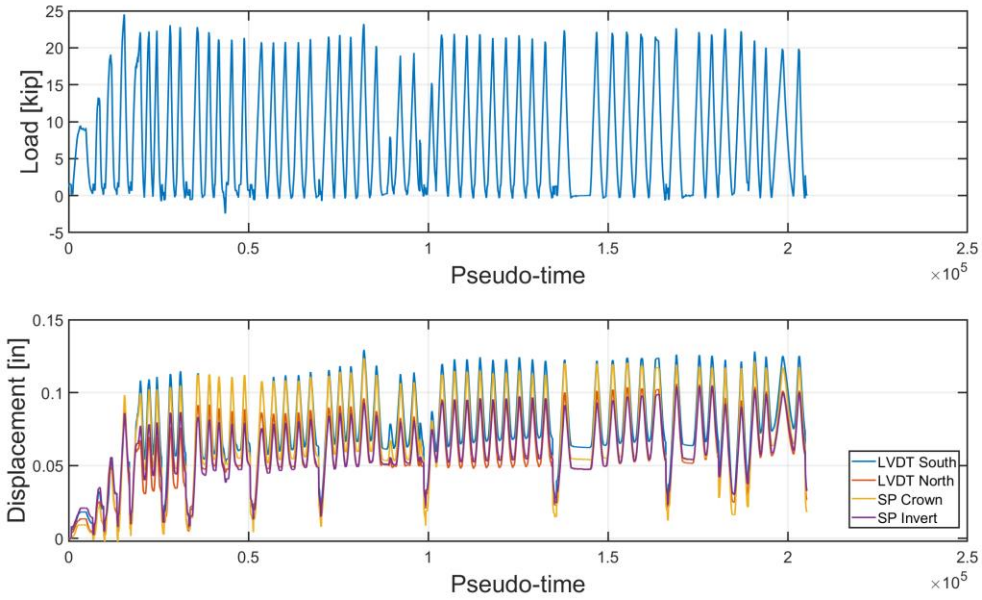

Figure 50. Load and CODs in axial cycling for C01

Load vs. the average displacement about the gap from the first axial cycle with a moderately sized displacement (~0.025 in.) is given in Figure 51. A small load drop occurs near the peak displacement. Average COD was calculated with the crown, invert, and springline measures for C01 unless specifically noted otherwise.

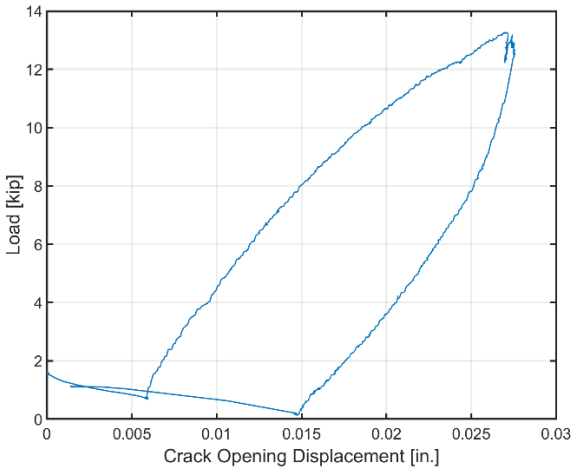

Figure 51. Early axial cycle, load vs. COD for C01

Figure 52 is a plot of displacements from various sensors about the gap in a typical axial cycle. The increase in COD because of pressurization is not shown, but the values of displacement reflect this, as well as the previous loading history within the set.

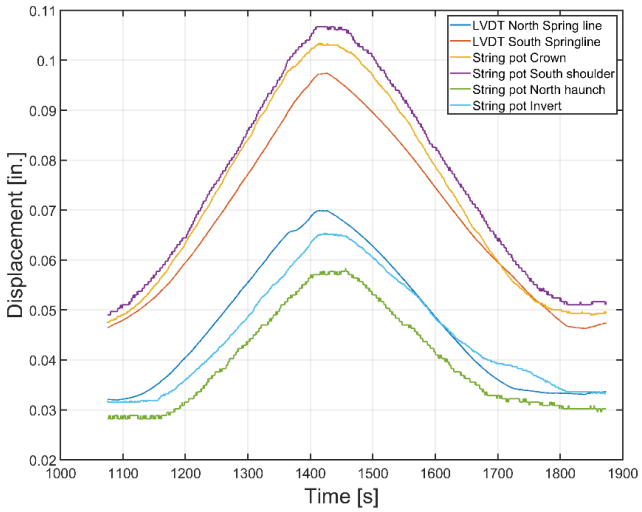

Figure 52. Displacements from LVDTs and SPs for C01 in a typical axial cycle

Figure 53 shows load vs. the average displacement about the gap for several typical cycles of C01 (cycles 9 to 14).

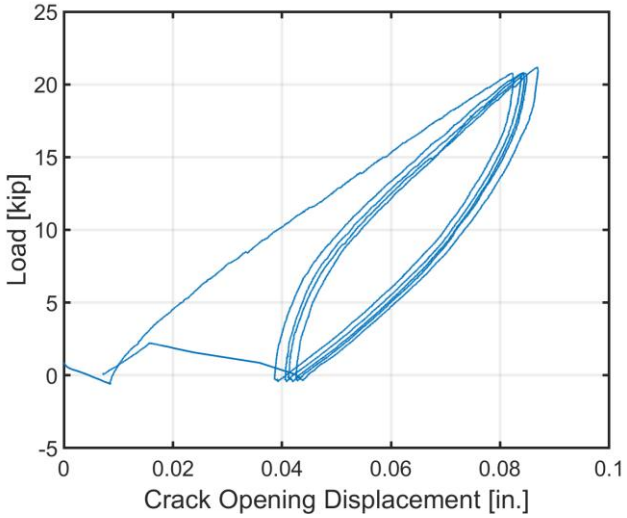

Figure 53. Axial cycles; load vs. COD for C01 (cycles 9-14)

The loading portions of select axial cycles are shown in Figure 54. These cycles are the first full cycles of loading blocks. Load and displacement for all cycles have been re-zeroed here for visualization of the change in specimen stiffness and overall response.

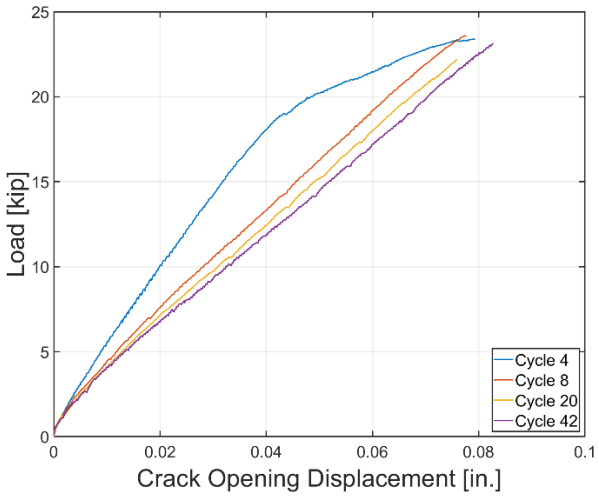

Figure 54. Initial axial loading cycles of C01 showing the first cycle

5.2.3 C01 Pull to Failure Results

The load vs. COD behavior for the pull to failure is shown below in Figure 55 (featuring the small cycle to 0.4 in. (10.16 mm) of COD). Only the string pots were used to calculate the average COD, as the LVDTs reached the extent of their measurement range. Ultimate capacity was reached at about 5 in. (127 mm) of COD under a load of roughly 48 kips (214 kN) and was characterized by detachment of the IRP from the host pipe. Leakage occurred as water backtracked from the detached region from inside the pipe (west segment). Leaking is visible between the host pipe and liner. A post-test photo of the specimen is shown in Figure 56.

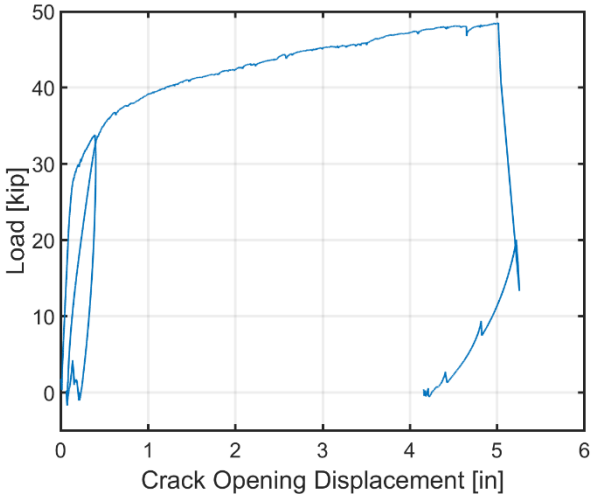

Figure 55. Load vs. COD: pull to failure inclusive of initial cycle of 0.4 in. (25.4 mm) displacement for C01

Figure 56. The gap opening in the failed specimen for C01

5.3 S02 Results

An overview of the operations performed on S02 is provided in Table 15.

Table 15. Principal loading procedures for specimen S02

General Operation	Number of Tests or Cycles	Deformations	Test Configuration
Initial Preliminary Bends	2	~0.24° Rotation	26.5 in. - 40 in. – 26.5 in.
Traffic Loading Bending Cycles	500000	0.22° Rotation	26.5 in. - 40 in. – 26.5 in.
Parallel Excavation	1	1.5° Rotation	26.5 in. - 40 in. – 26.5 in.
Parallel Excavation	1	3.3° Rotation	26.5 in. - 40 in. – 26.5 in.
Traffic Loading Bending Cycles	100000	0.22° Rotation	26.5 in. - 40 in. – 26.5 in.
Parallel Excavation	1	1.4° Rotation	26.5 in. - 40 in. – 26.5 in.
Axial Cycles	59	0.15 in. to 1 in. of COD	Weight supported axial testing
Pull to Failure	1	~7.5 in. of total COD	Weight supported axial testing
Axial Deformation to Assess the Interface	2		Weight supported axial testing

5.3.1 S02 Bending Results

Figure 57 shows load-time data and LVDT displacement-time data for cycles from the first set of traffic loading for S02. Note the LVDT displacements shown have been pressure corrected (this effect is small for all LVDT displacements barring the LVDT at the center of the AQUA-PIPE™ IRP). These cycles are a selected representative set of the cyclic traffic loading performed on S02. Traffic loading of S02 entailed a mechanical load to roughly 2.7 kips (12 kN). A small lifting load was required to support the pipe and return the frame's actuator to its initial position (approximately 400 lbs (1.8 kN)). 600,000 traffic cycles were applied to S02.

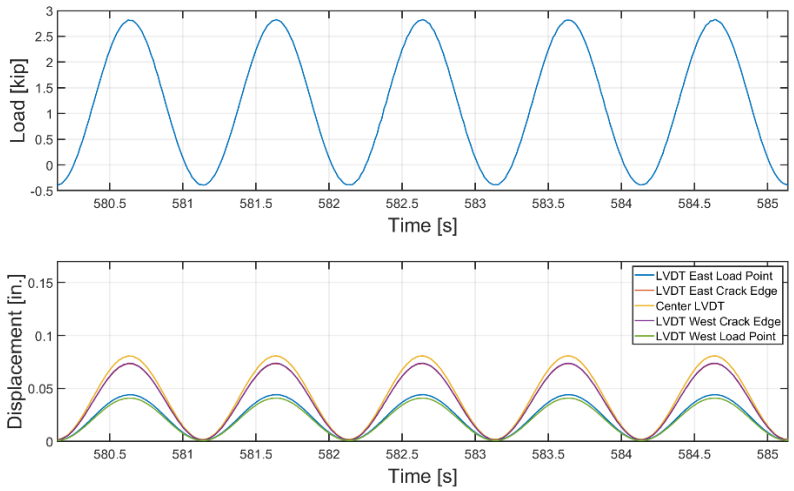

Figure 57. S02 traffic cycles, showing load vs. time and LVDT displacements vs. time from the first set of traffic cycles for S02

Figure 58 shows applied moment vs. global rotation curves at different cycle counts from one set of traffic cycles. Compared values were tested at a rate of 2 Hz and the cycle count shown in the legend is the overall cycle count (the block count for these cycles is 5, 10001, 28000). The cycle magnitudes remained relatively constant with a slight shift in the applied rotation and resulting moment over the course of cycling.

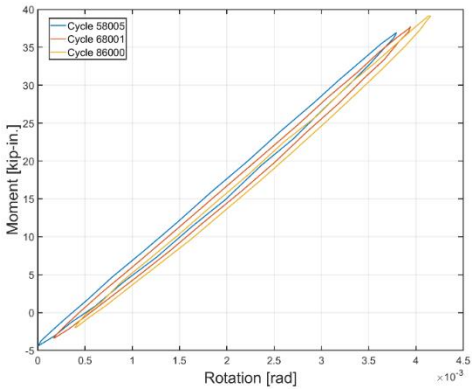

Figure 58. Measured moment vs. global rotation curves from a single block of traffic loading for S02

Figure 59 presents load and pressure against time for a representative block of traffic cycles on S02, in which the pressure was released for some cycles. It was observed that a positive shift in the load corresponding to a drop in pressure to zero.

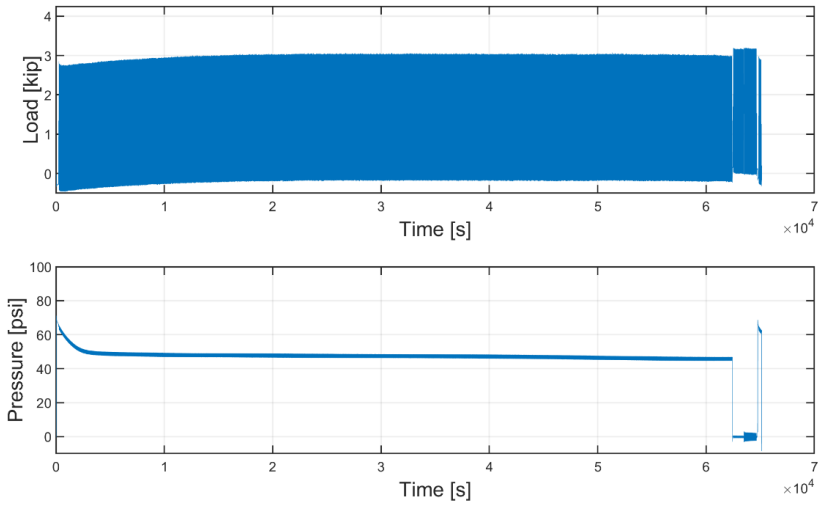

Figure 59. Load and pressure vs. time for S02

Figure 60 shows two cycles around the 500,000-cycle mark at 1 Hz and 2 Hz. The hysteresis loop expands slightly at a greater frequency. Figure 61 shows the specimen stiffness calculated for each cycle of traffic loading prior to adjacent excavation cycles. The stiffness was calculated by fitting the slope of the loading portion of the moment-rotation curves from the traffic cycles. The stiffness for S02 remained relatively constant through the first 500,000 cycles.

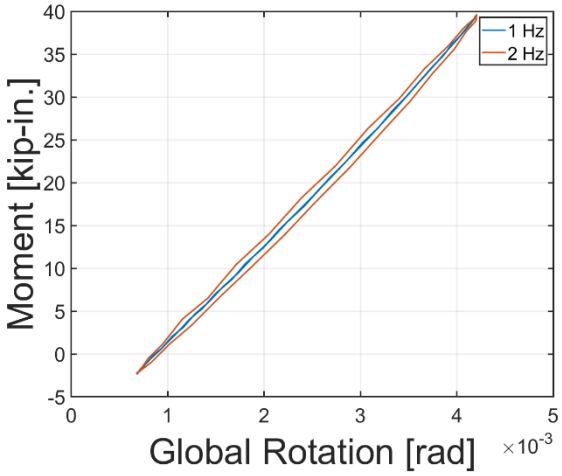

Figure 60. Moment vs. rotation at 1 Hz and 2 Hz for S02 (0.004 rad =0.23 deg)

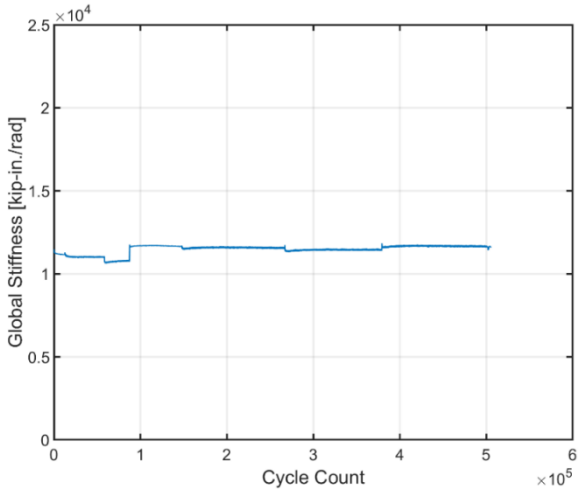

Figure 61. Stiffness vs. cycle count prior to imposing parallel excavation deformations for S02

Figure 62 shows moment vs. global rotation curves at specific cycles prior to parallel excavation loading. Stiffness remains relatively consistent across the first 500,000 cycles.

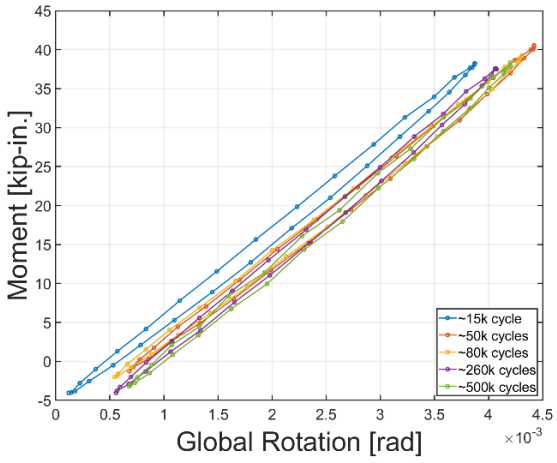

Figure 62. Moment vs. rotation cycles at specific counts for S02

The moment vs. global rotation behavior of S02 in the first smaller parallel excavation is given in Figure 63, while Figure 64 shows the moment vs. rotation behavior of the larger parallel excavation deformation. Rotations were calculated from both LVDTs and string pots, as readings from one LVDT gave unstable results (perhaps from the core slightly catching on the assembly under significant deformation and associated misalignment). The maximum moment attained in the large AED was 162 kip-in. (18 kN-m).

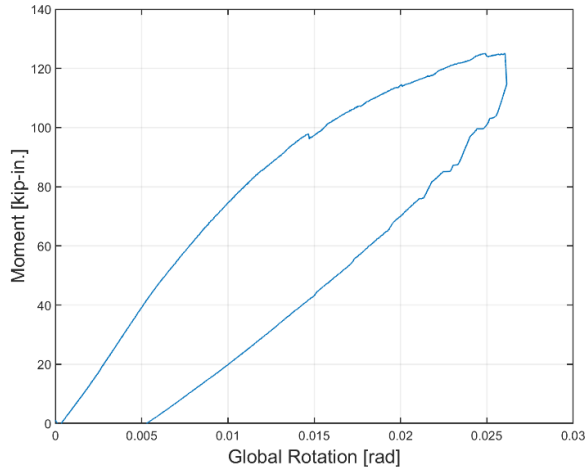

Figure 63. Moment vs. rotation in the initial parallel excavation for S02

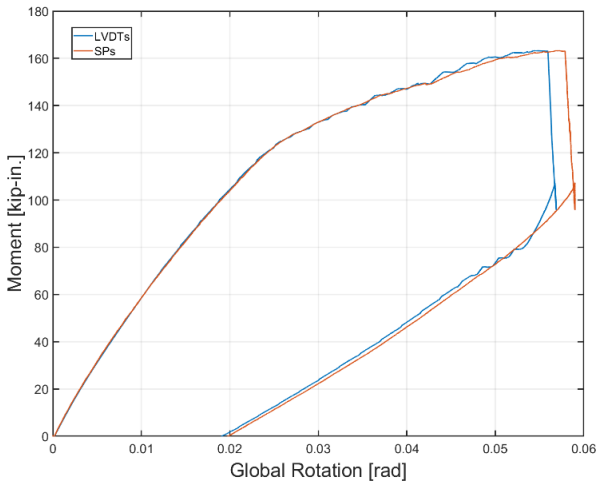

Figure 64. Moment vs. rotation in the large parallel excavation for S02 (SPs and LVDTs)

In Figure 65 the stiffness measured in the traffic cycles after the parallel excavation deformations is given. The stiffness appears reduced (~20%) to that measured prior to the excavation loading (see Figure 59).

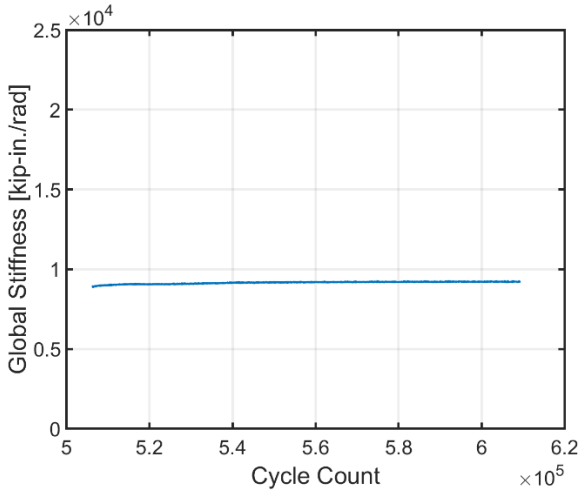

Figure 65. Stiffness vs. cycle count for S02, after parallel excavations

5.3.2 S02 Axial Testing Results

Figure 66 shows the axial load and displacement measures about the gap opening plotted against a pseudo-time index for the axial cycles of S02. The difference in displacements measured at different positions over the gap is attributed to the deformed shape of the specimen imposed by the previous lateral deformation.

The displacement measures shown in Figure 65 are zeroed from the first recorded displacement of the first axial cycle for the purpose of effective visualization of the gap opening behavior over time. When analyzing the data, each set of cycles is treated as an individual set and zeroed accordingly (using the first point of each individual set). Note that the invert SP was adjusted before the last several cycles; for these cycles, the displacement values recorded by this SP were shifted for easier visualization.

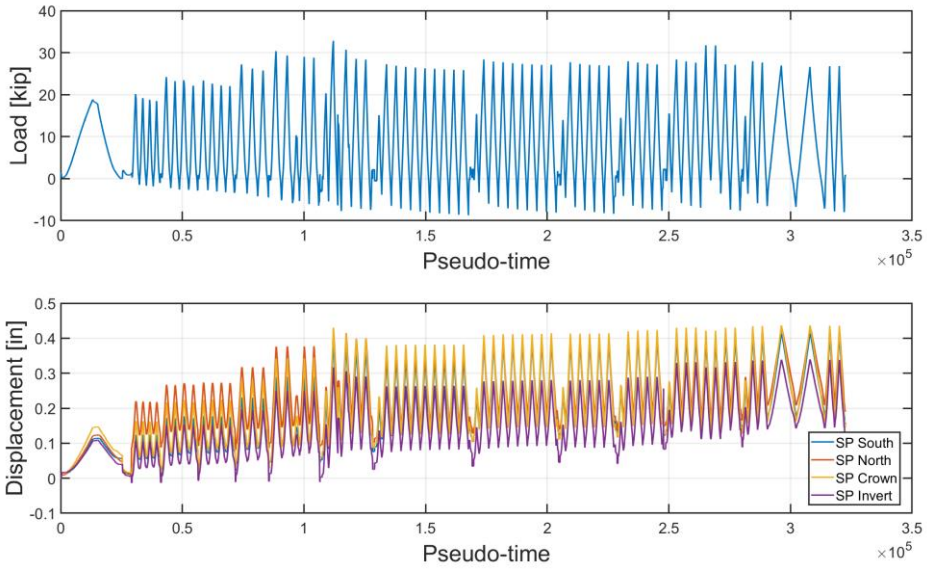

Figure 66. Load and CODs in axial cycling for S02

The load vs. the average COD from the first axial cycle for S02 is given in Figure 67. Figure 68 is a plot of the displacements from the various sensors about the gap opening in a typical axial cycle of S02.
Figure 69 shows load vs. the average displacement of the gap for several typical cycles of S02. Axial cycles with and without pressure are shown in Figure 70.

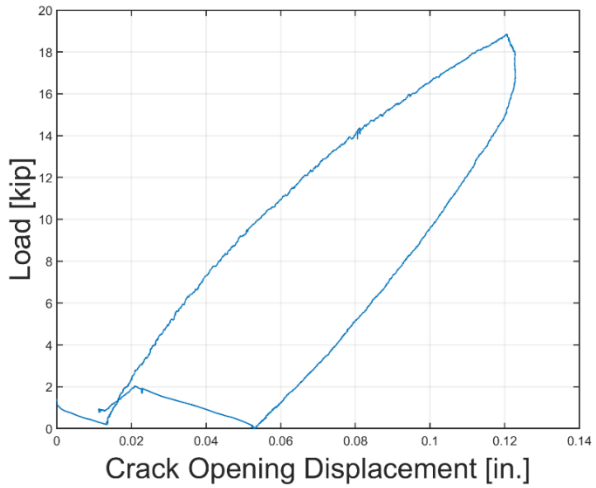

Figure 67. First axial cycle, load - COD for S02

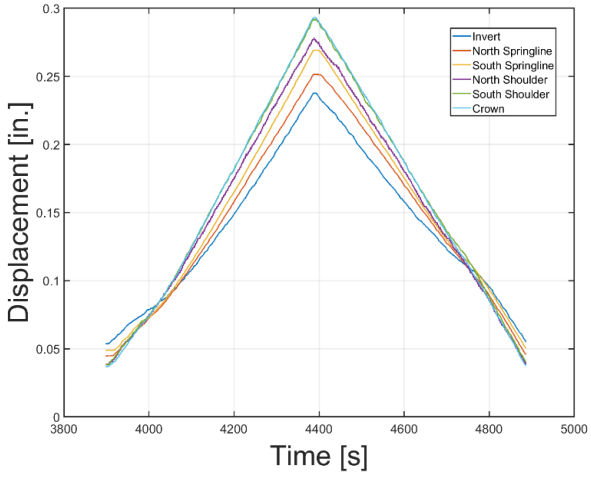

Figure 68. Displacements from SPs for S02 in a typical axial cycle

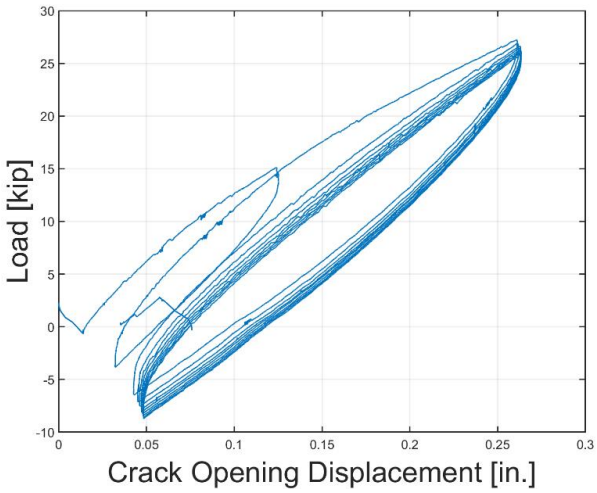

Figure 69. Axial cycles, load - COD for S02

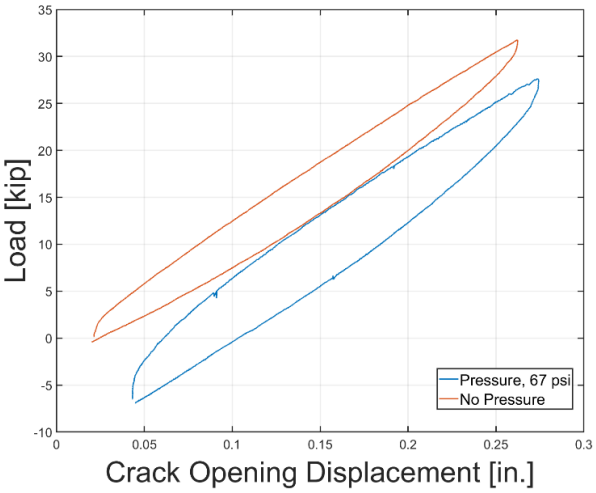

Figure 70. Axial cycles with and without pressure for S02

Axial displacement cycles are shown in Figure 71. The axial displacement cycles with 15 min durations before and after two axial cycles with 50 min durations are shown. The 50 min cycles are also shown in Figure 72.

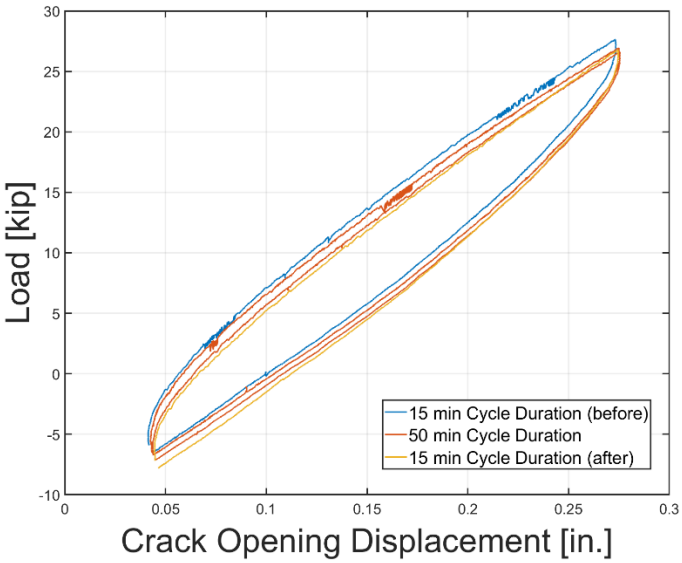

Figure 71. Axial loading for S02 at two loading rates (cycle durations)

The loading portions of select axial cycles are shown in Figure 72. These cycles are the first full cycles of loading blocks. Initial portions, in which the load rises sharply without a substantial increase in COD (this behavior deviates from the load COD relationship of each cycle) for cycles 25 and larger have been removed. This behavior seems to result from the initial half cycle applied prior to this cycle (the plotted cycles 25 and above occurred after such half cycles). Load and displacement for all cycles have been re-zeroed here for ease in visualization of the change in response.

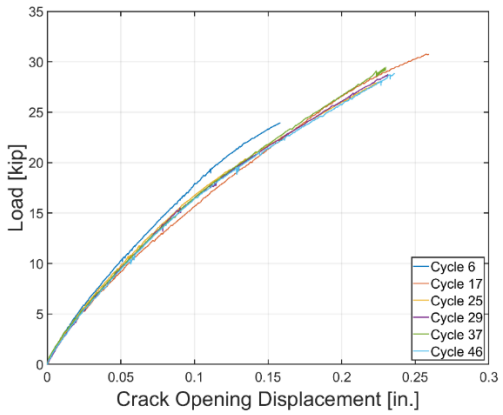

Figure 72. Select axial cycles of S02 showing loading portions

5.3.3 S02 Pull to Failure Results

Figure 73 shows the load vs. average COD, which includes the pull to failure for S02. Displacement values are zeroed at the start of each test. The first load-unload cycle is the 1 in. COD cycle. The second unloading occurred to remove the SPs at the springlines. The average COD used here is taken from the crown, invert, and shoulder string pots (measurement favors deformation towards crown of the pipe). Failure occurred by detachment at about 47 kips (209 kN). The total COD to failure from its cycled state was about 7.7 in. (195.6 mm) total from test start.

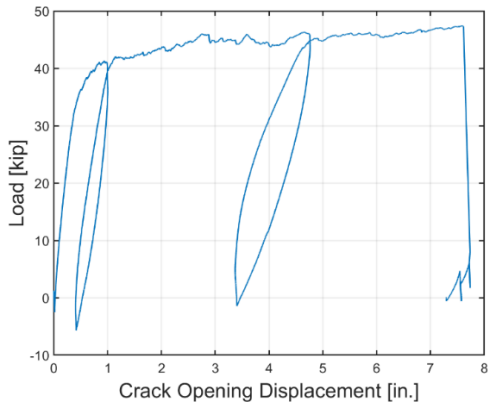

Figure 73. Large axial pulls of S02, load vs. COD

The pull to failure, now zeroed from the start of this pull and with the unloading and reloading for string pot detachment removed is shown in Figure 74.

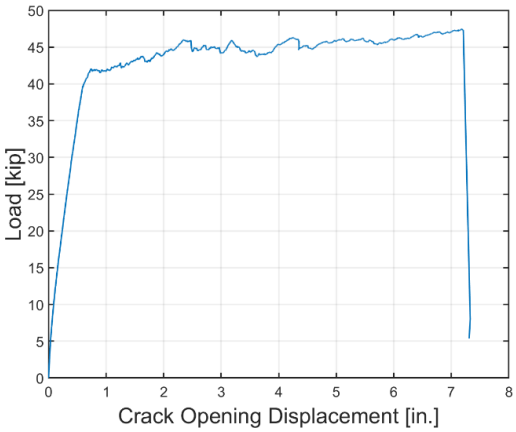

Figure 74. Pull to failure of S02, load vs. COD

The failure, marked by the large drop in load, was observed on the specimen at the holes in the host pipe on the east side of the specimen. These holes had been lined over and were observed to be leaking. On re-pressurization, leaking was also observed between the steel and liner at the gap on the east side. Figure 75 shows the extent of gap opening at failure.

Figure 75. Image of (a) gap opening after S02 pull to failure and (b) removal of liner from host pipe after test

5.4 S03 Results

An overview of the operations performed on S03 is provided in Table 16.

Table 16. Principal loading procedures for specimen S03

General Operation	Number of Tests or Cycles	Nominal Deformation Level	Test Configuration
Initial Preliminary Bends	4	~0.10° Rotation	25 in. - 40 in. - 25 in.
Traffic Loading Bending Cycles	498000	0.12° Rotation	25 in. - 40 in. - 25 in.
Parallel Excavation	1	1° Rotation, 2.6° Rotation	25 in. - 40 in. - 25 in.
Traffic Loading Bending Cycles	15000	0.25° Rotation	25 in. - 40 in. - 25 in.
Traffic Loading Bending Cycles	85000	0.4° Rotation	25 in. - 40 in. - 25 in.
Axial Cycles	52	0.03 in. – 0.55 in. COD	Weight supported axial testing

Table 17 provides additional details about the axial pull cycles and displacements performed on S03. The target gap opening changed over the course of testing as a reflection of the change in specimen stiffness, which results from progressive debonding over cycles.

Table 17. General axial pull sequence on S03

General Operation	Cycle Counts	Deformations
Small Displacement Cycles	3	Max avg. gap opening at 0.082 in.
Further Cycles	18	Max avg. gap opening at 0.25 in.
Next CA	20	Max avg. gap opening increasing from 0.3 to 0.5 in.
**Test Paused due to a minor leak and waiting on S04 results to reach the same level of mechanical aging*		
Rest Cycles	12	Max avg. gap opening at 0.25 ~ 0.3in.
First attempt Pull to Failure	1	
Second attempt Pull to Failure	1	

5.4.1 S03 Bending Results

Figure 76 shows load vs. time data for a representative set of traffic cycles for S03. Traffic loading deformation of S03 entailed a mechanical load to roughly 4 to 5 kips (17.8 to 22.2 kN). During traffic loading of S03, the maximum applied loading decreased over the first half of the sequence and then remained relatively constant; however, the amplitude remained consistent throughout the sequence. Figure 77 shows the global rotation over time in this set of traffic cycles. The rotation progresses over time with a similar trend to that of the load.

Figure 78 portrays the load and the four LVDT displacements measured against time over typical traffic cycles for S03. Similarly, Figure 79 provides the moment vs. rotation response of S03 at various cycles during a set of approximately 20,000 cycles, demonstrating a relatively consistent response (cycle rate of 2 Hz; cycle count shown in the legend is the overall count, equivalent to within the block loading cycles of 10, 1000, 5000, 17000). Figure 80 shows two cycles around the 500,000-cycle mark at 1 Hz and 2 Hz. While the hysteresis loop expands at greater frequency, the target rotations and resulting moment remain relatively consistent.

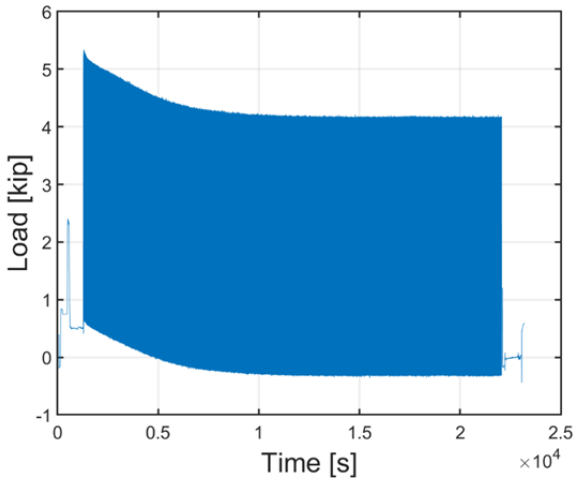

Figure 76. Load vs. time in S03 set of traffic cycles

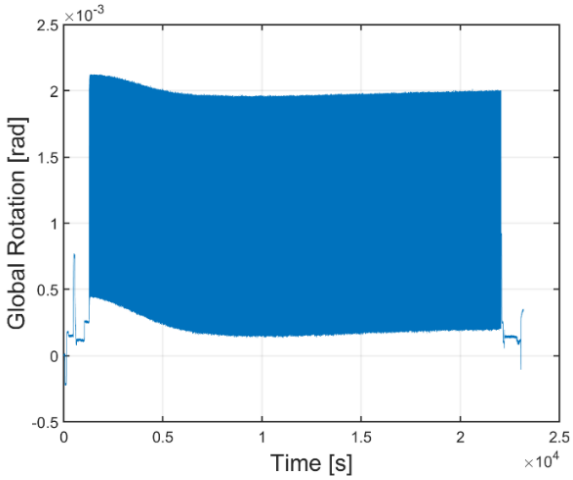

Figure 77. Global rotation vs. time in S03 set of traffic cycles

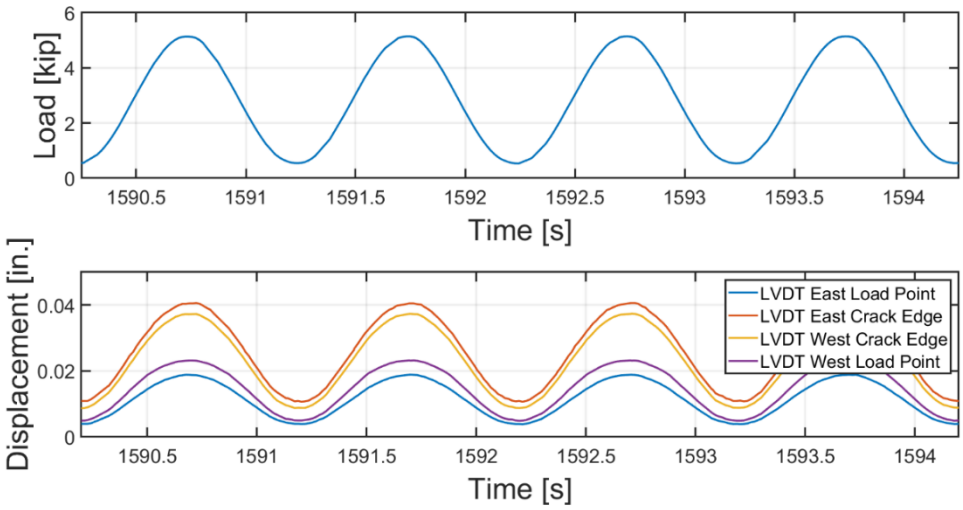

Figure 78. Measured load and LVDT displacements for four cycles against time

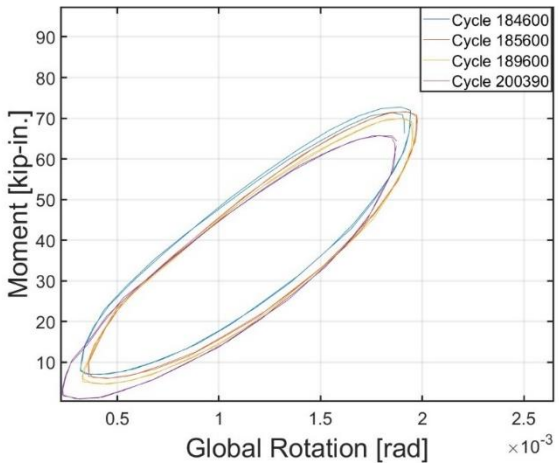

Figure 79. Measured moment vs. global rotation curves from a single block of traffic loading for S03

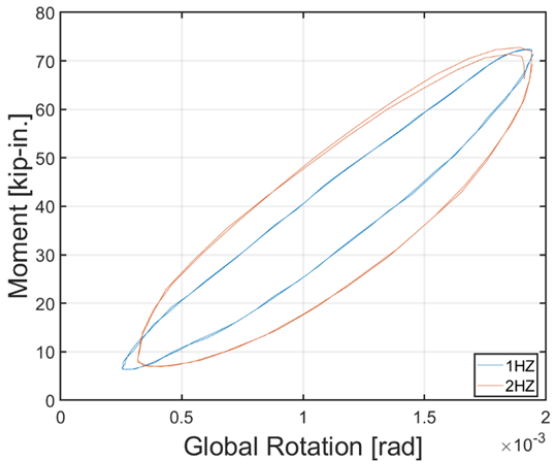

Figure 80. Moment vs. rotation at 1 Hz and 2 Hz for S03

Figure 81 shows the stiffness calculated from fitting the slope of the loading portion of moment vs. rotation curves from the traffic cycles prior to the parallel excavation loading for S03. While some variation was measured during early cycles, the stiffness remained relatively constant after about 150,000 cycles.

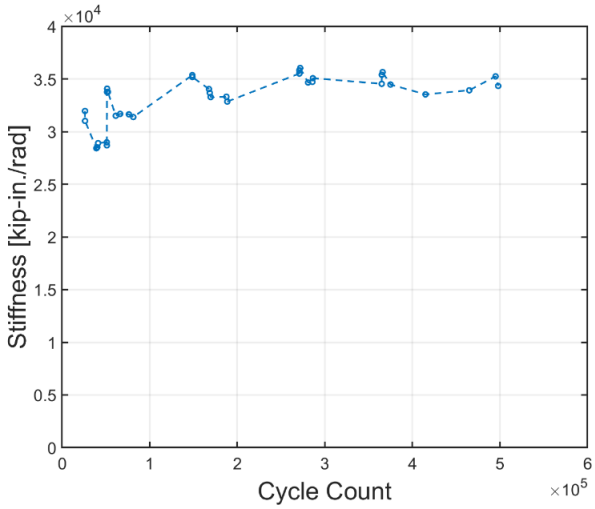

Figure 81. Stiffness measured from moment vs. rotation responses of traffic cycles prior to the adjacent excavation

Figure 82 shows the recorded load and LVDT displacements against time during the parallel excavation bend testing. During the tests, popping/cracking noises were heard. The bracket for the LVDT near the gap

edge on the west side of the specimen debonded from the pipe during the test. The observed spike and flatline from LVDT West Gap Edge were due to the bracket for the LVDT debonding from the pipe.

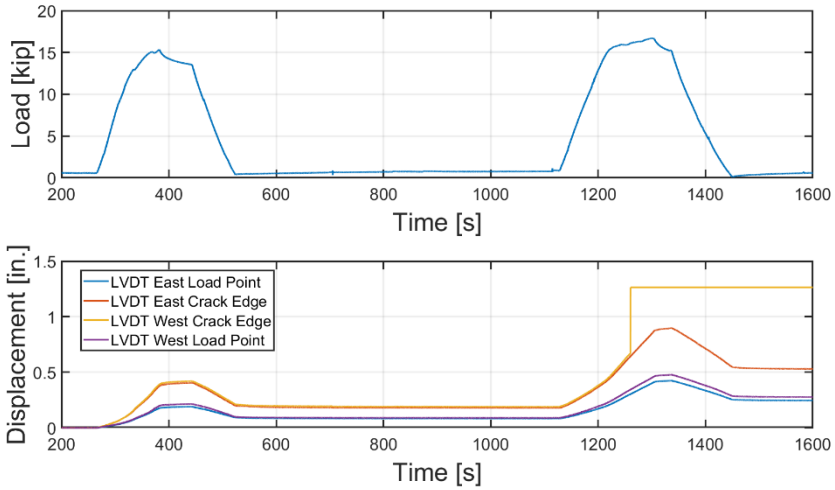

Figure 82. load and LVDT displacements against time in the parallel excavation bend testing

Figure 83 shows the moment-rotation response of S03 in parallel excavation bend tests. A maximum moment of roughly 200 kip-in. (23 kN-m) is achieved. Figure 84 shows the gap near the invert after the parallel excavation bend test. The excess resin that filled the gap between the steel host pipe segments has pulled away from one of the steel segments.

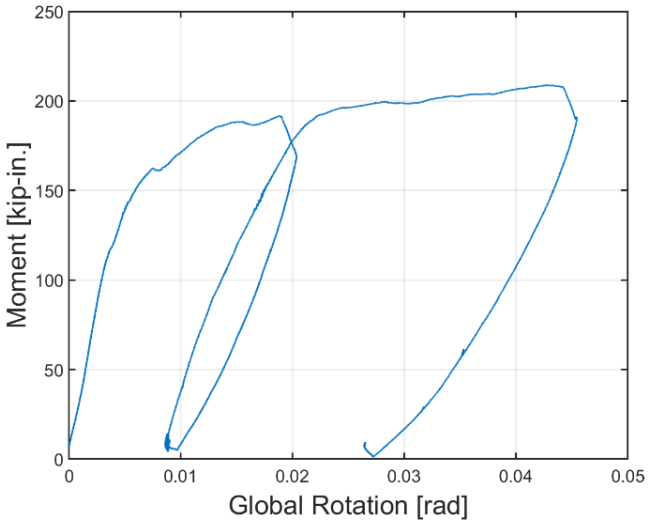

Figure 83. Moment vs. global rotation response under parallel excavation bend testing

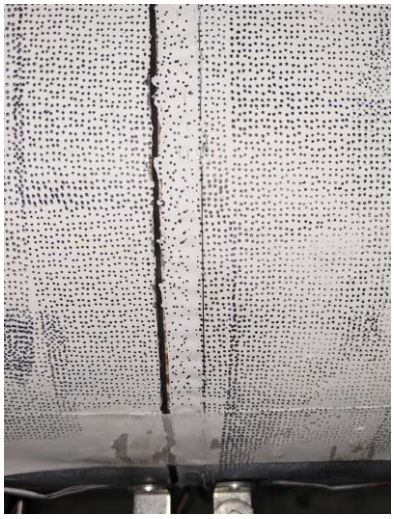

Figure 84. S03 gap after the parallel excavation bend test near the invert (north side of specimen)

5.4.2 S03 Axial Testing Results

Figure 85a and b show the axially applied displacement and actuator load, respectively, plotted against a pseudo-time index for most axial cycles of S03 (from 2nd set to 17th set). Figure 85c shows COD measures over the same set of cycles. The difference in displacements measured at different positions over the gap opening is partially attributed to the deformed shape of the structure imposed by the previous lateral deformation. These COD measures are zeroed from the first point of the first included set, and hence show the progressive increase in COD over the course of thermal cycles. While the north LVDT shows somewhat greater displacement over the first approximately 10 cycles, the displacement eventually becomes consistent during the middle cycle sets. There is an error in the measurement interpretation at time = 2.5 where an LVDT was manually adjusted, and thus a comparison past this point in the provided figures is not applicable.

The load vs. average COD for early axial cycles (cycles 1 and 2) is shown in Figure 86. The COD is calculated as the average of the crown, invert, and spring line measurements across the specimen gap opening. This is the case for subsequent data unless specifically noted otherwise. A load of roughly 20 kips (89 kN) is required for COD of 0.07 in. to 0.08 in. (1.8 mm – 2 mm).

Figure 87 shows the load, pressure, and axial strains measured on the host pipe against test time for cycles 8 to 14 (TH5). The last cycle shows the responses without internal pressure. The strain responses suggest considerable debonded length on the east side of the pipe, especially considering the relatively flat-lining behavior of the gauges 3 in. from the gap edge on the east pipe without internal pressure.

Figure 88 shows the load vs COD for an axial cycle with the nominal 65 psi (water, live) internal pressure and one cycle without pressure from the same test set (cycles 13 and 14). The magnitude of applied actuator displacement was identical for each cycle and the COD of both cycles was zeroed at cycle start. Internal pressure plays a notable role while performing axial cycles, as is indicated by the approximately 5 kips negative load offset at the beginning of the pressurized cycle relative to the no-pressure cycle. While both cycles follow approximately parallel paths to their maximum load (indicated constant specimen stiffness), the no-pressure cycle applied a load of about 33 kips (147 kN) achieved a COD of 0.17 in. (4.3 mm.) while a load of 30 kip (133 kN) was associated with a COD of 0.14 in. (3.5mm) for the cycle with internal pressure. This plot indicated the importance of tracking initial and progressive COD measurements during testing and the potential to adjust actuator displacement targets when test conditions are varied during a sequence or at the start of a new set of cycles.

Figure 89 shows the load and COD measurements against time for the 28th to 30th cycles, demonstrating relatively consistent measures of COD across all devices.

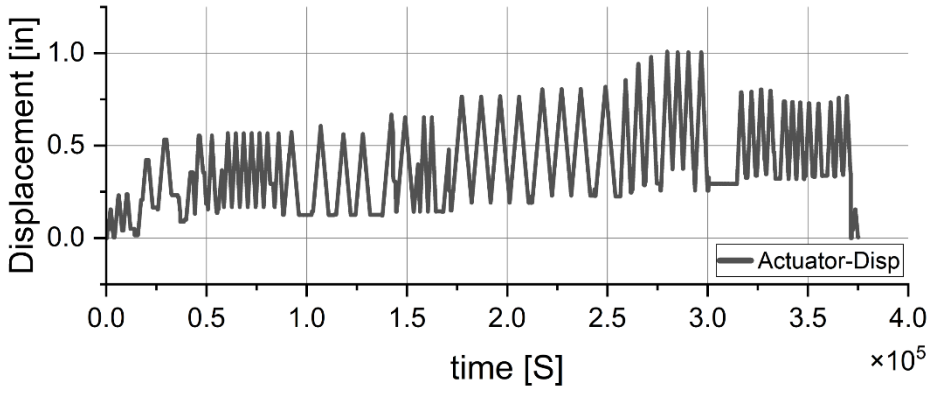

(a) actuator displacement

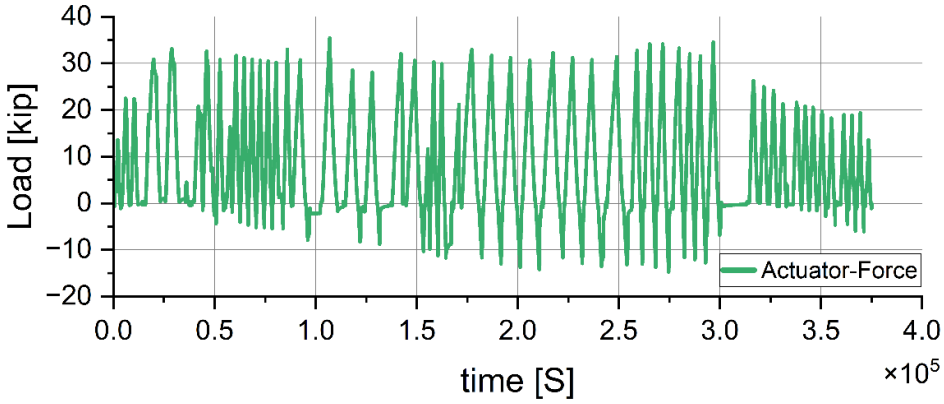

(b) actuator load

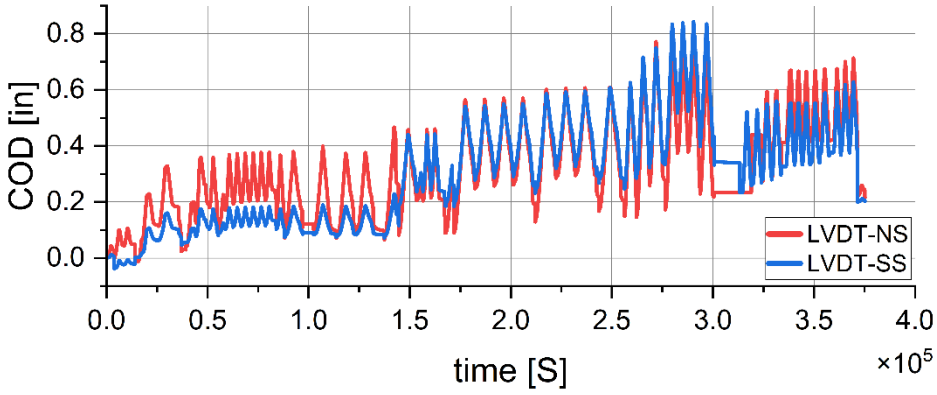

(c) gap opening displacement

Figure 85. Summary of axial cycles for S03: (a) actuator load, (b) applied displacement and (c) COD vs pseudo time

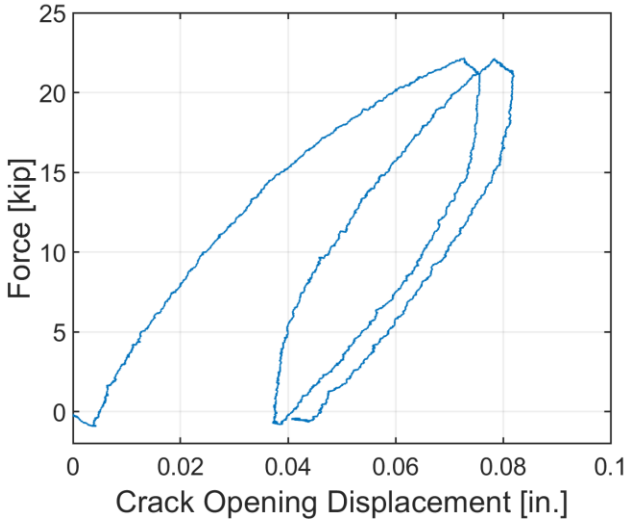

Figure 86. Early axial cycles, force vs. COD for S03

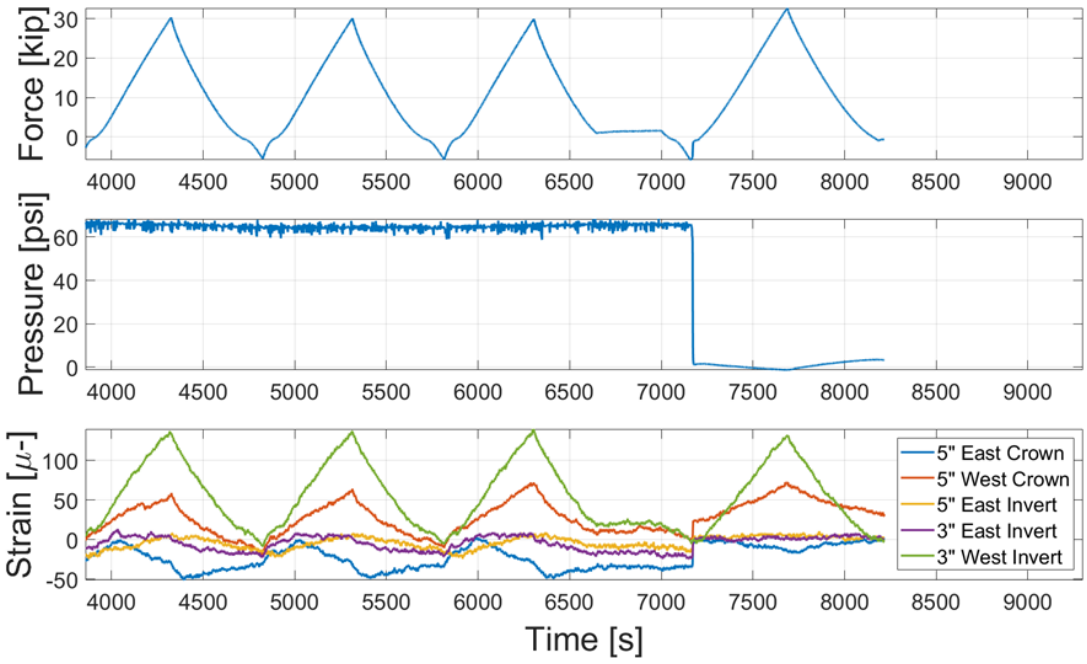

Figure 87. Axial force, pressure, and strain against time for axial cycles 8 to 14

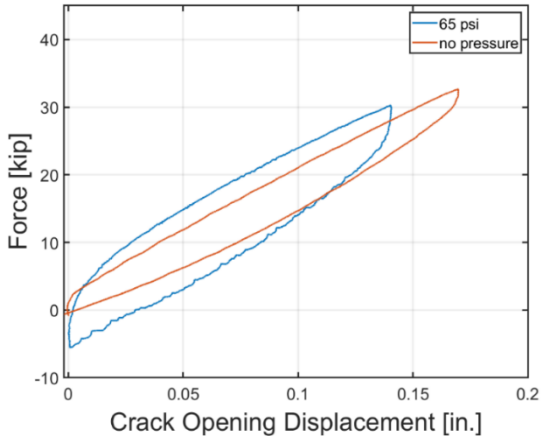

Figure 88. S03 axial cycles (13 & 14) with and without pressure

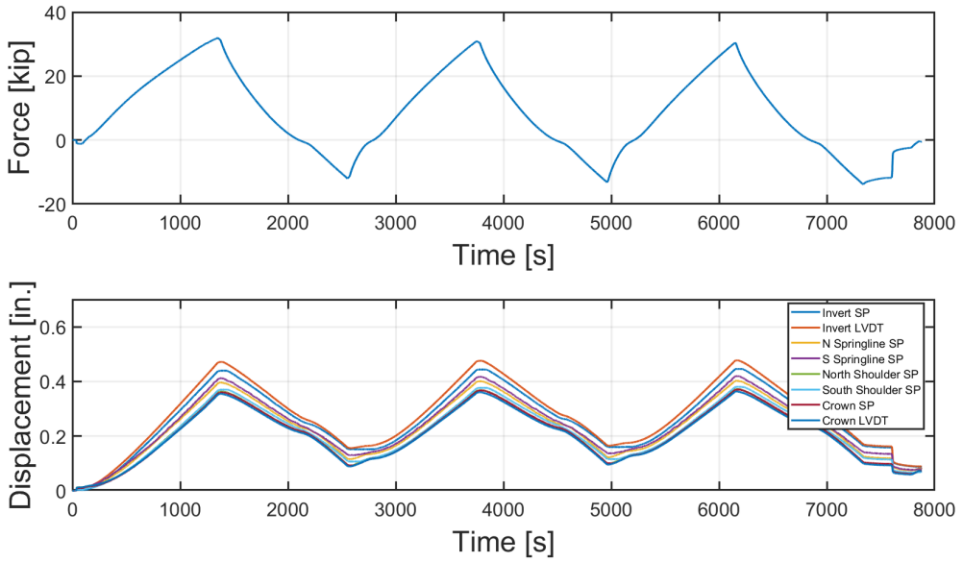

Figure 89. Load (a) and COD measures (b) against time for mid-procedure axial cycles

The load vs. the average COD from late axial cycles (cycle 35th to 38th) is provided in Figure 90. It can be observed that the maximum COD, which is 0.51 in. (13.3 mm), has progressively increased over the course of axial loading compared to earlier cycles, as previously shown in Figure 85.

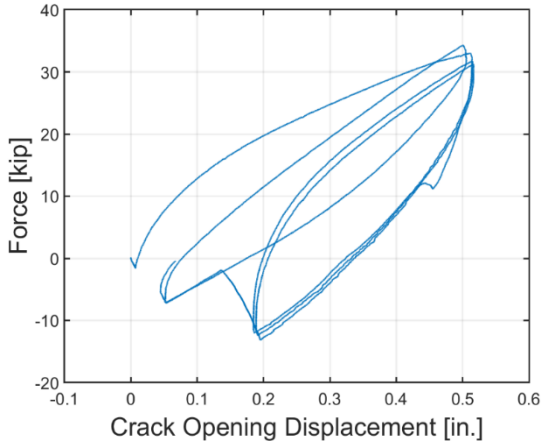

Figure 90. Later S03 axial cycles: force vs. COD

At the end of cycle 38, a minor leak was observed between the repair and steel host at the crown on the service connection side. Therefore, the pipe was repressurized with dead pressure to see how well it holds 65 psi (450 kPa) pressure. Figure 91 shows this change in internal pressure over time; a reduction of 66% of the initial pressure is seen over the course of 50 minutes.

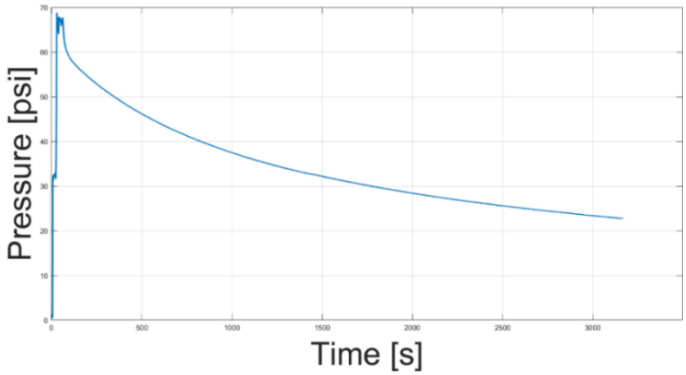

Figure 91. Pressure (Dead) vs. time after leak observed post 38th axial cycle

Testing was continued despite the marginal leak which was likely caused by debonding of the specimen back to the service connection located within 12 in. (300 mm) of the gap opening. The testing program was paused at this point to reassess the target CODs used throughout previous cycles and the progressive increase in COD that had occurred. It was determined that the applied cycles were significantly more aggressive than the analytical and numerical modeling indicated. This was largely due to the use of a safety factor of 2 applied to the target COD inputs, amongst many other conservative assumptions. These test results (the first time a reinstated service connect has been implemented in a specimen tested under

mechanically induced thermal loading) led to the refinement of the procedures for determining target COD. As such, the target COD was reduced to 0.26 in. (6.6 mm), which was determined to be representative of actual field conditions for all subsequent cycles.

The load versus the average COD from the 50th axial cycle is presented in Figure 92. Under a target COD of 0.26 in. (6.6 mm), the specimen continued to accommodate significant levels of deformation with no signs of degradation or reduction in capacity.

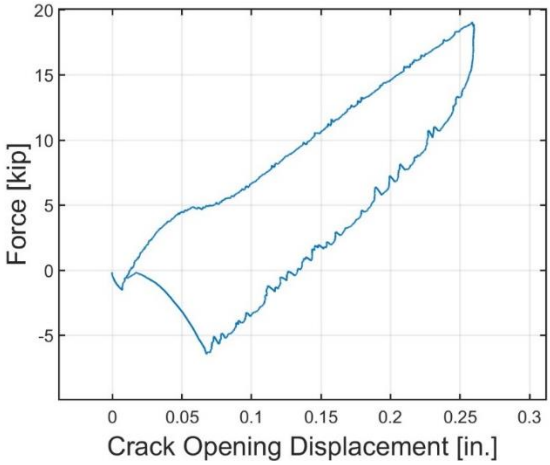

Figure 92. Force vs. COD for 50th axial cycle

5.4.3 S03 Pull to Failure Results

Figure 93 provides an overview of S03 pull to failure including axial load, displacements, and internal pressure vs. time over the entire test sequence. Figure 94 illustrates the load vs. average COD relationship, encompassing the pull-to-failure scenario for specimen S03. The COD remains approximately 0.6 in (15.24 mm) up to 30 kip (133 KN), displaying a linear trend. Beyond this point, as the load continues to increase, the COD progresses with a minimal increase in load. Notably, when the load is raised from 30 kip (133 KN) to 35 kip (156 KN), the gap opening expands to almost 3 in (76.2 mm). The material is subsequently pulled until reaching an approximate load of 38 kip (165 KN), accompanied by a COD of 4.5 in (114 mm).

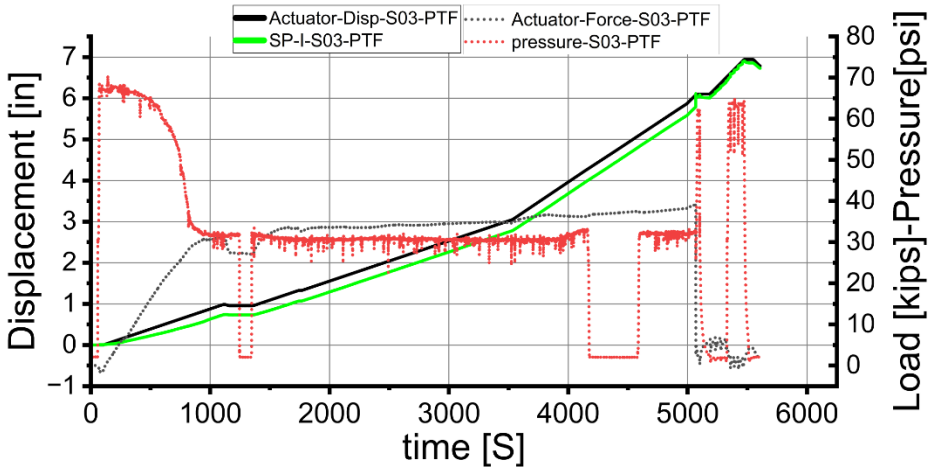

Figure 93. Crack Opening Displacement (COD)-Force vs. Pseudotime for large axial pull of S03 specimen.

Figure 95 illustrates the progression of Specimen S03 through different stages of the ultimate capacity axial tension test. In Figure 95 (a), the specimen is shown before the pull-to-failure test begins, with no debonding visible and the gap fully intact. Figure 95 (b) was taken after the specimen passes the linear region of the load-COD curve (Figure 94). Displacement is greater on the east side, where the service connection is located. Figure 95 (c) depicts the end of the pull-to-failure test, showing permanent displacement on both the west and east sides of the 0.5 in. gap. Finally, Figure 95 (d) displays the specimen after undergoing multiple post-test cycles, with a 15-inch displacement where the service connection hole on IRP is pulled out completely. These cycles occurred after the IRP had fully separated from the host pipe and were used to characterize the friction between pipe and IRP. Figure 96 shows an image of the inside of the specimen after the pull to failure test and post-test cycles, demonstrating that the east side of the specimen fully debonded from the host pipe.

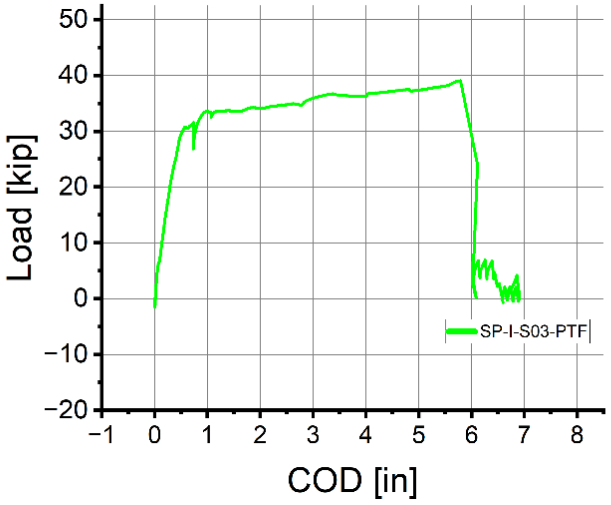

Figure 94. S03 force vs COD for pull to failure

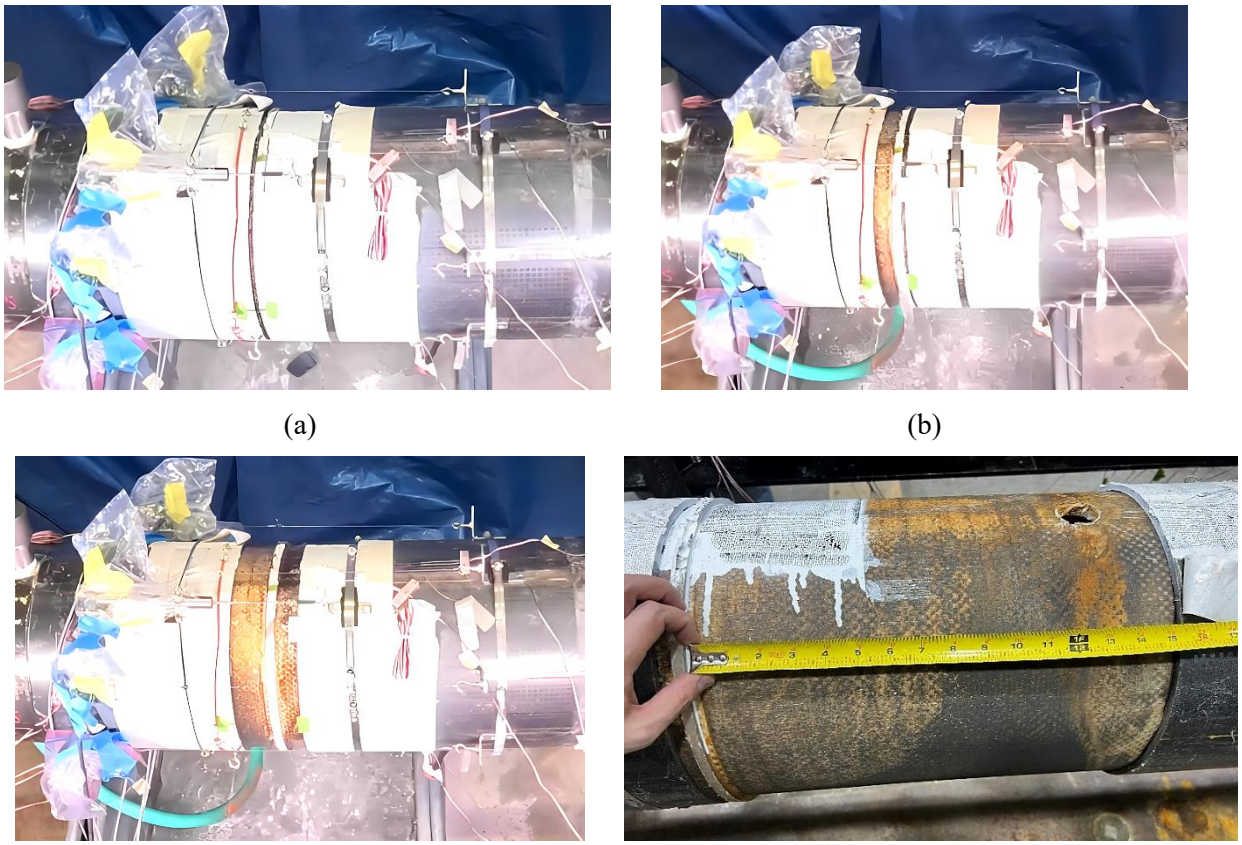

(a) (b)

(c) (d)

Figure 95. Specimen S03 (a) pre, (b) during, and (c) after detachment of the ultimate capacity axial tension test. (d) provides an image of the specimen after multiple post test sequences had been performed

Figure 96. Specimen S03, after all ultimate axial test cycles(including post pull friction cycles) had been applied to the specimen, showing East side fully debonded

5.5 S04 Results (Cornell)

An overview of the operations performed on S04 is provided in Table 18. This table lists the main loading procedures applied to the specimen. Information is summarized with respect to the general operation, number of tests and test cycles, test deformation, and configuration. The tests involved: 1) initial bending to verify operation of the equipment, 2) 500,000 cycles of repetitive traffic loads, 3) deformation imposed by parallel trench excavation, involving rotation about the center of the specimen of approximately 1.1° and 2.6°, 4) rotations of 0.25° and 0.40° applied over 15,000 and 70,000 cycles of traffic loading, respectively, 5) 76 cycles of temperature elongation/compression, and 6) two pulls to approximately 7 in. (178 mm) of maximum gap opening.

Table 18: Principal loading procedures for specimen S04

General Operation	Number of Tests or Cycles	Nominal Deformation Level	Test Configuration
Initial Flexure	4	~0.11° - 0.13° Rotation	25 in. - 40 in. - 25 in.
Traffic Loading Flexure/Bending Cycles	500,000	0.12° Rotation	25 in. - 40 in. - 25 in.
Parallel Excavation	2	1.1° Rotation, 2.6° Rotation	25 in. - 40 in. - 25 in.
Traffic Loading Bending Cycles	15,000	0.25° Rotation	25 in. - 40 in. - 25 in.

Traffic Loading Bending Cycles	85,000	0.40° Rotation	25 in. - 40 in. - 25 in.
Cycles of Thermally Induced Axial Displacement	76	0.03 in. – 0.55 in. COD	Axial Displacements
Axial Tension	2	6.5 in. – 7.0 in. Gap Opening	Pull to Failure

5.5.1 S04 Bending Results

The initial traffic load testing involved 500,000 cycles of load performed principally at cyclic frequencies of 1 Hz and 2 Hz, with a data sampling rate of 64 Hz. The targeted rotation was selected as 0.12° in consultation with Colorado University at Boulder (CUB). Applied global rotations ranged from about 0.11° to 0.13°. The actuator displacement associated with achieving these rotations was about 0.05 in. (1.3 mm).

A methodology for selecting the appropriate vertical displacements and global rotations from traffic loads for the rotational stiffness of the pipeline specimen was developed at Cornell University (e.g., O'Rourke & Netravali, 1996; Stewart et al., 2015). The methodology was adapted to more precise numerical modeling by CUB. During the tests on Specimen SNES04, global rotation, as well as vertical and horizontal displacements, were provided by CUB. One of the purposes of testing Specimen SNES04 was to compare the results with those of similar specimens at CUB. To meet this goal, it was necessary to test for the same deformations from repetitive traffic, parallel excavation, undermining, and thermal expansion/contraction at both Cornell and CUB. That way, one can compare the test results from two different institutions for the same deformations.

Traffic load testing at Cornell was performed daily. The cyclic loading was started and stopped on the same day to guard against unintended deformation of the specimen during nighttime or weekend loading. The tests were always run when personnel were able to observe and control the testing. A total of 34 groups or episodes of testing were performed to achieve a total slightly larger than 500,000 cycles. The number of cycles per each testing period varied from about 14,000 to 16,500.

Of fundamental importance for pipelines subjected to bending from rolling surface loads is the rotational stiffness at the lined gap or crack between two adjacent pipes. Figure 97 shows the moment vs global rotation of the specimen. The moment vs rotation traces a hysteresis loop, where the rotational stiffness can be defined as the slope of the line connecting the two apices of the hysteresis loop. The slope of that line is the stiffness $k_\theta = (\Delta M)/\Delta\theta$, as illustrated in the figure. The data in the figure were taken from Group 8 at about 150,000 cycles with $k_\theta = 420$ in.-kips (47,460 mm-kN) per degree, and from Group 34 at nearly 500,000 cycles with $k_\theta = 430$ in.-kips (48,590 mm-kN).

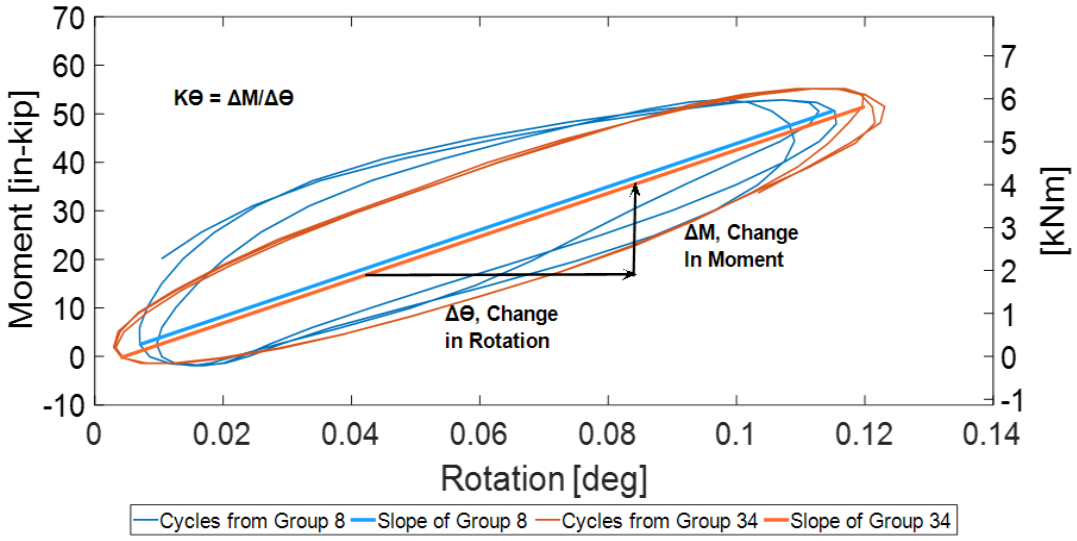

Figure 97. Typical moment vs rotation and definition of rotational stiffness, k_θ

Figure 98 shows the hysteresis loops associated with 1,000, 10,000, 100,000, and 500,000 cycles of traffic load. The maximum difference in the rotational stiffness is between k_θ = 491 in.-kips (53,480 mm-kN) per degree at 1,000 cycles and k_θ = 408 in.-kips (46,100 mm-kN) per degree at 500,000 cycles.

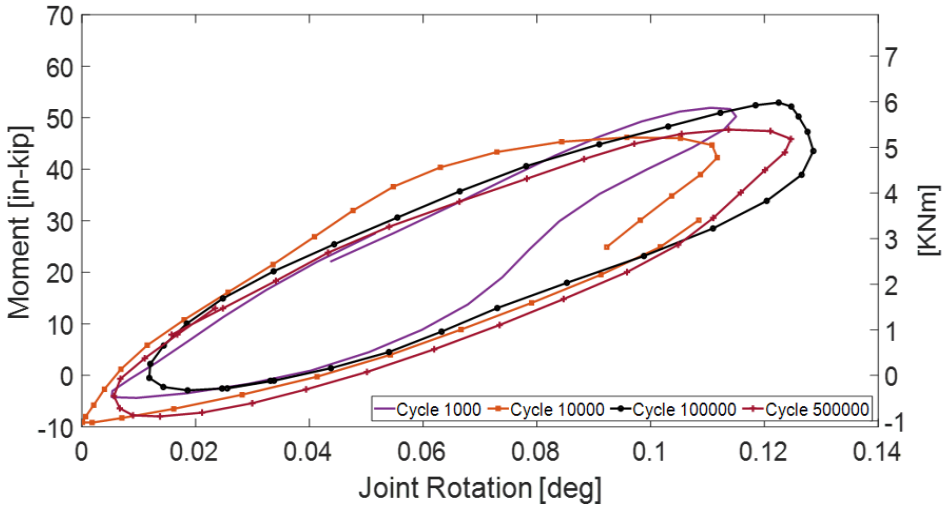

Figure 98. Moment vs rotation for various cycles of traffic load

Figure 99 presents a plot of the rotational stiffness relative to the number of cycles applied to the specimen. The rotational stiffness is, on average, about k_θ = 400 in.-kips (45,200 mm-kN) per degree. The stiffness

varied mostly ± 50 in.-kips (5650 mm-kN) per degree relative to the average. There is no clear trend in the stiffness. The variation in stiffness may be related to acquiring the data in 34 groups, which entailed resetting the loading system each time testing was performed. Minor differences in setting up 34 times would have affected the measurement of rotational stiffness.

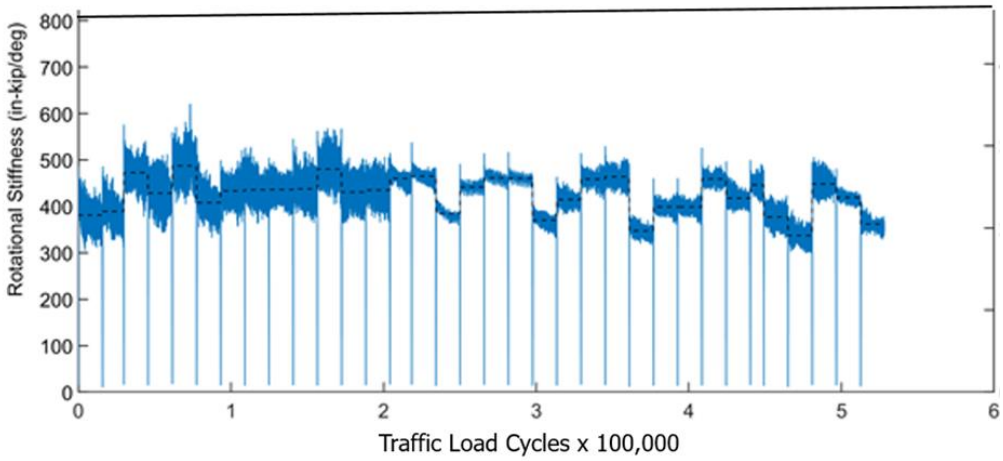

Figure 99. Rotational stiffness relative to number of cycles of traffic load

Stewart et al. (2015) evaluated the rotational stiffness at the mechanical joints of 12-in. (300-mm) diameter CI pipelines that were reinforced with a flexible polymer lining. They measured rotational stiffness k_θ = 200 in.-kips (22,600 mm-kN) per degree for traffic loading. This value is about half the rotational stiffness for similar conditions measured for this report.

After being subjected to 500,000 cycles of equivalent traffic load, no reduction in internal pressure nor leakage was observed in the test specimen.

To simulate parallel excavation effects, the loading saddles were loosened so that there was no rebound, nor restoration of the pipeline to its initial position. Parallel excavation effects were first modeled as a one-way loading to a rotation of approximately 1.10°. The actuator was then returned to its initial test position, and the specimen was loaded to a rotation of 2.6°. These rotations were provided by CUB. They correspond to a parallel excavation with maximum soil displacements of 2.5 in. and 5 in. (63.5 mm and 127 mm) and a safety factor of two.

The pipeline specimen was next subjected to 85,000 cycles of traffic load in two applications. First, the specimen was deformed by 15,000 cycles at an additional rotation of 0.25°. Next, the specimen was deformed by 70,000 cycles at an additional rotation of 0.40°. The rotations were selected in consultation with CUB. The rotations were imposed when the load saddles were tightened, thereby allowing the pipeline

to return to its initial position. This type of deformation simulates deflection in the field wherein the pipeline in soil returns to its original position after rolling traffic loads move across the pipe.

Pipeline deformation caused by adjacent, parallel excavation imposes relatively large rotations, which reduce the rotational stiffness of the joint. When cyclic traffic loads are applied after the effects of parallel excavation, the rotation increases for a given moment, thus reflecting the reduction of joint stiffness. As indicated previously, a rotation of about 0.12° was applied 500,000 times to model cyclic traffic loads. After adjacent, parallel excavation the rotations imposed were 0.25° and 0.40°, thus reflecting the reduced rotational stiffness.

Figure 100 presents the load path plotted in moment vs. rotation space for the effects of an adjacent, parallel excavation followed by additional cyclic traffic loads. The initial ~ 500,000 cycles of traffic load are shown in the figure. This combination of moment and rotation is characterized as pre-excavation cycles. About 12 representative load cycles are presented with an average k_θ = 360 in.-kip (40680 mm-kN) per degree. This rotational stiffness is at the lower end of the rotational stiffness measured for initial cyclic traffic loads (see Figure 99). The rotations of 1.1° and 2.6° generated by an adjacent excavation are also labeled in the figure and are presented as parallel excavation cycles. The maximum moment associated with 2.6° was approximately 190 in.-kips (21480 mm-kN). Two hysteresis loops related to 15,000 and 70,000 cycles of traffic load at 0.25° and 0.40°, respectively, are presented in the figure. This loading is characterized as post-excavation cycles. About 12 representative load cycles are presented for each hysteresis loop. The rotational stiffness of each of the two final cycles of traffic load is approximately k_θ = 150 in.-kip (16680 mm-kN) per degree. This rotational stiffness is about 40% of the rotational stiffness for the initial cyclic traffic load. The rotational stiffness was reduced by the relatively large deformation imposed by an adjacent excavation.

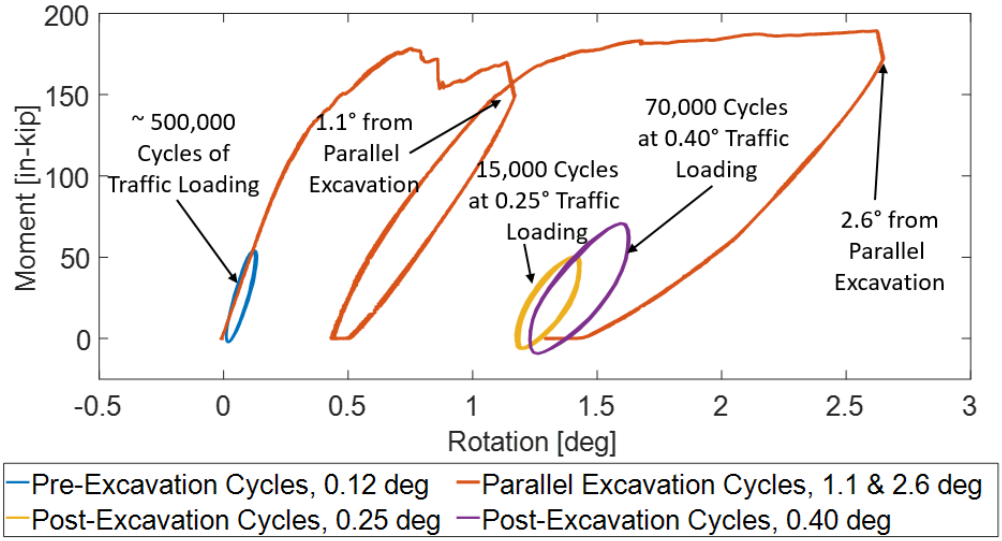

Figure 100. Moment vs. rotation of pre-excavation cycles for 0.18 degrees rotation, parallel excavation cycles for 1.1 and 2.6 degrees rotation and post excavation cycles for 0.25 an 0.40 degrees rotation

After being subjected to 500,000 cycles of equivalent traffic load, followed by deformation induced by parallel excavation and undermining, as well as an additional 85,000 cycles of traffic load, no reduction in internal pressure nor leakage was observed in the test specimen.

5.5.2 S04 Axial Testing Results

The deformation effects of thermal contraction and expansion were induced by cycles of tension alternating with compression that was applied to the pipeline specimen in the horizontal loading frame. Each cycle of tension and compression caused the center gap to open from its initial width at the start of the cycle and then return to a no-load condition. Models have been developed at Cornell University (e.g., O'Rourke, et al., 1996; Stewart et al., 2015) to obtain the gap opening displacement of a pipeline in soil subject to temperature change. These models have been adapted by CUB to more precise numerical simulations. The amount of gap opening was selected in consultation with CUB as approximately 0.03 in. (7.6 mm) to 0.55 in. (14.0 mm).

Figure 101 presents a typical load vs gap opening plot for Load Cycle 57 through 59. The bolts on the threaded rods were loosened so that the pipeline was unrestrained when water pressure of 65 psi (448 kN) was applied. The water pressure imposed a load on the end caps, resulting in a small displacement of the gap.

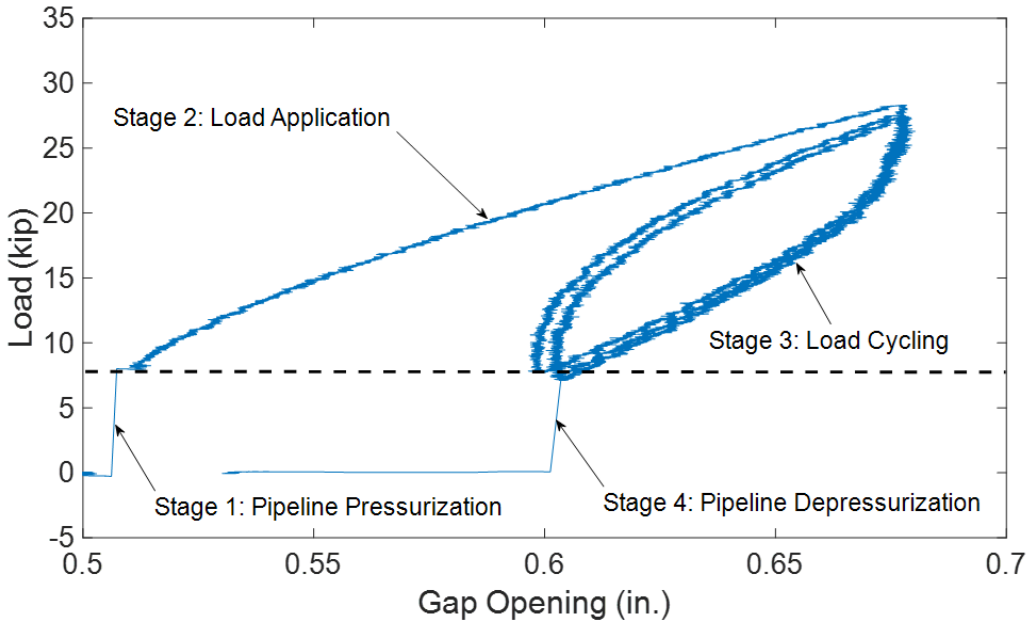

Figure 101. Typical axial load vs gap opening including pipeline pressurization and depressurization

As shown in the figure, Stage 1 involved a load increase from 0 to 8.4 kips (38 kN) from an initial gap width of about 0.506 in. (12.8 mm) to 0.512 in. (13.0 mm). The bolts then were tightened so that tension was applied to the specimen. During Stage 2 the load in tension increased from 8.4 kips (38 kN) to nearly 29.0 kips (129 kN) as the gap opened from about 0.51 in. (13.0 mm) to 0.68 in. (17.3 mm). Stage 3 involves hysteresis loops as the load was cycled from approximately 29.0 kips (129 kN) to 8.4 kips (38 kN). The axial stiffness is equivalent to the slope of the line connecting the two apices of the hysteresis loop, which was approximately 230 kip/in. (40.3 kN/mm). Stage 4 involved depressurizing the pipeline to zero load after loosening the nuts to allow relaxation and the recovery of displacement. The displacement was not fully recovered. At the end of the load cycles, the gap opening returned to 0.53 in. (13.5 mm), so there was about 0.02 in. (0.5 mm) of residual displacement. If no further load cycles were applied, there would be creep over time to a lower residual displacement with a smaller gap opening.

Pressurizing in fully restrained conditions could not be accomplished at Cornell because some small axial deformation would occur as the equipment and sample interfaces were seated during the test setup. These seating adjustments would result in axial load that could not be predicted. The initial conditions of lining stress, after pressuring an unrestrained pipeline, do not represent pressurizing under zero axial strain conditions, which would apply in the field. Nevertheless, it can be shown that the axial stress in the lining is either equal to or exceeds the stress related to pressurizing a fully restrained lined pipe specimen. Thus,

this procedure provides for a known state of stress that always equals or exceeds the stress in a restrained setup.

To focus on the thermal contraction/expansion of the lined pipeline, the initial conditions of pressurizing an unrestrained or fully restrained pipeline can be removed from the data. This removal is accomplished by reporting the load vs displacement data only for Stages 2 and 3. Such an adjustment is illustrated in Figure 101, where only data above the horizontal line, approximately equal to the initial pressurization load, are presented.

Figure 102 presents the load vs axial displacement data for the first 50 cycles of axial load, focusing on Stages 2 and 3. The figure shows the load vs displacement plots at various load cycles presented in the legend. Two practice applications of load (blue and orange) were performed, followed by the first simulated thermal displacement of 0.25 in. (6.4 mm), resulting in a gap opening from slightly larger than 0.5 in. (13 mm) to slightly larger than 0.75 in. (19 mm) [yellow]. The target displacement was provided by CUB. The hysteresis loops associated with various load cycles are color-coded, as many plots are on top of each other. For example, the hysteresis loops for Load Cycles 43 – 50 are plotted in purple on top of the hysteresis loops for many other load cycles, such as Load Cycles 20 – 42.

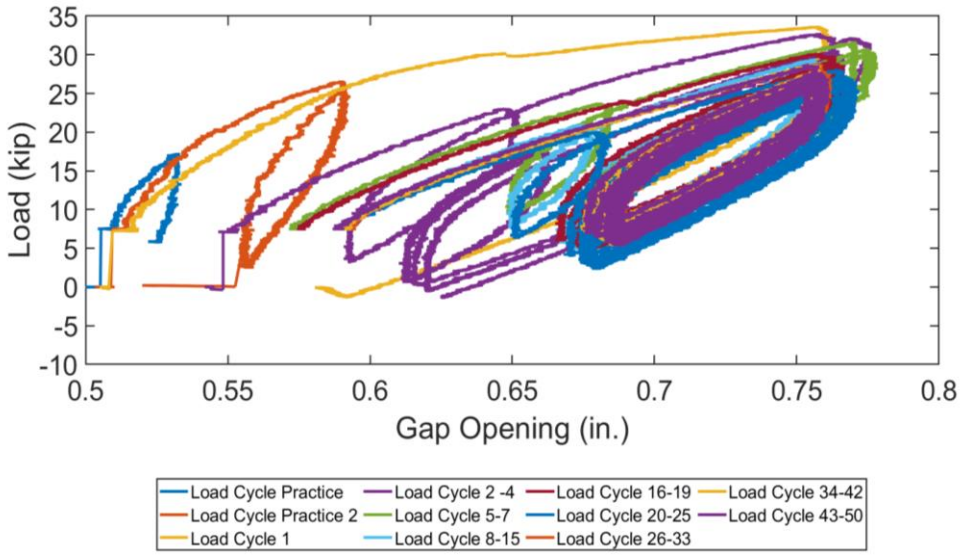

Figure 102. Load vs gap opening for various load cycles

The axial load stiffness for the practice loads was approximately 800 kip/in. (140 kN/mm). This stiffness was reduced by roughly 70% after the first full thermal load application. The load was cycled producing hysteresis loops, from which the stiffness was calculated mainly between 220 kip/in. (38.5

kN/mm) and 320 kip/in. (56 kN/mm). No clear trend in the stiffness was measured after the practice load cycles. The main reduction in stiffness was observed immediately after Load Cycle 1, the first full thermally driven displacement cycle.

There was a migration of gap opening from left to right in the figure. After Stage 3 load cycles the gap opening became larger. Figure 102 shows that the gap opening increased from slightly larger than 0.5 in. (13 mm) to about 0.68 in. (17 mm).

Figure 103 shows load vs gap opening for a final load cycle with internal pipe pressure of 65 psi (448 kPa) followed by a final load cycle at zero internal pressure. A displacement of 0.40 in. (10.1 mm) was applied to the gap opening of 0.56 in. (14.2 mm). As shown in the figure, leakage was observed at the crown when there was a gap opening of 0.96 in. (24.4 mm). When the total gap opening was increased to 1.03 in. (26.2 mm), the leakage increased to approximately 2 gpm (7.6 lpm). Water into the pipeline was then turned off to prevent local flooding. The pipeline specimen was unloaded and then reloaded under zero pressure, as shown in the figure. A maximum gap opening was measured as approximately 1.08 in. (27.4 mm) under zero internal pressure.

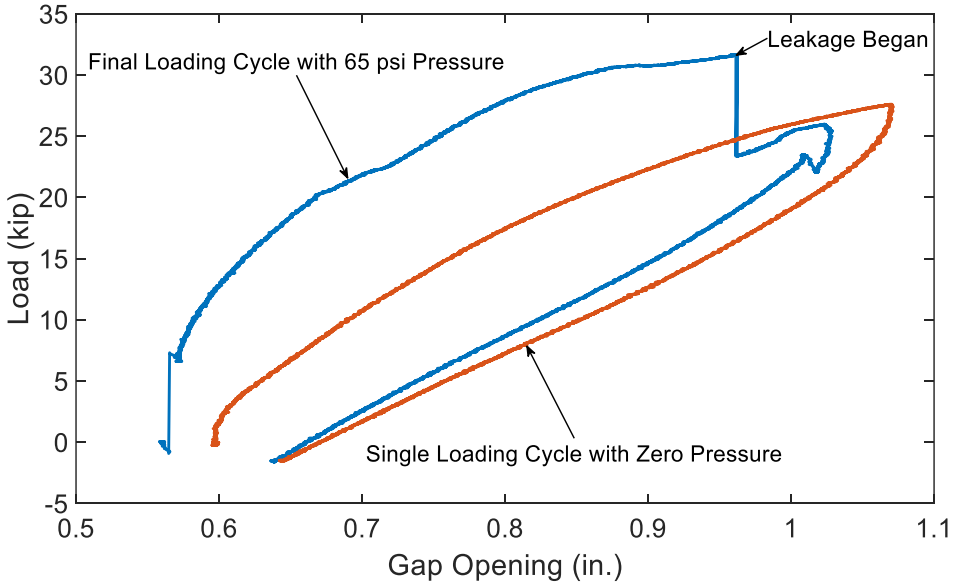

Figure 103. Final loading cycle with pressure and single loading cycle with zero pressure

Leakage at the crown of the pipeline at the central gap was in line with leakage at the service connection, approximately 14 in. (356 mm) north of the gap. It appears that the lining de-bonded from the host pipe northward until it intersected the service connection and caused tearing, thereby providing a path for water into the interface between the lining and the host pipe. The most direct path was for water to migrate from

the service connection along the crown until it emerged from the gap. After the pipeline was emptied of water, it was inspected with a camera. The inspection was inconclusive in locating the source of the leakage.

5.5.3 S04 Pull to Failure Results

Figure 104 shows the axial load vs displacement associated with the final applications of tensile force to failure. The load vs displacement plots were generated in two steps. The blue line shows the actuator load vs. gap opening for the first step. Only displacement equal to the actuator travel of 6 in. (152 mm) could be applied. The pull to failure of the dewatered specimen started at a gap opening of approximately 0.57 in. (14.5 mm). The actuator load increased to a maximum of about 40 kips (178 kN) at a displacement of approximately 6.3 in. (160 mm), which used up the actuator travel. The gradual increase in load is associated with de-bonding of the lining. The specimen then was unloaded from its maximum until zero load at about 3 in. (76 mm) of gap opening. The specimen relaxed further until about 2 in. (51 mm) of gap opening, at which point the second step was undertaken, for which the orange line indicates the load vs displacement plot. The maximum actuator force was about 41 kips (182 kN) at a maximum gap opening of nearly 7.0 in. (178 mm). The maximum actuator force corresponds to detachment of the lining from the host pipeline.

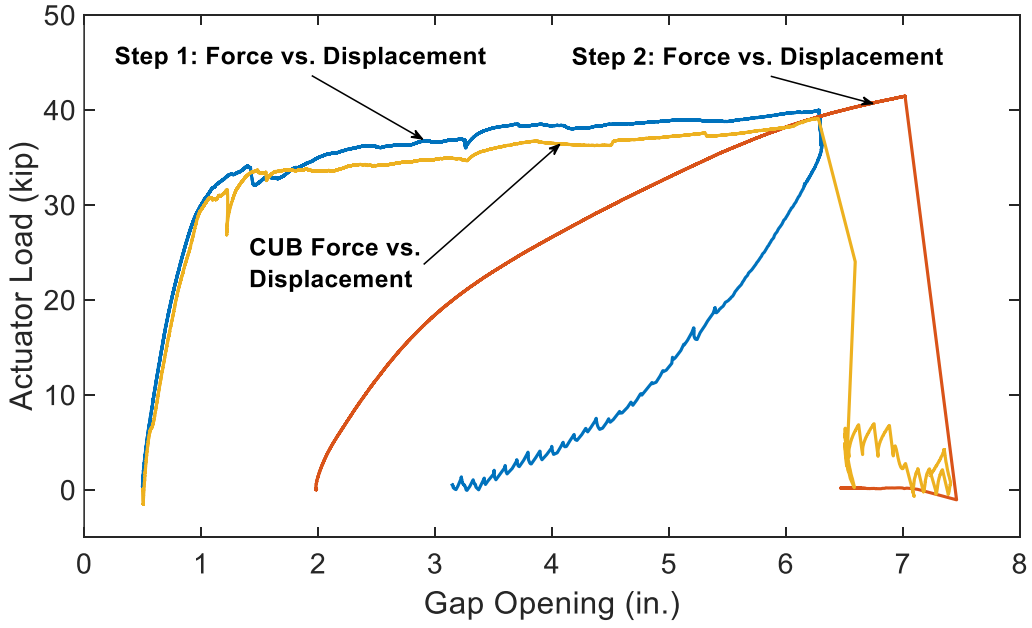

Figure 104. Actuator load vs gap opening

For comparison the actuator force vs displacement plot is shown in the figure for a similar pipeline specimen tested at CUB, showing good agreement between the Cornell and CUB test results. Further comparisons of specimens are discussed in the following section.

6 Discussion of Results

None of the specimens failed during the various bending operations. The stiffness of all four specimens does not change significantly during traffic loading cycles. It is apparent that the traffic loading cycles do progressively bend the pipe. The zero-load position of the actuator for the start position of a traffic loading set tended to become lower with subsequent traffic loading sets. In axial testing, COD is not always uniform about the circumference of the pipe; opening tends to be larger at or near the crown of pipe, which is logical considering the previous bending history.

6.1 Traffic Cycles

The following section summarizes key test results for each test performed. Table 19 summarizes the results for traffic cycles performed on each specimen, including the loading geometry, the cycle count, the target rotation, the average moment applied, and the approximate effective stiffness.

Table 19: Summary of traffic cycles for all specimens

Traffic Cycles					
ID (Gap/Crack Width)	Geometry	Approx. Cycle Count	Rotation (deg.)	Moment (kip-in)	Stiffness (kip-in/deg)
S01 (0.5 in.)	30” – 40” – 30”	1-10	~0.10°	54.5	545
		11 - 475,000	0.10°	52.5 – 57.5	525 - 575
	25” – 40” – 25”	475,001 – 475,010	~0.10°	43.5	435
		475,011 – 500,000	0.10°	43.5	435
		500,001 – 600,000	0.10°	40	400
C01 (0.5 in)	25” – 40” – 25”	1-10	~0.10°	38	380
		11 - 500,000	0.12°	42 – 46.2	350 - 385
		500,001 – 600,000	0.15°	40	265
S02 (6.0 in)	26.5” – 40” – 26.5”	1-10	~0.24°	46	192
		11 - 500,000	0.22°	38.5 – 46.2	175 - 210
		500,001 – 600,000	0.22°	35.2	160
S03 (0.5 in)	25” – 40” – 25”	1-10	~0.10°	52.5	525
		11 - 500,000	0.12°	63 – 73.2	525 - 610
		500,001 – 515,000	0.25°		
		515,001 – 600,000	0.40°		
S04 (0.5 in)	25” – 40” – 25”	1-10	0.11° - 0.13°	46.8	390
		11 - 500,000	0.12°	39 – 57	325 – 475
		500,001 – 515,000	0.25°	37.5	150
		515,001 – 600,000	0.40°	60	150

Although small differences can be observed between the specimens tested, it is important to note that there were no significant degradations in performances observed for the duration of traffic loading prior to adjacent excavation tests for each specimen tested. Traffic cycles performed after adjacent excavation tests resulted in minor reductions in rotational stiffness due to adjacent excavation tests exceeding linear behaviors of the specimens, discussed further in subsequent sections.

6.2 Adjacent Excavation

After approximately 500,000 traffic cycles were applied, several larger bending moments were applied to the specimen to simulate the effects of adjacent excavation events. Table 20 summarizes the results for parallel excavations performed on each specimen, including the loading geometry, the test ID, the target rotation, the average moment applied, and the approximate effective stiffness. Figure 105 and Figure 106 show a comparison of the moment vs. rotation for each specimen for both a small adjacent excavation event and a larger adjacent excavation event, respectively.

Table 20: Summary of adjacent (parallel) excavation loading

Adjacent Excavations					
ID (Gap/Crack Width)	Geometry	Test ID	Rotation (deg.)	Moment (kip-in.)	Stiffness (kip-in./deg)
S01 (0.5 in.)	25” – 40” – 25”	PE 1	0.18°	75	416
		PE 2	0.55°	190	345
C01 (0.5 in)	25” – 40” – 25”	PE 1	0.2°	80	400
		PE 2	0.7°	125	178
S02 (6.0 in)	26.5” – 40” – 26.5”	PE 1	1.4°	120	85
		PE 2	3.4°	150	44
S03 (0.5 in)	25” – 40” – 25”	PE 1	1°	175	175
		PE 2	1.8°	200	111
S04 (0.5 in)	25” – 40” – 25”	PE 1	1.2°	165	137
		PE 2	2.6°	190	79

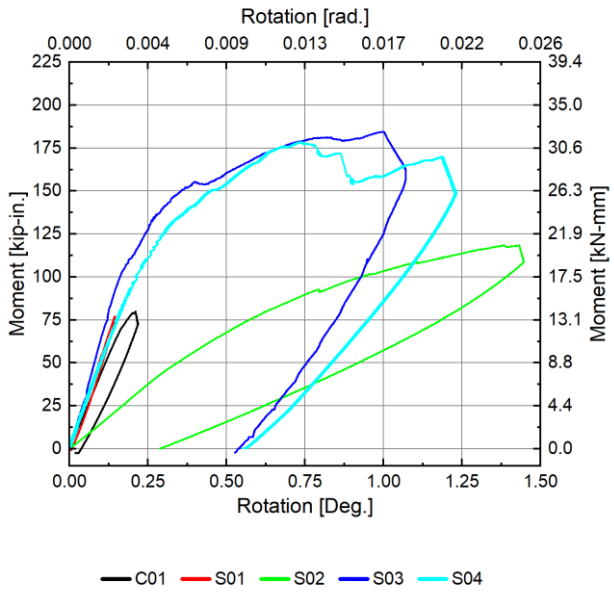

Figure 105. Moment vs. rotation results for small adjacent excavation events for each specimen

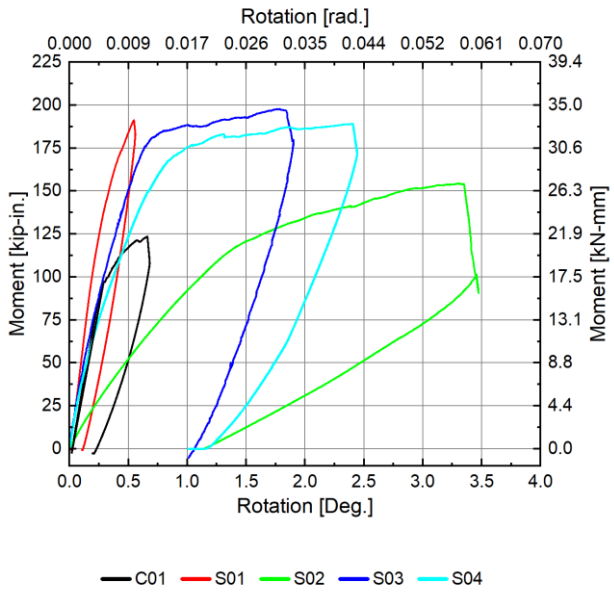

Figure 106. Moment vs. rotation results for large adjacent excavation events for each specimen

Specimens S01, S03, and S04 were all constructed using a steel host pipe and an initial gap width of 0.5 in (12.7 mm). As expected, each of these specimens had a similar response to the adjacent excavation events. During the smaller event, S01 was displaced to a maximum global rotation of about 0.18° (3.1 x 10-3 rad.) and loaded with a maximum moment of about 75 kip-in. (13.1 kN-mm). For the smaller excavation event S03 and S04 were displaced to a maximum rotation of about 1.0° (17.4 x 10-3 rad.) and 1.2° (20.9 x 10-3 rad.) and loaded with a maximum moment of about 175 kip-in. (30.6 kN-mm) and 165 kip-in. (28.9 kN-mm), respectively. Differences in maximum loading applied to S01 relative to the subsequent specimens are related to the progressive development process of the test methods herein. Despite differences in loading magnitude, when looking at the linear range of the moment vs. rotation plot, each specimen's response resulted in a similar effective rotational stiffness of about 375 kip-in./deg. During the larger adjacent excavation event, S01 was displaced to a maximum global rotation of about 0.55° (9.6 x 10-3 rad.) and loaded with a maximum moment of about 190 kip-in. (33.3 kN-mm). For the larger excavation event, S03 and S04 were displaced to maximum rotations of about 1.8° (31.4 x 10-3 rad.) and 2.4° (41.9 x 10-3 rad.) and loaded with a maximum moment of about 200 kip-in. (35 kN-mm) and 190 kip-in. (33.3 kN-mm), respectively. Each specimen was loaded with similar moments, but the maximum rotations differed, particularly for S01. The stiffer response of S01 is likely related to the magnitude to the previous traffic cycles, which were smaller than in subsequent specimens. The change in stiffness observed in all 0.5-in. steel specimens between 170 and 185 kip-in is due to a combination of factors, including inconsistency of the bond between the repair material and the host pipe, geometric differences across specimens, nonlinear material response, and impacts of preceding loading on the effective gap width. However, when looking at the linear range of the moment vs. rotation plot, each specimen maintains a similar rotational stiffness of about 400 kip-in/deg. Specimen C01 was also constructed with an initial gap width of 0.5 in (12.7 mm); however, a legacy cast iron host pipe was used for this specimen, as opposed to a surrogate steel host pipe. Similar to S01, this specimen was displaced to a smaller degree of rotation relative to the later tests for both the small and the large adjacent excavation event. C01 was displaced to a maximum rotation of about 0.2° (3.5 x 10-3 rad.) with a maximum applied moment of 80 kip-in. (14 kN-mm), and 0.7° (12.2 x 10-3 rad.) with a maximum applied moment of 125 kip-in. (21.9 kN-mm) for the small and large adjacent excavation events, respectively. The effective stiffness for C01 is consistent with the other 0.5 in. gap width specimens, indicating that the host pipe material does not have a significant influence on the effective rotational stiffness for a given specimen. Specimen S02 was constructed using a steel host pipe and an initial gap width of 6.0 in (152.4 mm), as opposed to the 0.5in. (12.7 mm) gap width of other specimens. As expected, results from traffic cycles indicated a rather significant reduction in effective rotational stiffness for this specimen, which required a reduced level of applied moment to

accommodate the adjacent excavation events. S02 was displaced to a maximum rotation of about 1.4° (24.5 x 10-3 rad.) with a maximum applied moment of 120 kip-in. (21 kN-mm), and 3.4° (59.3 x 10-3 rad.) with a maximum applied moment of 150 kip-in. (26.3 kN-mm) for the small and large adjacent excavation events, respectively. Unsurprisingly, S02 resulted in a much lower effective rotational stiffness for both tests performed. Considering the linear response of the material, an effective rotational stiffness of about 100 kip-in./deg. was observed for each test performed on S02. The change in stiffness beyond the linear range is also much less apparent relative to S03 and S04.

6.3 Thermal Expansion Cycles

After adjacent excavation tests and approximately 100,000 additional traffic cycles, specimens were then subjected to axial thermal expansion cycles. Table 21 summarizes the results for axial thermal expansion cycles performed on each specimen, including the cycle count, the target COD, the average maximum force applied, and the approximate effective specimen stiffness.

Table 21: Summary of thermal simulation axial test cycles

Thermal Expansion Cycles				
ID (Gap/Crack Width)	Approx. Cycle Count	Average Target COD [in. (mm)]	Approx. Max Force [kips (kN)]	Approx. Stiffness (kip-in)
S01 (0.5 in.)	1 - 3	0.08 (1.78)	20 (89)	250
	4 - 50	0.15 (3.81)	30 (133.5)	200
C01 (0.5 in)	1 - 3	0.03 (0.76)	12 (53.4)	400
	4 - 50	0.12 (3.05)	24 (106.8)	200
S02 (6.0 in)	1	0.12 (3.05)	20 (89)	166
	2 - 50	0.27 (6.86)	30 (133.5)	111
S03 (0.5 in)	0 - 3	0.08 (2.03)	20 (89)	250
	4 - 50	0.17 (4.32)	30 (133.5)	176
S04 (0.5 in)	0 - 3			176
	4 - 50	0.17 (4.32)	30 (133.5)	250

6.4 Axial Pull to Failure

After more than 50 thermal expansion cycles were applied, each specimen was then loaded to its ultimate force capacity. Table 22 summarizes the results for each specimen during ultimate capacity testing, including the COD at the instance of initial debonding, the maximum COD prior to loss in force capacity, the ultimate force capacity, and the approximate effective specimen stiffness. Figure 107 shows the ultimate force capacity relative to COD for each specimen. Figure 108 provides a magnified view of the initial loading relative to COD before initial debonding.

Table 22: Summary of ultimate axial capacity tests for all specimens

ID (Gap/Crack Width)	COD @ Initial Debonding [in. (mm)]	COD @ Ultimate Force Capacity [in. (mm)]	Ultimate Force Capacity [kip (kN)]	Tangent (Initial) Stiffness (kip/in)
S01 (0.5)	0.4 (10.1)	11.2 (284.5)	55 (244.6)	55
C01 (0.5)	0.1 (2.5)	5.0 (12)	45 (200.2)	45
S02 (6.0)	0.4 (10.1)	7.6 (193)	45 (200.2)	45
S03 (0.5)	0.5 (12.7)	5.6 (142.2)	40 (177.9)	40
S04 (0.5)	0.5 (12.7)	5.6 (142.2)	40 (177.9)	40

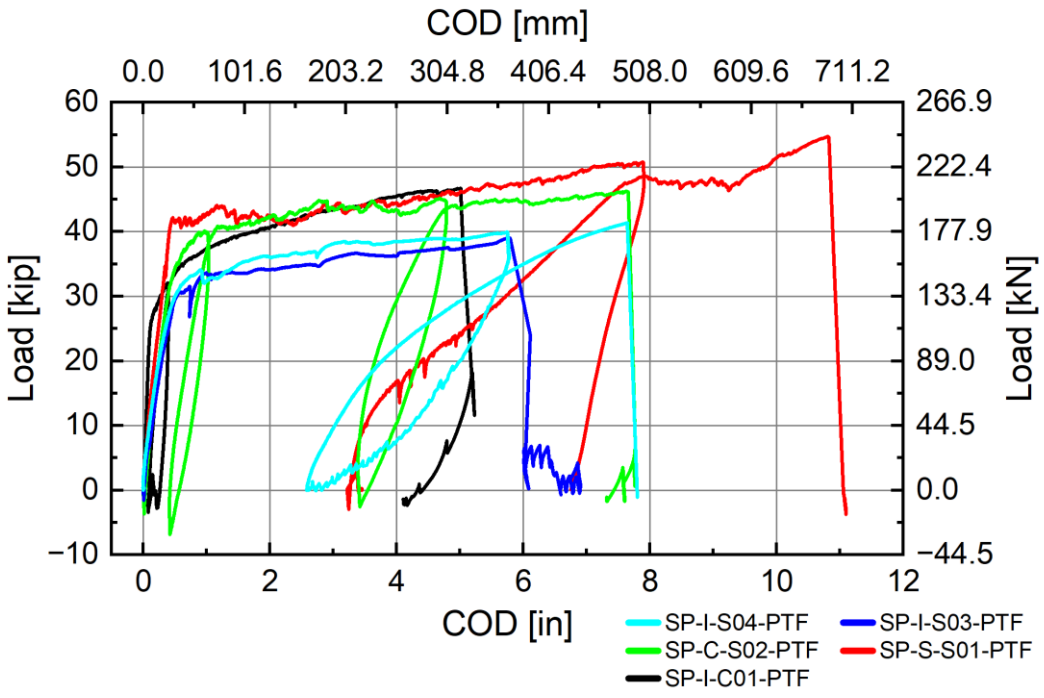

Figure 107. Pull to failure comparison for all specimens

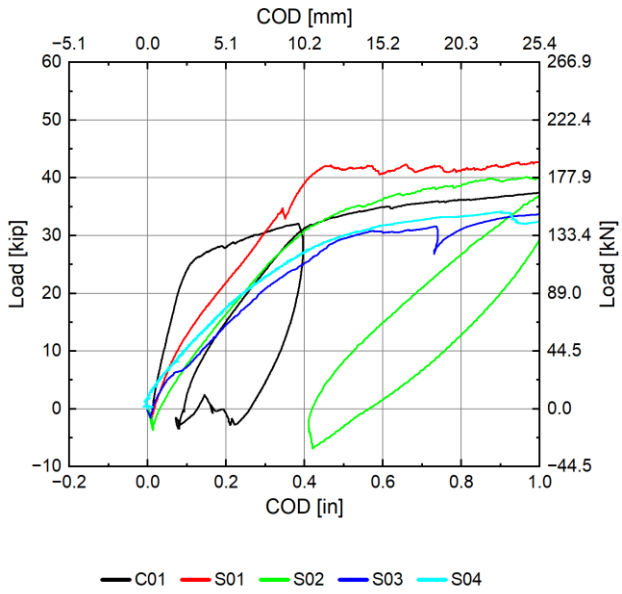

Figure 108. Pull to failure comparison for all specimens magnified at initial loading

Specimens S01, S03, and S04 were all fabricated using a steel host pipe and an initial gap width of 0.5 in (12.7 mm). S03 and S04 specimens had a similar response to the ultimate capacity test, while S01 achieved a larger ultimate force capacity and maximum COD. S01 was not loaded as rigorously during traffic cycles, adjacent excavation events, and axial thermal expansion cycles relative to S03 and S04. As a result, it is likely that the latter specimens may have experienced more debonding, reducing their ultimate capacities relative to S01. S01 and S04 were both loaded, unloaded, then loaded again. This was most likely due to running out of actuator stroke during the initial pull to failure. Once test setups were adjusted to allow further displacements, each of these specimens had much softer responses during initial loading due to a significant amount of debonding having already occurred, as expected.

Specimen C01 was also constructed with an initial gap width of 0.5 in (12.7 mm); however, a legacy cast iron host pipe was used for this specimen, as opposed to a surrogate steel host pipe. This specimen had a stiffer initial response relative to the other specimens with a 0.5 in. gap width. The rough surface of the legacy cast iron relative to the steel pipes may increase the frictional resistance between the repair material and the host pipe, adding to the overall stiffness of the specimen. However, C01 debonded sooner than the other specimens, indicating a weaker bond strength. The response of C02 after debonding occurs is noticeably stiffer relative to the stiffness of the other specimens after initial debonding occurs, further supporting that the frictional resistance of the CI is greater.

Specimen S02 was constructed using a steel host pipe and an initial gap width of 6.0 in (152.4 mm). Surprisingly, there were no clear differences in the performance of this specimen relative to others. Since ultimate failure testing was performed last, the testing up to this instance may have normalized the effective gap opening length, which would result in similar ultimate capacity responses regardless of the initial gap width.

6.5 Testing Variations

6.5.1 Rate Effects

During traffic cycles, loading was performed at both 1 Hz and 2 Hz for each specimen. Figure 109 shows a frequency sweep performed on S01, ranging from 0.3 Hz to 3 Hz. This study showed that the hysteresis loop "widens" as the frequency increases, indicating a less linear response for both loading and unloading curves. This trend was apparent for each specimen tested at both 1 Hz and 2 Hz (Figure 26, Figure 45, Figure 60). The observed trend suggests that the measurements maybe be influenced by a dynamic/inertial force effect. Higher frequencies would require the actuator to accelerate faster and slow down quicker, and those changes in rates within each cycle may cause differences in measured trends. Despite differences in loading rate, the figure shows that the target displacement and corresponding applied load remained consistent.

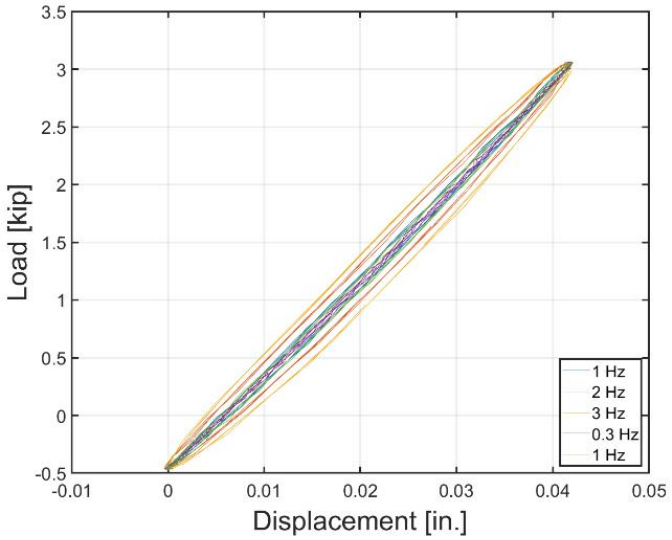

Figure 109. Load and displacement at various frequencies for S01

6.5.2 Pressure Effects

During traffic loading for each specimen, several different internal pressures were applied, ranging from 0 psi (0 kPa) to 65 psi (450 kPa). Each specimen shows some differences in behavior when comparing a pressurized state to a non-pressurized state. One notable difference is the shift in load and deformation indices. The maximum and minimum bending load during traffic cycles slightly increased when the pipe was not pressurized, best seen in Figure 24. With the pipe pressurized, one can expect the gap width of the specimen to slightly increase, increasing the overall length of the specimen. A longer specimen would be expected to experience more self-sag and thus require less applied load to reach the target deformation but more tensile load to return the specimen to an initial position against the self-sag. During thermal expansion cycles for each specimen, a similar trend was observed when comparing a pressurized state to a non-pressurized state. For the non-pressurized state, the maximum and minimum force for each cycle was slightly increased, but the gap width decreased, best seen in Figure 36. Internal pressure acts to push host pipe segments out, opening the gap, and when fixed in the frame, compression is recorded by the load cell, decreasing the recorded load during testing. It is also expected that internal pressure would stiffen the structure due to the constraining effect of the load applied perpendicular to the material. However, a substantial difference in stiffness is not readily apparent. This effect is likely minimal at low pressure like 65 psi (450 kPa).

6.5.3 Effect of Adjacent Excavation Deformations on Subsequent Response

Figure 109, Figure 110, and Figure 111 illustrate the moment vs. rotation curves for the specimens S01, C01, and S02 before and after the large parallel excavation, showing the effects on traffic loading cycles and small parallel excavation deformations. Three specimens (S01, C01, S02) exhibited a reduction in stiffness measured during traffic loading cycles following the parallel excavation deformations. For each figure, (a) shows the moment-rotation curves for traffic loading cycles before and after the large parallel excavation displacements were applied. Similarly, for each figure (b) the moment-rotation curves for moderate adjacent excavation cycles before and after the large adjacent excavation displacements are shown.

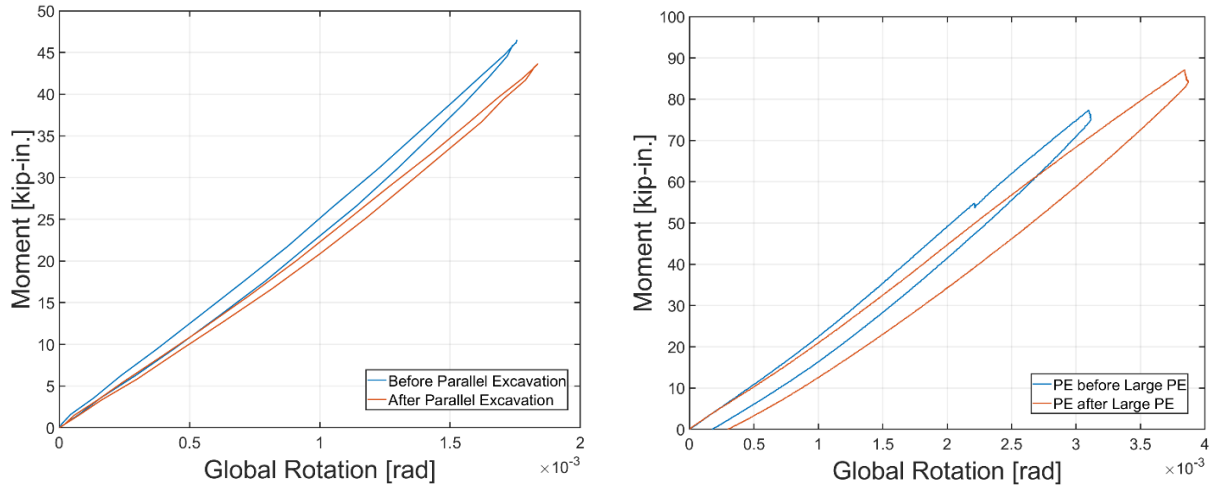

(a) (b)

Figure 110. S01 moment vs. rotation curves before and after the large adjacent excavation of (a) traffic loading cycles and (b) small parallel excavation deformations

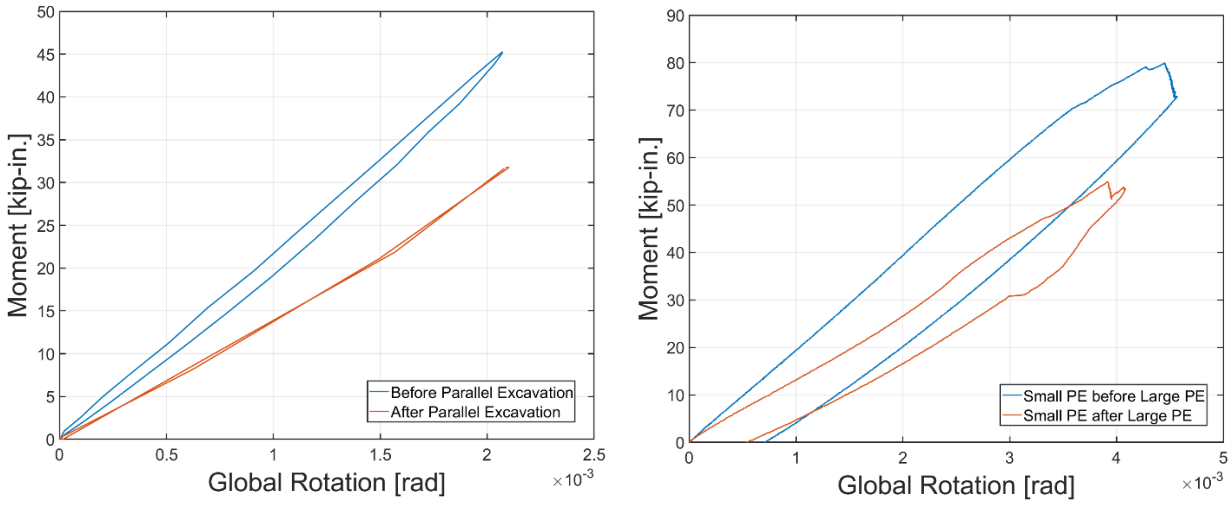

(a) (b)

Figure 111. C01 moment vs. rotation curves before and after the large adjacent excavation of (a) traffic loading cycles and (b) small parallel excavation deformations

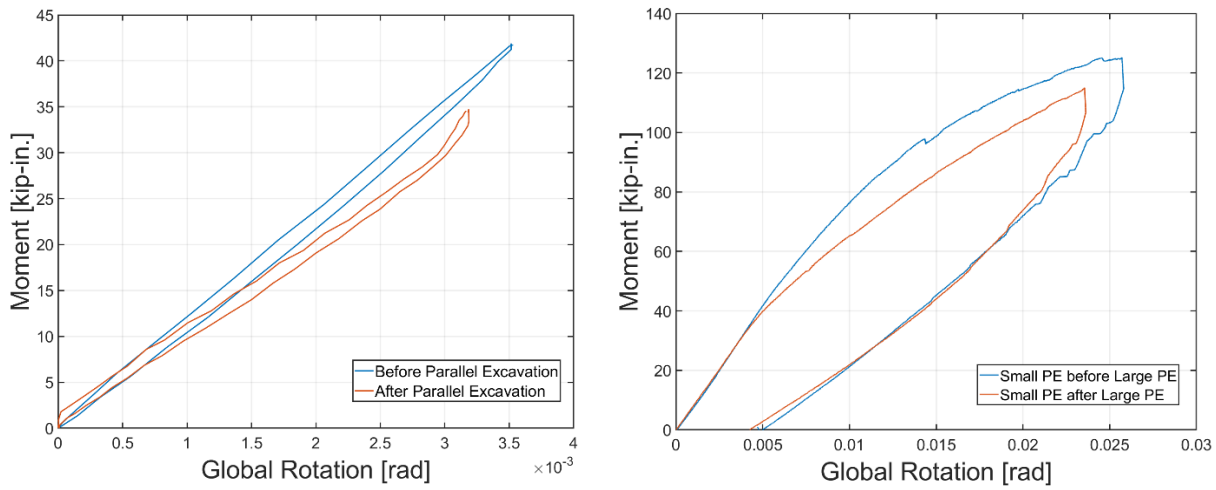

(a) (b)

Figure 112. S02 moment vs. rotation curves before and after the large adjacent excavation of (a) traffic loading cycles and (b) small parallel excavation deformations

Both the traffic cycles and the parallel excavations appear to show ca. 10% reduction in stiffness for S01. While the slope cannot be a reliable fit from the traffic cycles after the large parallel excavation deformation for C01, a substantial reduction in stiffness is apparent, ca. 30%. The response in the smaller parallel excavation deformations shows a stiffness reduction of about 35%. Interestingly, traffic loading cycles of S02 suggest 20% reduction in stiffness as a result of the parallel excavation, while the smaller parallel excavation suggests very little change in the initial response. This could be a result of the slightly different test conditions for these parallel excavations (restraining chains and cage adjustments in the "after" parallel excavation test).

The traffic loading moment-rotation behavior of S01 under the imposed parallel excavation deformation does show the least stiffness reduction of the three specimens (compare Figure 110(a) with Figure 111(a) and Figure 112(a)), suggesting less debonding (i.e., gap opening extension). It is also possible that changing the configuration of S01 straightened the specimen geometrically, thus reducing the apparent specimen stiffness (see section 5.3 for more details).

During the larger parallel excavation, there was an observed reduction in stiffness for each specimen over the duration of the test. C01 and S02 had reductions in stiffness that exceeded expected material behaviors, while S01 matched expectations. The stiffness reduction after a parallel excavation deformation has the potential to become an evaluation metric of the system. The level of stiffness reduction can be used to adjust the repair pipe stiffness in analytical and numerical assessments of the behavior under other conditions.

6.5.4 Change in S01 Bending Configuration

Before the final traffic cycles prior to the parallel excavation, the bending configuration of S01 was changed from 30 in. – 40 in. – 30 in. (762 mm – 1016 mm - 762 mm) to 25 in. – 40 in. – 25 in. (635 mm – 1016 mm – 635 mm). This change was implemented by lifting the specimen and adjusting the support saddles accordingly. The stiffness measured in traffic loading prior to this change was roughly 560 kip-in/deg [32000 kip-in./rad](63 kN-m/deg) (see Figure 27) and after 440 kip-in/deg [25000 kip-in./rad] (46 kN-m/deg) (Figure 31). One would expect only a small change (if any) as a result of the change in configuration; furthermore, basic analytical expressions suggest a slight (~10%) increase in stiffness would result as opposed to the substantial (~20%) decrease observed. The greater change in stiffness could be a result of lifting the specimen, which may have straightened the specimen from the deformed geometry acquired after the first 475,000 cycles of traffic loading. This change in geometry would lead to a reduced stiffness, as the specimen would experience less resistance while returning to its deformed state. Another possibility is that in lifting the specimen, damage, namely gap opening extension or further debonding, was induced, resulting in a less stiff structure. Regardless of the exact source, special care must be taken when maneuvering specimens during testing and between phases, and while not detrimental to the intended testing program, S01 results after this configuration change should be considered during interpretation.

6.5.5 Steel (S01) vs. Cast Iron (C01) Host Pipe

Although S01 and C01 had slight differences between both their physical geometry and loading geometry, these differences were minor, and the testing conditions were similar enough to compare results. Figure 113 shows the results for traffic cycles for each specimen. Figure 113a shows the moment vs. rotation data for the ~5,000th cycle, and Figure 113b shows the apparent stiffness of each specimen for all 500,000 traffic cycles performed prior to parallel excavation testing.

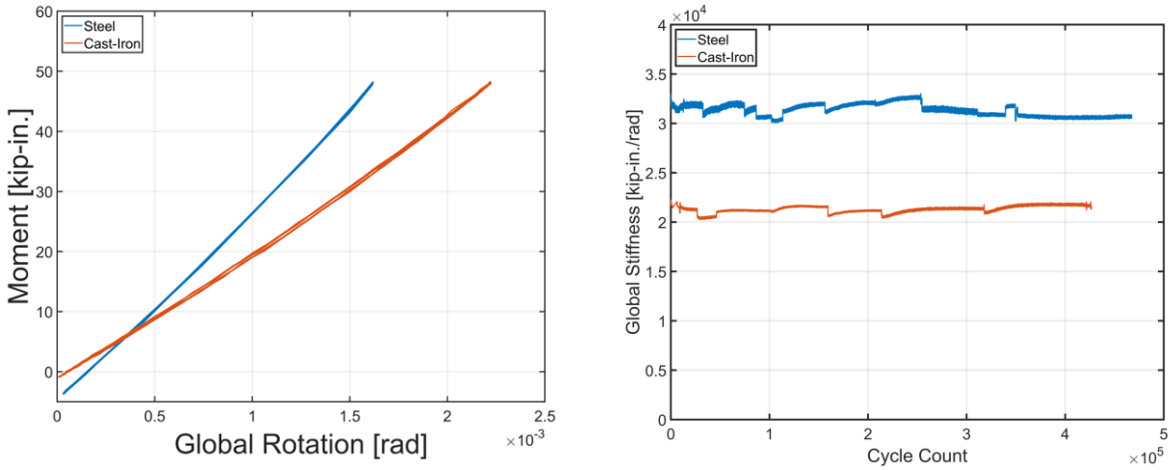

Figure 113. S01 vs. C01 in traffic loading, (a) moment-rotation behavior for the ~5000th traffic cycle (b) stiffness from the traffic loading cycles prior to parallel excavation deformation

This comparison shows the steel specimen has a stiffer response during traffic cycles. The stiffness is about 30% greater than the cast iron specimen. This difference in stiffness is not surprising because the interface formed between the liner and host pipe varies for each material. Since the cast iron pipe has a much less consistent surface, it is likely that the bond between the liner and the host pipe is also not consistent, resulting in a weaker bond and reducing the overall stiffness of the specimen. However, no significant reduction in stiffness was observed between the first and last traffic cycle for both the cast iron and the steel specimen, indicating that traffic loading did not significantly change or reduce the response of the specimen for each material.

The response to adjacent excavation deformation also shows S01 to be stiffer than C01 (even with the previously discussed stiffness reduction in S01 that resulted in changing the bending configuration). Figure 114 shows these responses: (a) features the response using the outer LVDTs to calculate the rotation (west alone for C01), and (b) features the response using the SPs attached to the saddles to calculate the rotation.

The parallel excavation responses also show a more prominent plateau behavior in C01's response relative to that of S01. Although C01 is subject to greater maximum rotations, the slope of the moment-rotation response for C01 reduces considerably more than S01 at the same degree of rotation (~0.005 rad). This behavior supports the theory that there is a "weaker" interface formed between the liner and cast iron, resulting in more debonding along the length of the pipe.

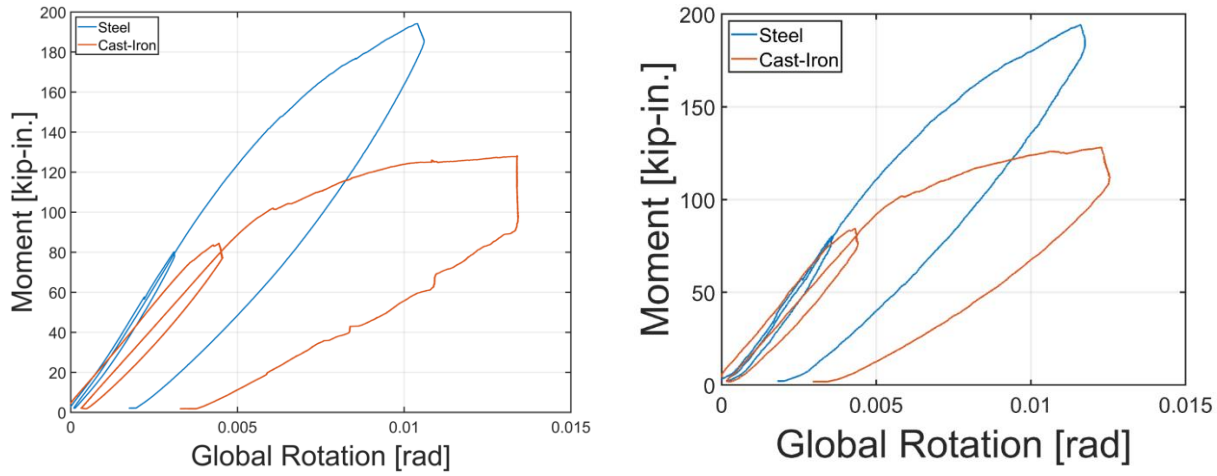

Figure 114. Moment vs. rotation behavior in parallel excavation deformation for S01 and C01, (a) rotation from LVDT measures (b) rotation from SP measures

The axial responses show a similar difference in stiffness. Figure 115 shows the responses for the small second axial cycle (a) and the response for several larger axial cycles in the middle of full ~50 axial cycles. In the early axial cycle shown, the response of C01 is considerably less stiff than that of S01, perhaps reflecting a larger gap opening imparted by the parallel excavation deformations. The larger displacement cycles show a ~30% difference in stiffness between each material, similar to what was seen over the vast majority of traffic loading.

Interestingly, the large axial pulls (pulls to failures) have some similarities. The first large axial pull of S01 (attempt to pull to failure) and the pull to failure of C01 show similar initial slopes, as shown in Figure 116. This, however, may be influenced by loading histories. Prior to the pull to failure, S01 was subjected to three roughly 0.4 in. (10.16 mm) displacement cycles (Figure 38), while C01 was only subjected to one (Figure 55). The subsequent stiffness reduction in S01 with these cycles is apparent in Figure 38.

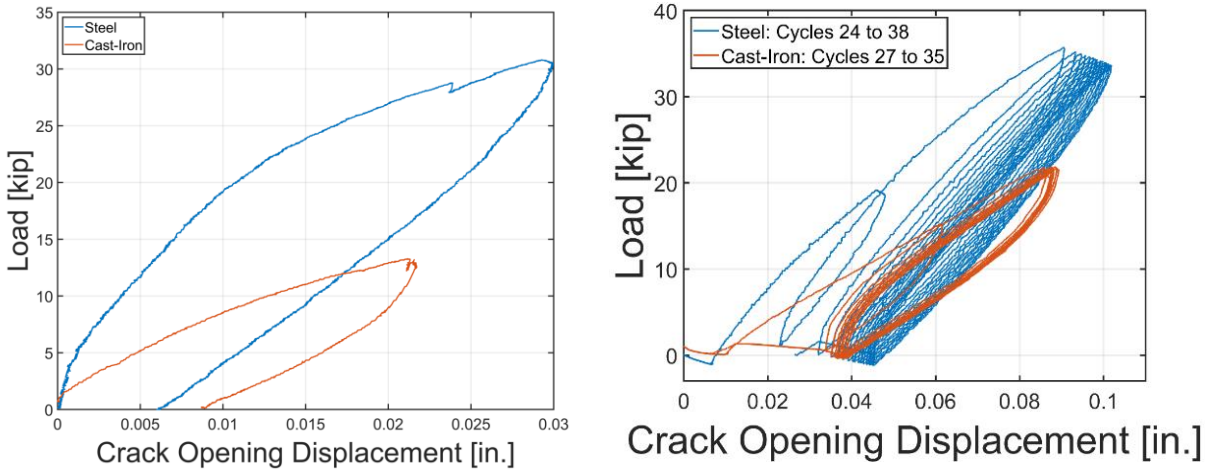

(a) (b)

Figure 115. Axial behavior comparison of S01 and C01, (a) second axial cycles, (b) typical axial cycles in testing

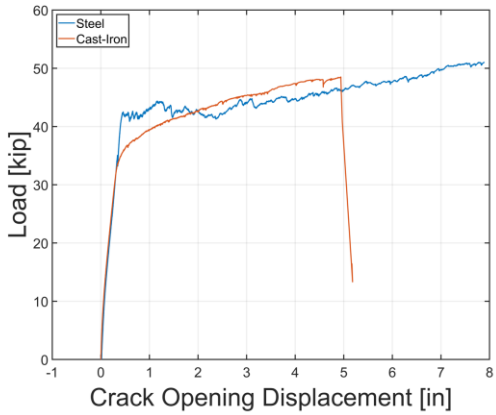

Figure 116. First large axial pull of S01 (attempt to pull to failure) and pull to failure of C01 (x-axis begins below 0 in. for ease in viewing slopes on large x-axis scale --- data is zeroed)

The post-failure response in tension of the two specimens is shown below in Figure 117. Figure 117 shows the forces required to pull the detached liner further without pressure (speeds ~ 0.2 in./min (5 mm/min) for S01 and ~0.3 in./min (7.6 mm/min) for C01). S01 shows a low and fairly constant force during this test, while the force increases until the load drops suddenly in C01 (and repeats). These post-failure responses also demonstrate differences in the interface, more specifically, the internal surface of the host pipe. The repair pipe in cast iron takes considerably more force (~25x) to move within the pipe post detachment. The considerable buildup of load and sudden drop in load and subsequent repetitions that characterize much of

the post-failure pullout in the cast-iron specimen and would seem to indicate slip–catch behavior, likely due to macroscale roughness of the internal surface of the host pipe. The steel specimen shows a lower and consistent load, likely indicative of kinetic friction and a smooth internal host pipe surface. This macroscale roughness of the cast iron specimen likely causes the interface to be weaker when intact (considering adhesion: gaps without adhesive, variation in adhesive/excess resin layer thickness, tortuous load transfer paths) resulting in a less stiff system and one that detaches at slightly lower load, but simultaneously creates more resistance to complete repair pipe pullout post detachment. The detachment in C01 may also be more localized than that in S01, which has a more consistent internal surface.

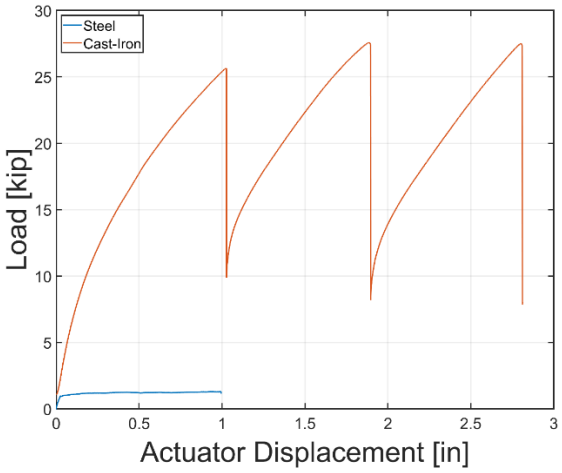

Figure 117. Post-failure tension without pressure for S01 and C01

Differences in the responses have been highlighted. However, S01 and C01 are in many ways similar. The specimens underwent similar loading histories and neither failed prematurely. Stiffnesses achieved moments, and loads are of the same orders of magnitude. Both specimens' mechanical responses to traffic loading remain relatively consistent (i.e., unaltered) over about 500,000 traffic cycles (Figure 113(b)). Furthermore, differences between specimens with cast iron host segments may be significant for the same repair system, given the potential variability in the internal surface and mechanical properties of legacy cast iron pipe.

6.6 Discussion of Methodology

One objective of this testing program is to validate the test methodology and procedures. As such, the following section discusses the methodologies adopted and provides some suggestions for future test programs.

For some conditions, an unpressurized pipe can be the worst-case scenario considering external load. Ring collapse or failure under external pressure is more likely without internal pressure, and similarly, an expectation that a compressive zone developed in longitudinal bending would be more likely to buckle and cause failure without internal pressure. However, testing with fluid inside the pipe and pressure allows leaks to be detected. For future testing for the natural gas industry, testing specimens at lower pressure and more reflective of actual operating pressures of legacy cast-iron gas distribution systems may be advisable. The level used in this work, typically ~65 psi (450 kPa), stemmed from two justifications: (1) in water distribution systems, this is representative of typical pressure in water distribution systems (typically between 50 – 100 psi) and (2) for the natural gas industry, typical maximum operating values (30 psi) multiplied by a safety factor of two. While fully justified for this program, future testing should consider end-use applications of the IRP and range internal pressure during testing appropriately. Moreover, pressurization and depressurization responses should be recorded in all future testing. Adjustments for pressure are straightforward and displacement in bending tests from pressure alone at the load points (i.e., those used to form the primary deformation metric – global rotation) is negligible.

In the context of all deformations applied to the specimens, the traffic loading cycles are relatively small. The stiffness of all specimens (at least with reference to further deformation) under roughly 500,000 traffic cycles remains mostly unchanged for the CIPP under test. These cycles do demonstrate fatigue performance, and a macroscale assessment does answer questions of scale and allows for the interface to be fatigue tested, which coupon-level testing would struggle to do. Nevertheless, there are some possible future considerations regarding these cycles.

1) The initial actuator position at the start of any one set of cycles is a variable to consider. One approach is to use the initial actuator position from the first traffic cycle set of a specimen for all subsequent cycle sets. This would essentially fix a reference position from which all deformation would be applied. This is justifiable because the soil around a legacy pipe is expected to be well compacted and any deformation would return the pipe to its initial position. Another approach would be to have a variable starting point for each set of traffic cycles, associated with where the actuator recorded zero force when coming into contact with the specimen. This second approach depends on a number of test parameters (e.g., position of supporting jacks, characteristics of the specimen harnesses) and, especially for lower modulus materials, may impose progressive deformation that is unrealistic relative to the anticipated state of a legacy host pipe in the ground. While the first approach was utilized, generally in this program, this observation is important for future testing programs.

2) Similar to the previous point, the start of cycling after the parallel excavation load is an important parameter. It is expected that after an excavation event, the ground remains to some extent deformed. After the post-excavation test, the reference point for additional traffic cycles should be adjusted to zero the actuator load at the start of cycling. This is likely to cause cycling to occur to a pipe specimen that is slightly more deformed. Again, this suggestion stems from justifications based on likely in-field conditions.
3) While the traffic cycles are conservatively derived, the authors wonder if there may be a potential method to streamline the testing. For example, could large levels of displacement be applied at a reduced number of cycles. As data is generated from testing specimens with IRPs of various materials and compared with coupon-level tests, this is a future question that will be considered.

The target displacements of axial cycles intuitively seem large. The use of an "effective gap/crack width" determined from initial pull data and a simple model is perhaps aggressive. Finite element modeling is ongoing to obtain a better understanding of gap opening with real interface conditions. If the flexibility/simplicity of the analytical approach is desired, the safety factor of two and/or the ΔT of 50°F (27.8°C) may need to be reevaluated. Finite element modeling may elucidate factors that should be applied, reducing target displacements. With potentially aggressive axial displacement targets (in addition to the timescales of the various events), performing bending operations first is logical. Tension was predominantly induced in the axial testing as it is considered worst case loading for the test configuration, but compression loading could be applied as well with less impact on the IRP and load predominantly being carried by the host pipe (for narrow gap widths).

7 Summary & Conclusions

This section summarizes the findings of the testing program performed on 12-in.- (300-mm) diameter specimens repaired with the AQUA-PIPE™. Five specimens were tested, including those with steel (4) and CI (1) host pipes. The specimens were prepared with a nominal 0.5-in. (12.7 mm) or 6-in. (150 mm) gap of exposed AQUA-PIPE™ IRP, with approximately 5 ft (1.52 m) of host pipe on either side of the gap. They were subjected to cyclic flexural and axial loading using specialized testing equipment at the Center for Infrastructure, Energy, and Space Testing (CIEST) at the University of Colorado Boulder and the Bovay Laboratory Complex at Cornell University.

The general methodology consisted of applying bending deformation to a pipe specimen, followed by axial loading, predominantly in tension. Bending involved 500,000 short duration (1 to 2 Hz) cycles representing cyclic deformation caused by overhead traffic. This fatigue testing was followed by larger bending deformations reflective of the system responses to adjacent excavation activity, which in turn were followed by roughly 100,000 additional "traffic" cycles. An ultimate parallel excavation deformation was then performed prior to the start of axial testing. In axial testing, 50 or more axial cycles were applied, representing the thermal deformation over 50 years associated with annual temperature changes ΔT of 40°F or 50°F (22.2°C or 27.8°C). Final axial tension tests were performed to assess the ultimate pullout capacity of the host pipe and AQUA-PIPE™ IRP. Most testing was performed at about 65 psi (450 kPa) of internal water pressure.

The levels of excavation movement assumed for the adjacent excavation cycles were associated 2.5 in. (63.5 mm) and 5 in. (127 mm) for the small and large events, respectively. The 5 in. (127 mm) level of soil displacement is expected to be used to set maximum parallel excavation deformation levels in future studies. The targeted rotational deformations depend on the stiffness of the repair pipe and the nature of the bonding between the repair and host pipe. If another IRP technology had a similar stiffness to AQUA-PIPE™, similar deformation levels would be anticipated. Initial stiffness tests of specimens and comparison with analytical and/or numerical models will inform the degree of bonding and, thus, deformation levels (for example see Klingaman et al., 2024).

The stiffness of the specimens in bending ranged from roughly 175 to 611 kip-in./deg (20 -70 kN-m/deg), using a global rotation calculated LVDTs positioned just outside the load points. The stiffness varied around ± 49 kip-in./deg (5.6 kN-mm/deg) relative to the average. There is no clear trend in the rotational stiffness. Maximum moments achieved in the lateral loading of all specimens ranged from 120 kip-in. to 200 kip-in. (13 kN-m to 23 kN-m). No specimen became structurally compromised or lost containment of water under the applied bending deformations.

The axial load stiffness associated with the initial practice loads was approximately 800 kip/in. (140 kN/mm). This stiffness was reduced by roughly 70% after the first full thermal load application to an axial load stiffness generally between 220 kip/in. (38.5 kN/mm) and 320 kip/in. (56 kN/mm). The principal reduction in stiffness was observed immediately after the first thermally-driven displacement cycle. For S02, the 6 in. (152.4 mm) gap width specimen, the targeted displacement and associated load were 0.3 in (7.62 mm) and roughly 30 kips (133 kN), respectively. All specimens experienced upwards of 50 such cycles.

The target displacements of axial cycles were derived from a simplified analytical model with the application of a 2.0 safety factor. Based on detailed finite element modeling performed in parallel to the testing program, it was determined that these applied thermal movements used in this testing were indictive of loads greater than would be generated under field conditions. It was further found that a safety factor of 1 to 1.25 resulted in pipeline and IRP deformations that were conservative and better matched to in-situ conditions. Future testing programs should institute target displacements that would actually occur (e.g., using a FS between 1 and 1.25 for axial deformation when implementing the Dixon et al. (2023a) target deformation methods).

Leakage was observed at the crown of the specimen following thermal displacement Cycle 38 and 76 for S03 and S04, respectively. It appears that the lining de-bonded from the host pipe toward the service connection. Once de-bonding reached the service connection, a path for water into the interface between the lining and host pipe opened, resulting in minor leakage at the center gap.

As prescribed by the test program, the ultimate capacity in axial tension of all specimens was achieved by IRP detachment from the host pipe. This occurred at loads around 50 kips (220 kN) with CODs at failure from roughly 5 in. to 12 in. (127 mm to 304.8 mm). A steel specimen (S01) was found to be stiffer than a cast-iron specimen (C01) of the same gap width, suggesting differences in host pipe geometry and/or interface characteristics between the liner and the host pipes. Qualitatively, their behavior is quite similar, and, given the variability of CI pipe in the field, differences in behavior across specimens are expected. The 6 in. (152.4 mm) gap width steel specimen (S02) has considerably lower stiffness than the 0.5 in. (12.7 mm) gap width steel specimen (S01) in both bending and axial tension, as expected.

The AQUA-PIPE™ repair system performed well under all applied external loads representative of 50 years of service. No cracks or significant structural damage to the IRP were observed during service life testing, and no leakage occurred until the final stages of cyclic testing for thermally induced axial displacements. The product was able to debond locally from the host pipe to accommodate strain concentrations while achieving containment and continuity. While this testing program and the applied cycles were limited to a 50-year service life due to project time constraints, the performance observed

suggests that longer durations of testing could demonstrate the ability of the system to accommodate a service life exceeding 50 years. While the reported performance was expected based on previous studies of this IRP system, this research demonstrates that the proposed service life testing procedures can be accommodated by existing trenchless technology and supports further applications of the proposed methods.

References

Ahmadi, H., Manalo, A., Dixon, P.G., Salah, A., Karunasena, W., Tien, C.M.T., … Wham, B.P. (2024). "Temperature change-induced linear and nonlinear axial responses of internal replacement pipe (IRP) systems for pipeline rehabilitation incorporating the effects of soil friction". *Structures*, *62*(March), 106247. doi.org/10.1016/j.istruc.2024.106247

Allouche, E.N., Alam, S., Simicevic, J., Sterling, R., Condit, W., Matthews, J., & Selvakumar, A. (2014). "A pilot study for retrospective evaluation of cured-in-place pipe (CIPP) rehabilitation of municipal gravity sewers". *Tunnelling and Underground Space Technology*, *39*, 82–93. doi.org/10.1016/j.tust.2012.02.002

ASME. (2018). *Article 403 Nonmetallic Internal Line for Pipe: Sprayed Form for Buried Pipe*. *ASME PCC-2-2018 Repair of Pressure Equipment and Piping*. New York: ASME.

ASTM. (2016a). "F3182 - 16 Standard practice for the application of spray-applied polymeric liners inside pipelines for potable water". *ASTM International*. West Conshohocken, PA. doi.org/10.1520/F3182

ASTM. (2016b, August 1). "F1216: Practice for Rehabilitation of Existing Pipelines and Conduits by the Inversion and Curing of a Resin-Impregnated Tube". West Conshohocken, PA: ASTM International. doi.org/10.1520/F1216-16

ASTM. (2017, February). "F1743: Practice for Rehabilitation of Existing Pipelines and Conduits by Pulled-in-Place Installation of Cured-in-Place Thermosetting Resin Pipe (CIPP)". West Conshohocken, PA: ASTM International. doi.org/10.1520/F1743-17

ASTM. (2018). "D5813 - 04 Standard Specification for Cured-In-Place Thermosetting Resin Sewer Piping Systems". doi.org/10.1520/D5813-04R18

ASTM. (2019). "F2207-06: Standard Specification for Cured-in-Place Pipe Lining System for Rehabilitation of Metallic Gas Pipe". West Conshohocken, PA. doi.org/10.1520/F2207-06R19

AWWA. (2019). "Committee Report: Structural Classifications of Pressure Pipe Linings". American Water Works Association (AWWA).

Bussières, J. (2021). *Characterization of water main CIPP liner*. RAP-21200-B-1, Centre de développement des composites du Québec (CDCQ), Saint-Jérôme, QC. Retrieved from www.cdcq.qc.ca

Dixon, P.G., Salah, A., Ahmadi, H., Ulrich, M.E., Hubler, M.H., Dashti, S., … Wham, B.P. (2023a). "An Analytical Approach for Thermally Induced Axial Deformation in Rehabilitated Pipelines". *Proceedings: Pipelines 2023* (pp. 260–269). Reston, VA: American Society of Civil Engineers. doi.org/10.1061/9780784485026.028

Dixon, P.G., Tafsirojjaman, T., Klingaman, J., Hubler, M.H., Dashti, S., O'Rourke, T.D., … Wham, B.P. (2023b). "State-of-the-Art Review of Performance Objectives for Legacy Gas Pipelines with Pipe-in-Pipe Rehabilitation Technologies". *Journal of Pipeline Systems Engineering and Practice*, *14*(2), 1–13. doi.org/10.1061/JPSEA2.PSENG-1371

Fu, G., Shannon, B., Rathnayaka, S., Deo, R., & Kodikara, J. (2020). *State of The Art Literature Review on CIPP liners*. *CRC Project: Smart Linings for Pipe and Infrastructure*.

Jeon, S.-S., O'Rourke, T.D., Neravali, A.N., O'Rourke, T.D., & Neravali, A.N. (2004). "Repetitive Loading Effects on Cast Iron Pipelines with Cast-in-Place Pipe Lining Systems". *Journal of Transportation Engineering*, *130*(6), 692–705. doi.org/10.1061/(ASCE)0733-947X(2004)130:6(692)

Klingaman, J., Dixon, P.G., Wham, B.P., Dashti, S., & Hubler, M.H. (2022). "Traffic Loading Effects on Rehabilitated Cast Iron Distribution Pipelines". *Proceedings: Pipelines 2022* (pp. 313–323). Reston, VA: American Society of Civil Engineers. doi.org/10.1061/9780784484296.037

Klingaman, J., Wham, B.P., Dixon, P.G., & Dashti, S. (2025). "External loading-induced deformations of deteriorated pipelines rehabilitated with internal replacement technologies". *Tunnelling and Underground Space Technology*, *157*(March), 106272. doi.org/10.1016/j.tust.2024.106272

Lu, H., Behbahani, S., Azimi, M., Matthews, J.C., Han, S., & Iseley, T. (2020). "Trenchless Construction

Technologies for Oil and Gas Pipelines: State-of-the-Art Review". *Journal of Construction Engineering and Management*, *146*(6), 03120001. doi.org/10.1061/(asce)co.1943-7862.0001819

Najafi, M. (2005). *Trenchless Technology: Pipeline and Utility Design, Construction, and Renewal (Design considerations for trenchless renewal methods)* (1st ed.). New York: McGraw-Hill Education. Retrieved from https://www.accessengineeringlibrary.com/content/book/9780071422666

O'Rourke, T.D., Netravali, A.N.A.N., Pendharkar, S.M., Tonkinson, A., Chaudhuri, D., & Toprak, S. (1996). *Evaluating Service Life of Anaerobic Joint Sealing Products and Techniques*. Cornell University, Ithaca, NY, USA.

O'Rourke, T.D., Strait, J.E., Mottl, N., Berger, B.A., Wham, B.P., Stewart, H.E., & Price, D. (2021). *Performance Evaluation of Aqua-Pipe under Earthquake-Induced Ground Deformation* (Report). Cornell University, Ithaca, NY. Retrieved from https://cpb-us-w2.wpmucdn.com/sites.coecis.cornell.edu/dist/a/38/files/2020/10/26Sept20InterimSanexenReport.pdf

Roboski, J., & Finno, R.J. (2006). "Distributions of ground movements parallel to deep excavations in clay". *Canadian Geotechnical Journal*, *43*(1), 43–58. doi.org/10.1139/t05-091

Stewart, H.E., O'Rourke, T.D., Wham, B.P., Netravali, A.N., Argyrou, C., Zeng, X., & Bond, T.K. (2015). "Performance Testing of Field-Aged Cured-in-Place Liners (CIPL) for Cast Iron Piping". Cornell University, Ithaca, NY. Retrieved from https://lifelines.cee.cornell.edu/projects/

Vladeanu, G., & Matthews, J.C. (2018). "Analysis of risk management methods used in trenchless renewal decision making". *Tunnelling and Underground Space Technology*, *72*(November 2017), 272–280. doi.org/10.1016/j.tust.2017.11.025

Zhao, J.Q., & Rajani, B.B. (2002). "Construction and Rehabilitation Costs for Buried Pipe with a Focus on Trenchless Technologies". Ottawa: Institute for Research in Construction National Research Council Canada.